Zirconium-Based Metal-Organic Frameworks for Artificial Electrochemical Photosynthesis

Benjamin David Thomas

Dissertation submitted to the faculty of the Virginia Polytechnic Institute and State University in partial fulfillment of the requirements for the degree of

Doctor of Philosophy
In
Chemistry

Amanda J. Morris (Chair)
Paul A. Deck
Feng Lin
Joseph S. Merola

12/17/24
Blacksburg, VA

Keywords: metal-organic frameworks, artificial photosynthesis, electrochromic, CO_2 reduction, water oxidation

Zirconium-Based Metal-Organic Frameworks for Artificial Electrochemical Photosynthesis

Benjamin Thomas

ABSTRACT

The utilization of porous materials for electrocatalytic applications has been of high interest due to their high surface area and increase in electrode-electrolyte interface. Metal-organic frameworks (MOFs) are an emerging class of 3-D porous materials consisting of inorganic nodes bound by multidentate organic linkers. MOFs have permanently large surface area, high stability, and the tunability of the structure. The metal source or the organic linker can be swapped to create a material with desirable features. MOFs have been explored for applications in electrocatalysis, conductivity and energy storage. The fundamental charge transfer methods of MOF thin films is discussed and the utilization of these conductive materials for the key reactions in artificial photosynthesis is explored to highlight methods to improve the efficiency of these materials for electrocatalysis.

The Morris group has previously shown that charge transfer in MOFs can occur through a redox hopping mechanism in which the charge hops from redox center to redox center through space followed by the movement of a charge balancing ions. In Chapter 2, the charge transfer mechanism within the MOF is further investigated by utilization of spectroelectrochemistry. The incorporation of a redox center, $Ru(bpy)_2(dcbpy)$, "RuBPY" where bpy = 2,2′-bipyridine; bpy-$(COOH)_2$ = 5,5′-dicarboxylic acid-2,2′-bipyridine into the UiO-67 framework creates a conductive MOF that is also electrochromic. RuBPY is a deep orange color in the standard Ru^{II} state and upon oxidation to Ru^{III} it is pale green. The change in absorption profile of the redox center allows for the rate of oxidation to be determined through absorbance measurements. The material showed minimal change in absorbance upon applying an oxidative potential. The incorporation of a

sulfonate group into the backbone of the RuBPY-UiO-67-SO_3H MOF allowed for a much higher change in absorbance, converting the entire MOF into the oxidized state. The change in level of absorbance indicates that the sulfonate groups improve the conductivity within the pores of the MOF, allowing for oxidation of previously electrochemically inaccessible redox centers. The sulfonate groups are thought to break ion pairs of the electrolyte and increase effective electrolyte concentration within the pores. The sulfonate groups' ability to improve the conductivity within the MOF can be further investigated to improve charge transfer through porous materials.

The sulfonate groups were again incorporated into the UiO-67 MOF framework for use in electrocatalytic applications by also incorporating the known water oxidation catalyst, RuTPY, Ru(tpy)(dcbpy)H_2O. A RuTPY-UiO-67 film had previously shown reactivity as a water oxidation catalyst with improved activity over a monolayer of RuTPY on fluorine-doped tin oxide, FTO. The sulfonate groups were added to create a proton transfer chain that shuttled the generated protons away from the catalytic site to improve reactivity. The incorporation of sulfonate groups again showed improved charge transfer from the MOF materials with the RuTPY-UiO-67-SO_3H being 100% electrochemically accessible. The water oxidation capabilities improved giving the material increased oxygen generation upon oxidation of water. The improvement of catalytic activity of RuTPY-UiO-67-SO_3H was beyond the increased electrochemical accessibility means the proximal sulfonate groups were aiding in catalysis in some manor. This work highlights the use of multivariate approaches to MOFs to improved efficiency in various applications.

The fourth chapter discusses the other half of artificial photosynthesis, CO_2 reduction. The known CO_2 reduction catalyst, Ni(cyclam), is incorporated into a zirconium-based MOF, VPI-100. The VPI-100 powder was electrochemically deposited onto a glassy carbon electrode and the film was used for electrochemical CO_2 reduction into carbon dioxide. The film successfully generated

CO as a major product with a faradaic efficiency of 56%. The film was stable under electroreduction conditions and was able to be recycled for continuous production of CO.

The final chapter is a review that discusses the utilization of MOFs as photocatalysts for CO_2 conversion using only abundant earth metals. While most CO_2 catalysts are expensive noble metals, the development of cheap abundant catalytic materials is extremely relevant to a clean energy future.

Zirconium-Based Metal-Organic Frameworks for Artificial Electrochemical Photosynthesis

Benjamin Thomas

GENERAL AUDIENCE ABSTRACT

The climate crisis has led to a need to develop more efficient renewable energy sources and novel energy storage devices. Electrochemical systems have shown great promise in providing a clean energy future with developments in lithium-ion batteries, fuel cell technologies, and artificial photosynthesis to produce value added chemicals. The basis of all these electrochemical processes is efficient charge transfer to the necessary components. Metal-organic Frameworks (MOFs) which are crystalline, porous materials made up of inorganic metal nodes connected in a discrete pattern by organic linkers. The three-dimensional nature of the MOFs consisting of connected pore networks has shown great promise to be improved conductive materials and electrocatalysts compared to existing materials. Herein, we exploit the modular nature of the MOFs to incorporate functional groups that improve ion transport and allow catalytic activity for artificial photosynthesis. The work here shows that MOF structures can be further modified to provide even more efficient electrocatalytic behavior to aid in a clean energy future.

Acknowledgments

First, I would like to thank my advisor, Dr. Amanda Morris. Her unwavering support of me, even when I didn't believe in myself, was crucial to my graduate school career. I am inspired by your commitment to doing the hard science the correct way, your passion for education, and your commitment to making academia a better place. Your influence in the lab and out has changed me for the better, and I will be forever grateful for that.

I want to thank the other faculty and staff members of the department, specifically my committee members, Dr. Paul Deck, Dr. Feng Lin, and Dr. Joseph S. Merola, for their support and insight. All the professors I had for my classes gave me a fantastic foundation of chemistry knowledge for my research studies. This department truly feels like a family and I am honored that I was able to work with many of you in various capacities to make it a better place.

I want to thank my group members of past and present. Being in the trenches with you all "baking" MOFs and troubleshooting broken instruments has made these five years infinitely more enjoyable. I want to specifically shout out Dr. Brad Gibbons for his mentorship and support in my research. I appreciate your advice and your friendship. I also want to thank my undergraduate students, Julia LaFortune, Dequinte Robinson, Quinn Smith, and Cleo Orlando. You were all fantastic researchers to mentor and I am proud to see you all continuing your scientific careers. I wish all the success in the world for all of you.

I want to thank all the people outside the department I have met in Blacksburg. This town is truly a special place with special people. I specifically want to acknowledge my

ultimate frisbee group, Blue Ridge Ultimate. The countless games of pickup and tournaments I attended gave me a great escape from the lab to get fresh air and throw a plastic disc. I will miss our trips to Sub Station II, movie nights, and Hokie sports events. The friendships I have made with you all have truly made southwest Virginia feel like home.

I want to thank my family for supporting me in this endeavor. Your presence through stressful times has been incredible, and I will forever appreciate your encouragement to do anything I want in life. I have been a lifelong Hokie because of you all and now I have a paper that proves it.

Table of Contents

Chapter 1

Background of Charge Transfer and Electrocatalysis in Metal-Organic Frameworks (MOFs)

1.1 Research Motivation

As global energy demands increase, research has focused on finding energy sources other than fossil fuels for decades.[1] Solar and wind are two inexhaustible alternatives that have shown promise in mitigating CO_2 emissions for a sustainable future.[2] The use of these energy sources is limited by their immediate nature and lack of availability 24/7.[3] The creation of efficient energy storage is crucial to implementing these energy forms into the commercial grid. One solution is using electrocatalysts to regenerate conventional fuels such as H_2 and CH_4. The production of energy sources from CO_2 and H_2O from solar and wind power is known as artificial photosynthesis.[4] Figure 1 shows a typical electrochemical cell for artificial photosynthesis. For a clean energy future, the development of catalysts that can generate these products efficiently is of high interest.[5]

Electrochemistry is the application of a potential bias to induce a chemical change at a polarized surface. The redox potentials of different species can be exploited to create spontaneous reactions that produce an electrical current, such as in a Li^+ ion battery.[6-8] When external energy is applied, a nonspontaneous reaction can occur, and materials can reach oxidation states that have chemical relevance in catalysis, chemiluminescence, energy storage, and other applications.[9-14] The electron transfer needed for this reaction occurs at the electrode surface, meaning the development of highly active and efficient electrodes is key to the success of any electrochemical reaction.

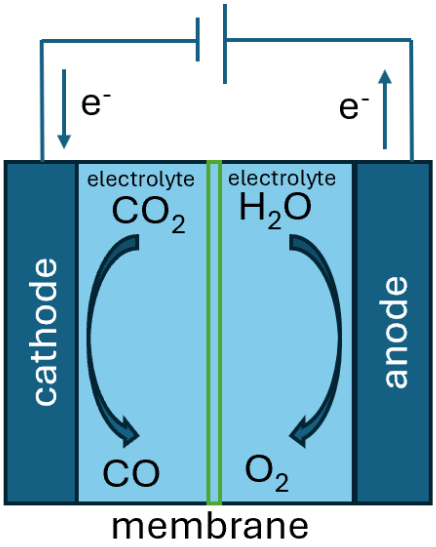

Figure 1: Example electrode for artificial photosynthesis converting CO_2 to CO and oxidizing water to O_2

Porous three-dimensional electrodes have an advantage over 1D and 2D electrodes because of their high surface area and the ability for the electrolyte to diffuse freely throughout the connected nanopores, limiting the formation of aggregates.[15] The mechanism of charge transfer at the solid-liquid interface of the porous electrodes has been studied intently, but the charge transfer mechanisms away from the electrode surface throughout the materials are underexplored.[16, 17] Understanding the mechanism for the diffusion of charge in 3D electrodes and increasing rate of electron transfer is vital for the efficient use of these materials in energy storage and electrocatalysis.

1.2 Metal-Organic Frameworks

Metal-organic frameworks (MOFs) are a class of 3-D frameworks that are characterized by their tunability, stability, and porosity.[18] MOFs are a form of coordination polymer built from metal ions or clusters and polydentate organic linkers bound by bridging groups such as carboxylates. The ability to switch the inorganic node's composition or the identity of the organic linker has led to thousands of different MOFs being synthesized and reported in the past 25 years

for a wide array of applications. MOFs are well known for their extremely high surface area and ability to contain large amounts of gas The high surface area and porosity of these materials has been exploited for gas storage and separation[19], drug delivery[20], electrochemical materials[21-26], and catalysis.[27]

MOF films have been grown on conductive electrode surfaces for use as conductive materials and in electrocatalysis. Research into the mechanisms of charge transfer and electrocatalysis within these MOF films is crucial to their use in artificial photosynthesis

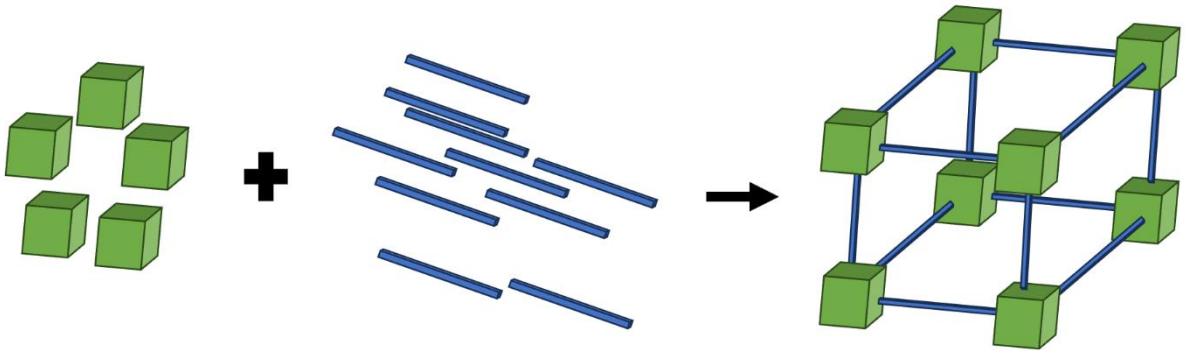

Figure 2: Scheme of MOF synthesis

Several research groups are interested in using MOF films for conductive applications such as electrocatalysts, batteries, and other energy storage materials. Many MOFs with nodes consisting of redox active first row transition metals can be used in electrocatalytic applications. Unfortunately the oxidation or reduction of these metal nodes tends to lead to the MOF falling apart forming a metal oxide that becomes the true active catalyst.[28-31] Zirconium based MOFs tend to be more stable in a wide range of conditions.[32] The inherent insulating nature of zirconium carboxylate based MOFs has led to the desire to modify these frameworks to improve conductivity.[33] Charge transfer through MOFs can occur via several different mechanisms: through bond, through plane, through space, redox hopping, and guest promotion. The Morris group was the first to propose a redox hopping mechanism in which the charge “hops” among

redox centers throughout the MOF, followed by the subsequent diffusion of the counter ion shown in Figure 3.[26] The speed of this charge transfer is affected by two different but correlated diffusional processes. The first is the diffusion rate of the electron, D_e, which is the actual exchange of charge between the redox centers dictated by the self-exchange rate of the charge carrier.[34] The second is the diffusion rate of the charge balancing counterion, D_i, which has several factors, including ion identity, MOF pore size, ion pairing, and concentration of the counter ions.[35] The counter ion movement is generally the bottleneck for most charge transfer reactions because the mass transport of the ion is much slower than that of an electron.[36] Most electrochemical techniques combine these diffusion coefficients into a single D_{app} term. Investigating parameters relevant to improving the diffusion coefficient can help the efficiency of charge transfer within MOF films at an electrode surface.

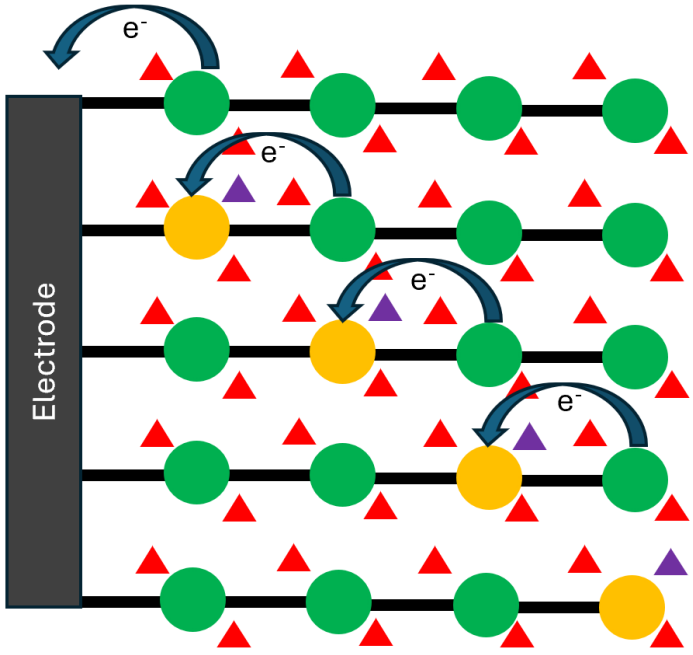

Figure 3: Mechanism of redox hopping upon oxidation. Green circle (redox species), Orange circle (oxidized redox species), Red triangle (counterion), Purple triangle (moving counterion)

1.3 Charge Transfer Investigations

There are several methods for investigating the charge transfer parameters for electrochemically active materials.[37] Chronoamperometry is the application of a potential to an electrode and the monitoring of the resulting current over time. The current response of the complete oxidation or reduction of a species on the surface of an electrode can be modeled using the Cottrell equation to calculate a diffusion coefficient, D_{app} shown in eq 1.[38]

$$i = \frac{nFAC\sqrt{D_{app}}}{\sqrt{\pi t}} \quad (1)$$

In eq. 1, i is current (A), n is moles of electrons transferred, F is Faraday's constant, A is the area of the electrode, *C* is the concentration of electroactive species, and *t* is time. The plot of current versus the inverse of $t^{1/2}$ can be used to determine the apparent diffusion coefficient of the electrolysis by extracting the slope of the linear region. The Cottrell equation can be integrated into the Anson equation to correlate the total charge transferred to time. The Anson equation lowers the impact of non-faradaic current in its measurement, so the derivation of D_{app} tends to be more accurate.[37] The plot of charge vs $t^{1/2}$ can give D_{app} from the slope.

$$Q = \frac{2nFAC\sqrt{D_{app}t}}{\sqrt{\pi}} \quad (2)$$

The Morris group has used chronoamperometry to independently determine the diffusion of both electrons and ions within MOF films. The Scholz model uses chronoamperometry data when applied to a microcrystal on an electrode surface to describe the nature of charge transfer throughout the material.[39] Briefly, upon application of a potential jump, the charge transfer of the crystallite starts at the three-phase boundary. The three-phase boundary is the crystal's edge on the outside, touching the electrode surface. The edge is where the crystal, the electrode, and the counter

ions are all interacting shown in Figure 4D. This edge undergoes charge transfer rapidly due to the bath of ions sitting outside the crystallite. As charging continues, the oxidation occurs rapidly at the electrode surface and moves upward. The electron movement is perpendicular to the electrode surface while the ion movement is parallel to the electrode surface into the crystallite to balance charge.

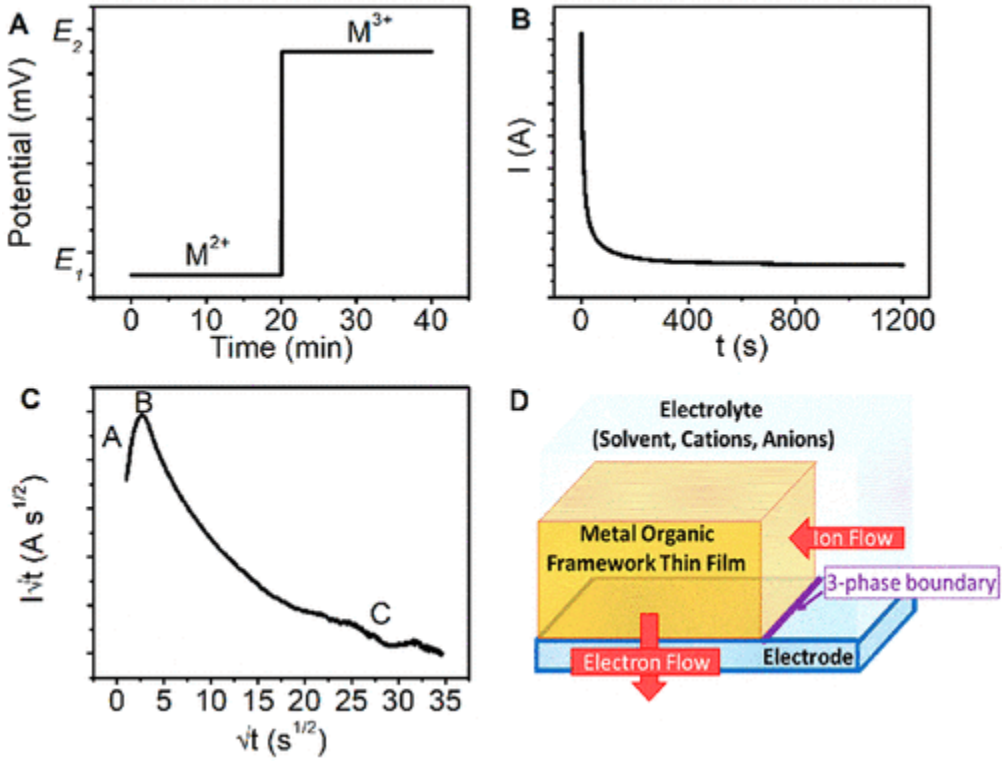

Figure 4: Application of the Scholz Model to chronoamperometry data. A) Waveform for potential step experiment B) Current response for potential step experiment C) plot of $i*t^{1/2}$ vs $t^{1/2}$ of current response D) Model of microcrystal on electrode surface showing the direction of ions and e^-. Reprinted with permission from *J. Am. Chem. Soc.* 2019, 141, 30, 11947–11953[40] Copyright © 2019 American Chemical Society

The Scholz model can be applied to MOFs such as an M-NU-1000 MOF doped with three different metallocenes, (M=Fe,Ru,Os), grown on FTO slides. The results showed the D_e followed self-exchange rates, with Os-Nu-1000 showing the fastest electron transport. The D_i correlated with the association constant of the ion with the metallocene as tetrakis(pentafluorophenyl)borate, $TFAB^-$ has a weaker pairing constant with the redox center than PF_6^- and $TFAB^-$ showed a higher

D_i. MOF films with different pore sizes can be used to test the impact of both space and hopping distance on D_{app}

Cyclic voltammetry can be used to determine more information about the electrochemical processes occurring on an electrode. Cyclic voltammetry is a potential sweep in both oxidative and reductive directions. The rate at which the potential is cycled can give a multitude of information on the electrochemical processes in the system.[41] Nicholson and Shain describe eight different electrochemical reactions that can occur at an electrode surface. The correlation between scan rate and current response, the ratio of peak heights, and peak separation can determine which case is happening for a specific redox event seen in a voltammogram.

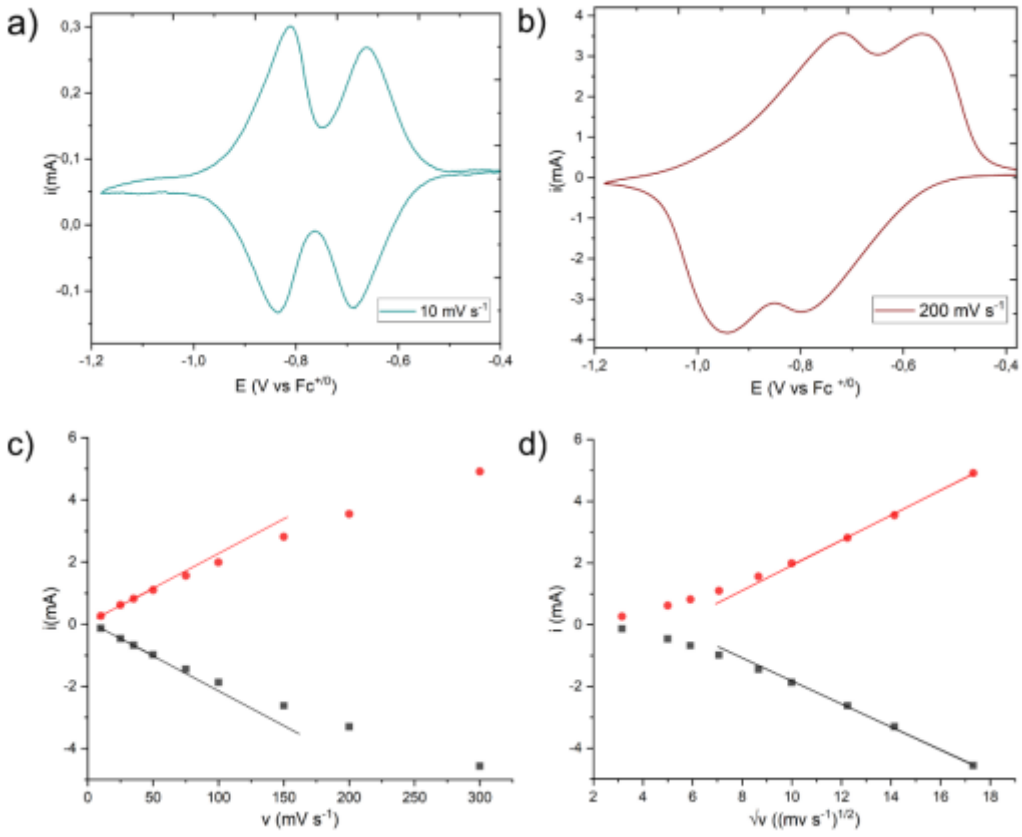

Figure 5: Cyclic Voltammograms of Zn-PDI@FTO in Ar-saturated 0.5 KPF_6 DMF at a scan rate of a) 10 mv/s and b) 200 mv/s. The relation of anodic peak currents to c) *v* and d) $v^{1/2}$ Reprinted with permission from ACS Nano 2023, 17, 21595-21603[42]

Scan rate cyclic voltammetry dependence studies for thin film electrodes can give us information on the film's method of charge transfer and the D_{app} in the cell. A surface-based electron transport reaction would follow Equation 3 where Γ is the total active species on the electrode surface. The peak current has a linear relationship with the scan rate, *v*. Diffusion based electrolysis follows the Randles-Selvik Equation, equation 4

$$i = \frac{n^2 F^2 v A \Gamma}{4RT} \tag{3}$$

$$i = 0.4463 nFAC \sqrt{\frac{nFvD}{RT}} \tag{4}$$

When diffusional transport is the mechanism of charge transfer, the peak current vs $v^{1/2}$ plot would have a linear relationship. MOF films provide an interesting combination of both surface and diffusional charge transfer. At slow scan rates, the rate of charge transfer throughout the MOF film outpaces the rate of potential sweep, meaning the current response would show a surface-bound redox material. An example of the surface-bound charge transfer is shown in Figure 5a; a Zn-NDI MOF film grown on an FTO electrode undergoes cyclic voltammetry at 10 mV/s showing a typical surface-based cyclic voltammogram with the oxidative and reductive peaks on top of each other with minimal peak splitting. On the other hand, at faster scan rates, the diffusion of charge cannot keep up with the rate of potential sweep, so the current response shows a diffusional mechanism of charge transfer throughout the MOF film. The diffusional transport is shown in Figure 4b, where the Zn-NDI (NDI=nap MOF is subjected to cyclic voltammetry at 200 mV/s. The redox waves show classic diffusional behavior with duck wave shapes and peak separation relative to the rate of charge transfer. The transition from surface wave-like behavior to diffusional wave-like behavior can be used to determine the D_{app} of the MOF film. A dimensionless

parameter, λ_e, can be used to determine the switching condition that correlates the film's thickness to its charge transfer behavior, Equation 6.

$$\lambda_e = d\sqrt{\frac{Fv}{D_{app}RT}} \quad (5)$$

The crossover point from the surface behavior to diffusional behavior occurs when $\lambda_e \approx 1$. The crossover point can be determined by plotting the peak currents against *v* and the peak currents against $v^{1/2}$. The point at which the linear dependence on *v* shifts to a linear dependence on $v^{1/2}$ is the crossover point. These plots for the Zn-NDI MOF film, shown in Figures 4c and 4d, show the crossover point to be around 50 mV/s. Using eq. 5, the diffusion coefficient for the Zn-NDI MOFs is about 2 x 10^{-10} cm^2/s. This calculation was within error of other methods of determining D_{app} in these redox active Zn-NDI MOF films. However, resistive current can impact the peak height calculations, which can be difficult to reconcile, and the transition scan rate can be difficult to determine with precision.[37]

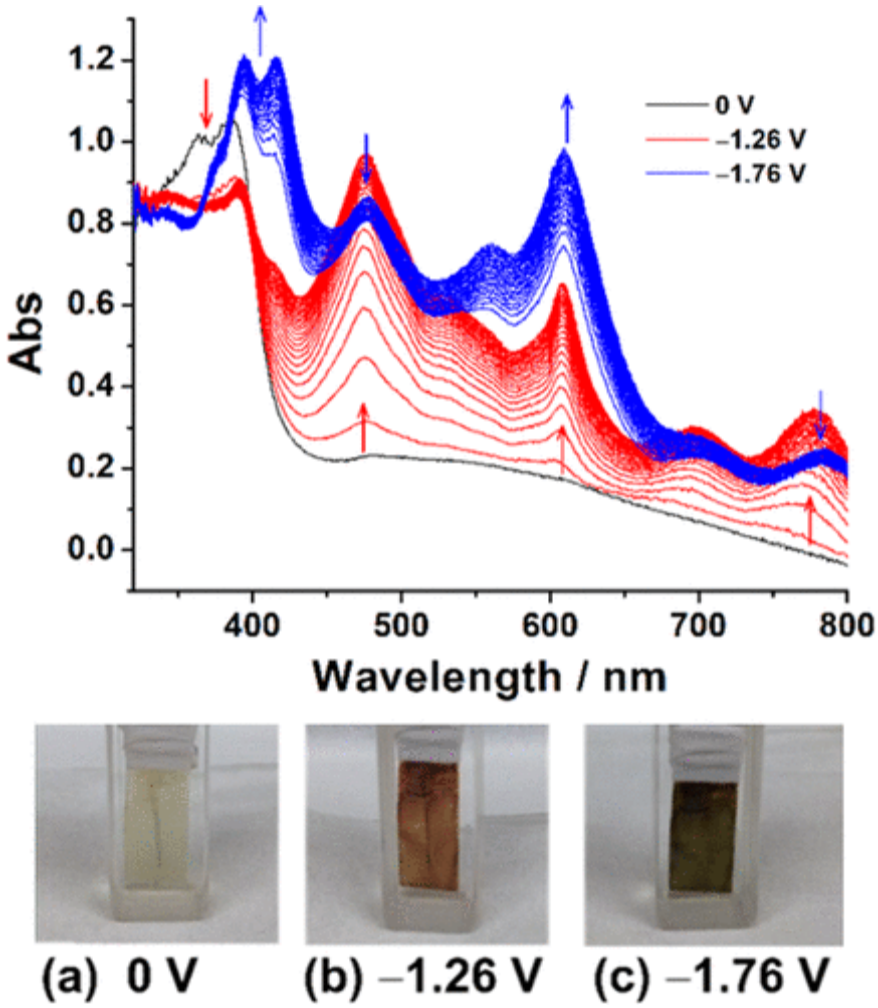

Figure 6: Absorption spectra of Zr-(dcphOH-NDI)@ FTO Film upon application of reduction potential and pictures of color changes upon reduction in 0.8 M KPF_6 in DMF at a) 0 V, b) -1.26 V and c) -1.76 V. Reprinted with permission from *J. Am. Chem. Soc.* 2018, 140, 8, 2985–2994 Copyright © 2018 American Chemical Society[23]

For electrochemical methods, removing background currents resulting from double-layer charging and side reactions can be an impossible challenge. Spectro-electrochemistry can mitigate the impact of background current issues on the diffusion coefficient calculations.[42] Using the ultraviolet-visible absorption spectra of an electrochromic complex, a single wavelength can be monitored as potential is applied to determine D_{app}. The rate at which the absorption changes from the reduced form to the oxidized form is correlated with the rate of electron transport throughout the material. A modified Anson equation for chronoabsorpometry is shown in eq 6. Where A is

the absorbance, and A_{max} is the maximum absorbance of the electrochromic material, in this case, the MOF film. Figure 6 shows the absorption spectra as well as the film color change of a Zr-(dcphOH-NDI) MOF film on FTO (dcphOH-NDI=3-hydroxy-2-[7-(4-carboxy-2-hydroxyphenyl)-1,3,6,8-tetraoxo-3,6,7,8-tetrahydro-1*H*-benzo[*lmn*][3,8]phenanthrolin-2-yl]benzoic acid). The (dcphOH-NDI linker is electrochromic and has two transition potentials. At -0.96 is the dcphOH-NDI/ dcphOH-NDI$^-$ couple and at -1.36 is the dcphOH-NDI$^-$/dcphOH-NDI^{2-}. Upon reduction at -1.26 V vs $Fc^{+/0}$, absorption peaks appear around 475, 608, and 780 nm.

$$\Delta A = \frac{2A_{max}\sqrt{D_{app}t}}{d\sqrt{\pi}} \quad (6)$$

Using the absorption change at 475 nm, a chronoabsorpometic analysis was done to calculate the $D_{app,}$ which was 2.1 x 10^{-10} cm^2/s. This value was an order of magnitude higher than the D_{app} calculated through cyclic voltammetry, presumably due to the removal of background current and resistive current from calculations.

1.4 Water Oxidation

Electrocatalysis is the application of an electrochemical potential to a certain substrate to produce a desired product. The oxidation or reduction of a substrate to perform a desired product has been used to generate more efficient pathways for complex materials for complex organic synthesis that avoid toxic redox agents.[43, 44] There is a desire to use electrocatalysis to generate a clean energy future by generating energy from naturally occurring materials such as H_2O, H^+, and CO_2. By generating electrons and protons from water that can be used in the reduction of CO_2 and H^+ to combustible materials, a carbon neutral energy source can be created.[45] The oxidation of water converts water into oxygen, protons and electrons, Eq. 4.

$$2H_2O \rightarrow O_2 + 4H^+ + 4e^- \quad E° = 1.23 \text{ V vs. NHE} \quad \text{Eq. 4}$$

The catalysis comes with the challenge of having high activation energy because of the intermediates generated requiring potentials well past 1.23 V vs. NHE to occur.[46] To overcome the activation energy, catalysts can be used to stabilize the intermediates and lower the overpotential needed to produce oxygen creating a more efficient process.

Water oxidation is a fundamental part of the photosynthesis process that nature uses to convert solar energy into chemical energy. Photosystem II, a protein found in plant cells, is known to be responsible for the conversion of water molecules into oxygen and protons. The active site for water oxidation is a Mn_4CaO_5 cluster within the protein.[47] Absorption of light is done by a nearby a nearby chlorophyll, The generated electron hole is inevitably filled by the Mn_4CaO_5 cluster, oxidizing the active site. The photooxidation process repeats itself 3 times for a total of four electron transfers. The fully oxidized cluster then proceeds to split two water molecules into two oxygen molecules and four protons.

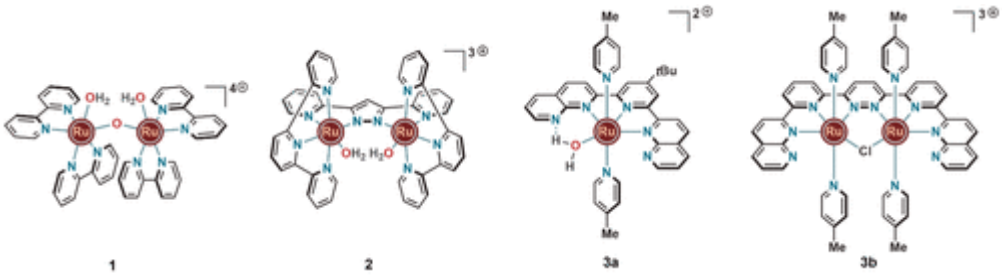

Figure 7: The original Ru complexes active for water oxidation. Reprinted with permission from Acc. Chem. Res. 2021, 54, 3326−3337[48]

Attempts to artificially match the catalytic activity of the Mn_4CaO_5 cluster have led to various water oxidation catalyst designs. Early attempts to mimic PSII led to synthetic manganese-oxo clusters.[49] These complexes show great promise with proximal Mn atoms reaching a Mn^V=O being a key step in oxygen evolution. Other atoms such as ruthenium and iridium that have higher stability at the higher oxidation states needed for the four electron transfer required in water

oxidation.[50] The blue dimer, $[(bpy)_2(H_2O)Ru^{III}(\mu\text{-}O)Ru^{III}(H_2O)(bpy)_2]^{4+}$, shown in Figure 7 (compound 1), is one of the most well studied water oxidation catalysts ever synthesized.[51] However, low turnover frequencies, $4.2x10^{-3}$ s^{-1} and quick degradation led to interest in developing alternative polypyridyl ruthenium complexes for water oxidation.[46] After other investigations into Ru dimer complexes the first mononuclear Ru water oxidation catalyst was synthesized, Figure 7 (compound 3a). The mononuclear complex however, suffered from low turnover (580) compared to its dinuclear counterpart, Figure 7 (compound 3b), (3200). Even with lower rates of catalysis, he investigations into mononuclear complexes remains of interest due to the ease of tunability as well as the ability to fully understand the mechanisms that drive oxygen evolution.[52] Ruthenium complexes bound by tpy linkers, (tpy)= 2,2′;6′,2″-terpyridine) have shown great interest in mechanistic studies due to the complete understanding of the pathway to oxygen production including understanding behind the terminal O-O bond formation step.[53]

The Ru (tpy) (L) series has been explored for water oxidation capabilities. Some of the synthesized homogenous catalysts have shown to have a higher rate of oxygen production than the Mn_4Ca cluster. The issue with these catalysts is their quick deactivation as they dimerize in solution. A solution to this has been the incorporation of these catalysts into MOF frameworks to isolate the active sites and give higher stability. The Morris group has incorporated Ru (tpy) (dcbpy) (dcbpy= 2,2′-bipyridine-5,5′-dicarboxylic acid) into a UiO-67 framework for electrocatalytic water oxidation.[24] Some of the biphenyl dicarboxylic acids were replaced with an active ruthenium water oxidation catalyst that contained a bipyridine dicarboxylic acid so the catalyst could be easily introduced into the MOF structure, Figure 8. The ruthenium loaded MOF thin film on FTO showed 5 times higher water oxidation rates, turnover frequency of 0.2 s^{-1}, than that of undoped UiO-67 thin film on FTO.

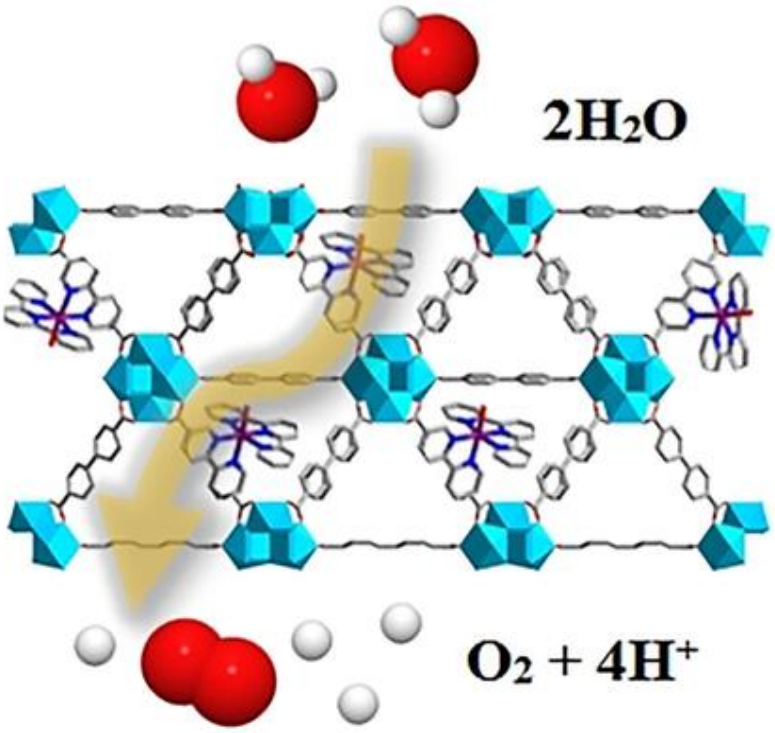

Figure 8: Schematic representation of water oxidation by a catalyst-loaded metal-organic framework. Reprinted with permission from ChemSusChem 2018, 11, 464 – 471[54]

Further efforts to increase the efficiency of these MOFs have included combination with light. The end goal of an artificial photosynthetic system has been to create an array for energy production from fully renewable energy sources. The growth of a UiO-67 thin film containing the known ruthenium polypyridyl catalyst, Ru(tpy)(dcbpy) was grown a film of WO_3, a semiconductor able to absorb light with a band gap suitable for water oxidation reactions.[21] The result was a photoelectrochemical catalyst that showed oxygen production under water oxidation conditions at a thermodynamic underpotential of 600 mV vs NHE when exposed to light, which is over 1 V lower than the native ruthenium-loaded UiO-67 with no semiconductor. The MOF-semiconductor combination showed hole transfer properties, indicating the charge transfer from the Ru catalyst to the WO_3 was part of the mechanism of oxygen production.

To further increase efficiency in artificial photosynthesis materials we look to nature and the thermodynamics of the reaction itself. The water oxidation reaction is pH dependent. At neutral

pH, water molecules are oxidized according to Eq. 4 with a standard reduction potential of 1.23 V vs natural hydrogen electrode (NHE). At higher pHs, hydroxyl ions are favored to undergo oxidation according to Eq. 5 with a standard reduction potential of 0.40 V vs NHE, which is much lower than the standard potential. Hydroxyl ions have a much lower oxidation potential, making this process favored; however, the subsequently lower pH increases the potential required for proton reduction at the anode, meaning a decrease in catalytic current at high pH is generally not seen to this degree.

$$2H_2O \rightarrow O_2 + 4H^+ + 4e^- \quad E° = 1.23 \text{ V vs. NHE} \qquad \text{Eq. 4}$$

$$4OH^- \rightarrow 2H_2O + O_2 + 4H^+ + 4e^- \quad E° = 0.40 \text{ V vs. NHE} \qquad \text{Eq. 5}$$

In nature, photosystem II has a built-in mechanic to remove protons from the active site which serves two purposes. The first is the protons are needed in the photophosphorylation process at the thylakoid lumen to generate ATP. The second is to reduce charge buildup at the active Mn_4CaO_5 center. A buildup of charge by produced protons creates an increased thermodynamic barrier for the water oxidation reaction.[55] Proximal amino acids capable of creating a hydrogen bond network, including aspartate, glutamate, and histidine, create a channel with a tunnel of water molecules to act as a proton transport chain.[56] The high rate at which these protons move long distances indicates a Grotthus mechanism in which the proton is quickly transferred through a network of hydrogen bonds.[55]

Research groups have tried to exploit this phenomenon by incorporating proximal proton transfer groups on molecular catalysts.[57, 58] The incorporation of a proton acceptor onto a family of ruthenium polypyridal complexes, $[Ru(tda)(py)_2]$ tda= ([2,2′:6′,2″-terpyridine]-6,6″-dicarboxylate) (py=pyridine), showed improved water oxidation reactivity at neutral pH. The DFT

calculations showed the proton transfer to the dangling carboxylate group was vital to the mechanism kinetics increasing rate more than 3-fold compared to the non-carboxylated catalysts. The implementation of intramolecular proton transfer shows increases in the overall rate. However, the proton still needs to be removed and shuttled away from the active site which cannot be done intramolecularly. A MOF backbone can give us a protein-like structure to work around that creates a wide new array of manipulations that can be made to adjust the proximal structure surrounding the active site, including the addition of proximal groups to aid in proton transport.

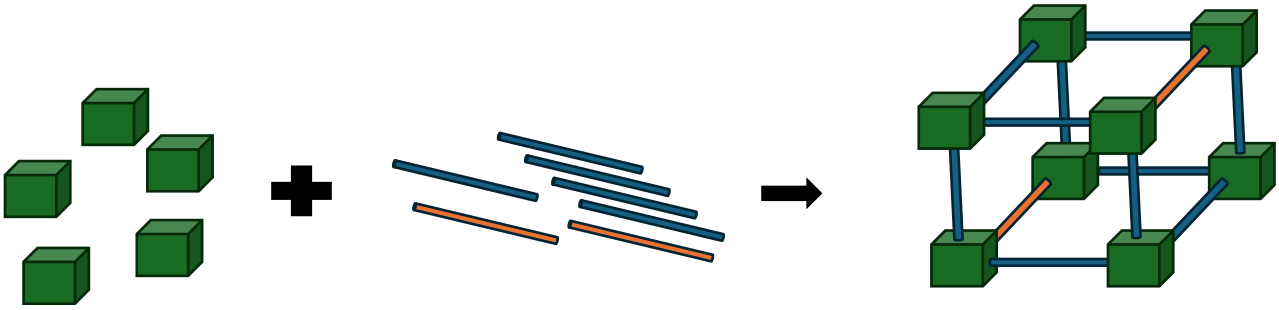

Figure 9: Synthesis scheme of multivariate MOF with various linkers

A multivariate MOF incorporates more than one linker or metal ion that can work synergistically to improve application performance. The idea of multivariate MOFs has been explored for several applications, including gas absorption and separation.[59] The combination of various functional groups within a MOF-5 style increased absorption. Incorporating various metal ions into MOFs has been used to create cooperative catalysts for several different reactions, including epoxide opening catalyzed by Cr, Mn, Cu, and Co combinations.[60] The incorporation of functional groups for cooperative catalysis with a singular active site has never been shown in a MOF, and the features of this approach are shown in future chapters of this dissertation.

1.5 CO_2 Reduction

On the other side of the electrochemical cell in artificial photosynthesis is the cathode where CO_2 reduction occurs. CO_2 reduction has been of high research interest for a long time now. The increase in CO_2 emissions since the Industrial Revolution has led to a large quantity of gas in the atmosphere from anthropogenic sources.[61] Current practices involve the capture and sequestration of CO_2 to hinder the ecological impact of the greenhouse gas.[62-64] Carbon dioxide reduction produces value-added chemicals that can be used in synthetic processes as well as a fuel source in combustion engines.[65] For electrochemical reduction, the half potentials for most products are very similar, making a selective catalyst for a product extremely difficult.[66] Copper metal is extremely efficient in the reduction of CO_2 yet produces dozens of products making separation and usage much more difficult.[67] Figure 10 shows the various products that can be generated from electrochemical reduction of CO_2

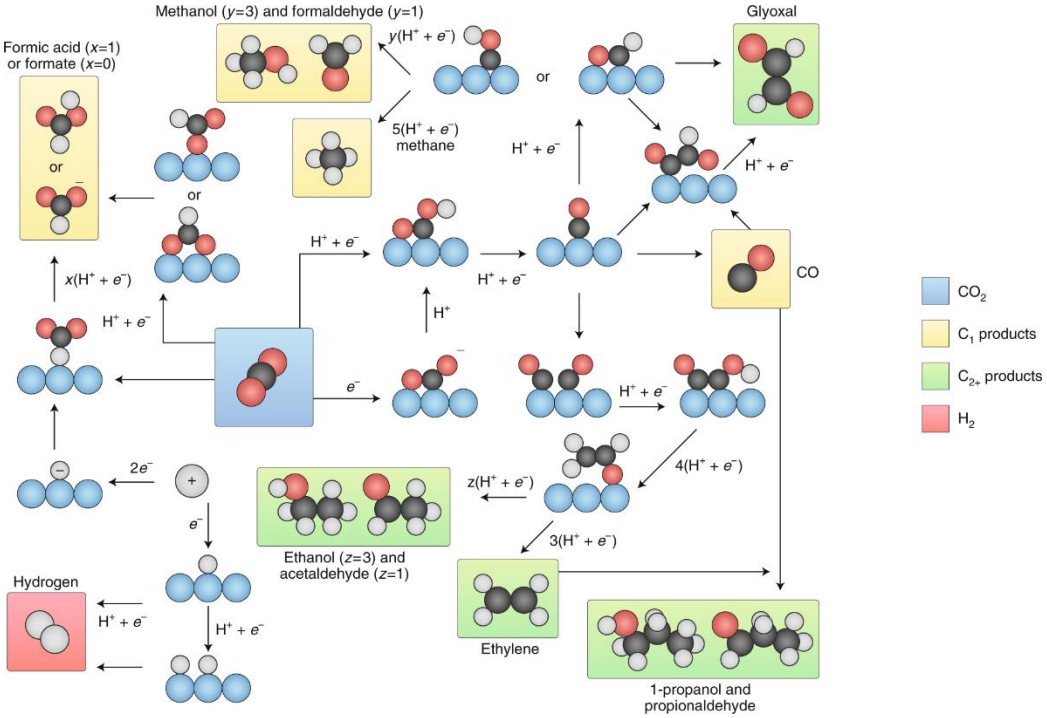

Figure 10: Pathways for CO_2 reduction; C-Black, O-Red, H-White, Catalyst-Blue Reproduced with permission from Nature Energy VOL 732 4, SEPTEMBER 2019 732–745[68]

The reduction of CO_2 can occur through a $2e^-$, $4e^-$, $6e^-$, or $8e^-$ process. The simplest of these products are C_1; carbon monoxide (CO), formic acid (HCOOH), methanol (CH_3OH), and methane (CH_4) are the four main targets for CO_2 usage. Product selection can be determined by various factors, including catalyst selection, surface morphology, electrolyte/solvent system, local pH,[69] and the conditions of mass transport.[70]

Traditional electrocatalysts include bulk metal sheets. These materials were easy to prepare and gave insight to reaction conditions that give various products.[71] Current heterogenous catalyst research looks into nano structuring these metals.[72, 73] The use of Ag or Au nanoparticles has shown highly efficient CO_2 conversion to CO. A large dependence on particle size in the efficiency of reactivity has been observed due to surface area and binding strengths of various intermediates. These metals are recyclable and easily be separated from the electrochemical cell to be used again.[74] The understanding of the mechanism at the solid interface can be hard to unravel with the surface/substrate interaction not being fully characterized.[75]

Homogeneous electrocatalysts for CO_2 reduction have been well studied for their ease in mechanistic understanding and their ability to be tuned. By having isolated active sites, the interactions between the CO_2 substrate and the transition metal atom can be investigated and tuned to get high selectivity to a single product.[76] Most of these catalysts tend to be noble metal polypyridyl complexes of noble metals such as Ru or Ir.[77, 78] These catalysts can show high reactivity at low overpotentials however their stability has shown to be low as they can deactivate through dimerization or other degradation pathways.[79]

Combining both the benefits of the solid metal catalysts and the tunability of the homogenous catalysts, the use of MOFs for CO_2 conversion is a growing field. Most of these MOFs have active sites at the metal nodes with Cu or Ru atoms being highly active for the

production of CO.[80] However, a lot of these MOFs lack stability under reduction conditions.[81] Most of the Cu or Ru based nodes degrade upon prolonged electrolysis leaving a metal oxide on the electrode surface.[82] While these catalyst show high reactivity, the exploitation of the porous nature of MOF frameworks themselves has been underexplored for the electrocatalysis. The need to find stable frameworks that incorporate reduction catalysts can be a growing field with promising results.

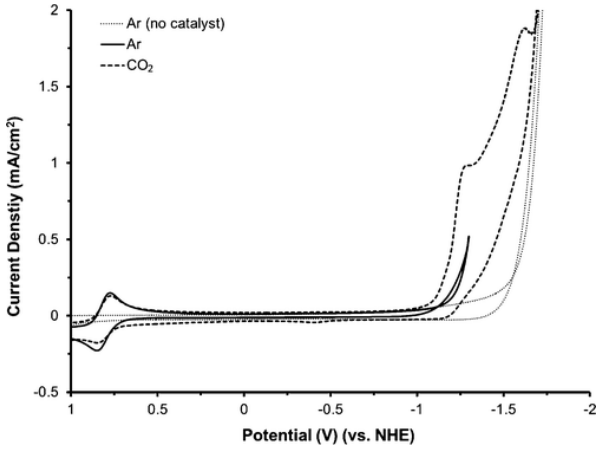

Figure 11: Cyclic Voltammetry of Ni (Cyclam) under Ar and CO_2 atmospheres Reprinted with permission from Inorg. Chem. 2012, 51, 3932−393[65]

A well-studied CO_2 reduction catalyst is Ni cyclam (cyclam = 1,4,8,11-tetraazacyclotetradecane). The pendant nitrogens in the heterocycle give proximal hydrogens that are important for CO_2 reduction reactions.[65] Figure 11 shows the reactivity of Ni(cyclam) under Ar and CO_2 atmospheres. Cyclam has previously been incorporated into a MOF, VPI-100.[83] Carboxylic acid groups were added to each end of the macrocycle to create a bidentate linker capable of binding to metal nodes for MOF. The cyclam in both its nickel and copper forms was found to activate CO_2 for a cycloaddition to various epoxides when heated.[84] The VPI-100 MOF has not been previously explored for its electrochemical applications which is shown in a future chapter.

1.6 References

(1) *Sunshot 2030*. https://www.energy.gov/eere/solar/sunshot-2030

(2)S. E. I. *Solar Industry Research Data*. 2023.

(3) Sharma, S.; Jain, K. K.; Sharma, A. Solar Cells: In Research and Applications—A Review. *Materials Sciences and Applications* **2015**, *06* (12), 1145-1155. DOI: 10.4236/msa.2015.612113.

(4) Gibbons, B.; Cai, M.; Morris, A. J. A Potential Roadmap to Integrated Metal Organic Framework Artificial Photosynthetic Arrays. *Journal of the American Chemical Society* **2022**, *144* (39), 17723-17736. DOI: 10.1021/jacs.2c04144.

(5) Zhang, L.; Wang, Y. Decoupled Artificial Photosynthesis. *Angewandte Chemie International Edition* **2023**, *62* (23), e202219076. DOI: https://doi.org/10.1002/anie.202219076.

(6) Arote, S. A. Fundamentals and perspectives of lithium-ion batteries. In *Lithium-ion and Lithium–Sulfur Batteries*; IOP Publishing, 2022; pp 1-1-1-26. DOI: 10.1088/978-0-7503-4881-2ch1.

(7) Manthiram, A. Materials Challenges and Opportunities of Lithium Ion Batteries. *The Journal of Physical Chemistry Letters* **2011**, *2* (3), 176-184. DOI: 10.1021/jz1015422.

(8) Li, M.; Lu, J.; Chen, Z.; Amine, K. 30 Years of Lithium-Ion Batteries. *Advanced Materials* **2018**, *30* (33), 1800561. DOI: https://doi.org/10.1002/adma.201800561.

(9) Cai, M.; Loague, Q. R.; Zhu, J.; Lin, S.; Usov, P. M.; Morris, A. J. Ruthenium(ii)-polypyridyl doped zirconium(iv) metal–organic frameworks for solid-state electrochemiluminescence. *Dalton Transactions* **2018**, *47* (46), 16807-16812, 10.1039/C8DT03906B. DOI: 10.1039/C8DT03906B.

(10) Seh, Z. W.; Kibsgaard, J.; Dickens, C. F.; Chorkendorff, I.; Nørskov, J. K.; Jaramillo, T. F. Combining theory and experiment in electrocatalysis: Insights into materials design. *Science* **2017**, *355* (6321), eaad4998. DOI: doi:10.1126/science.aad4998.

(11) Richter, M. M. Electrochemiluminescence (ECL). *Chemical Reviews* **2004**, *104* (6), 3003-3036. DOI: 10.1021/cr020373d.

(12) Mortimer, R. J. Electrochromic Materials. *Annual Review of Materials Research* **2011**, *41* (Volume 41, 2011), 241-268. DOI: https://doi.org/10.1146/annurev-matsci-062910-100344.

(13) Gou, X.; Xing, Z.; Ma, C.; Zhu, J.-J. A Close Look at Mechanism, Application, and Opportunities of Electrochemiluminescence Microscopy. *Chemical & Biomedical Imaging* **2023**, *1* (5), 414-433. DOI: 10.1021/cbmi.2c00007.

(14) Cao, Q.; Puthongkham, P.; Venton, B. J. Review: new insights into optimizing chemical and 3D surface structures of carbon electrodes for neurotransmitter detection. *Analytical Methods* **2019**, *11* (3), 247-261, 10.1039/C8AY02472C. DOI: 10.1039/C8AY02472C.

(15) Zhao, H.; Liu, L.; Vellacheri, R.; Lei, Y. Recent Advances in Designing and Fabricating Self-Supported Nanoelectrodes for Supercapacitors. *Advanced Science* **2017**, *4* (10), 1700188. DOI: https://doi.org/10.1002/advs.201700188.

(16) Srinivasan, S. ELECTRODE/ELECTROLYTE INTERFACES: STRUCTURE AND KINETICS OF CHARGE TRANSFER. In *Fuel Cells: From Fundamentals to Applications*, Srinivasan, S. Ed.; Springer US, 2006; pp 27-92.

(17) Reed, S. K.; Madden, P. A.; Papadopoulos, A. Electrochemical charge transfer at a metallic electrode: A simulation study. *The Journal of Chemical Physics* **2008**, *128* (12). DOI: 10.1063/1.2844801 (acccessed 9/12/2024).

(18) Hong-Cai Zhou, J. R. L., and Omar M. Yaghi. Introduction to Metal–Organic Frameworks. *Chemical Reviews* **2012**, *112* (2), 673-674. DOI: 10.1021/cr300014x.

(19) Li, H.; Wang, K.; Sun, Y.; Lollar, C. T.; Li, J.; Zhou, H.-C. Recent advances in gas storage and separation using metal–organic frameworks. *Materials Today* **2018**, *21* (2), 108-121. DOI: https://doi.org/10.1016/j.mattod.2017.07.006.

(20) Cornell, H. D.; Zhu, Y.; Ilic, S.; Lidman, N. E.; Yang, X.; Matson, J. B.; Morris, A. J. Green-light-responsive metal–organic frameworks for colorectal cancer treatment. *Chemical Communications* **2022**, *58* (34), 5225-5228, 10.1039/D2CC00591C. DOI: 10.1039/D2CC00591C.

(21) Gibbons, B.; Cairnie, D. R.; Thomas, B.; Yang, X.; Ilic, S.; Morris, A. J. Photoelectrochemical water oxidation by a MOF/semiconductor composite. *Chemical Science* **2023**, *14* (18), 4672-4680, 10.1039/D2SC06361A. DOI: 10.1039/D2SC06361A.

(22) Shao, Q.; Yang, J.; Huang, X. The Design of Water Oxidation Electrocatalysts from Nanoscale Metal–Organic Frameworks. *Chemistry – A European Journal* **2018**, *24* (57), 15143-15155. DOI: https://doi.org/10.1002/chem.201801572.

(23) Johnson, B. A.; Bhunia, A.; Fei, H.; Cohen, S. M.; Ott, S. Development of a UiO-Type Thin Film Electrocatalysis Platform with Redox-Active Linkers. *Journal of the American Chemical Society* **2018**, *140* (8), 2985-2994. DOI: 10.1021/jacs.7b13077.

(24) Lin, S.; Pineda-Galvan, Y.; Maza, W. A.; Epley, C. C.; Zhu, J.; Kessinger, M. C.; Pushkar, Y.; Morris, A. J. Electrochemical Water Oxidation by a Catalyst-Modified Metal–Organic Framework Thin Film. *ChemSusChem* **2017**, *10* (3), 514-522. DOI: https://doi.org/10.1002/cssc.201601181.

(25) Baumann, A. E.; Burns, D. A.; Liu, B.; Thoi, V. S. Metal-organic framework functionalization and design strategies for advanced electrochemical energy storage devices. *Communications Chemistry* **2019**, *2* (1), 86. DOI: 10.1038/s42004-019-0184-6.

(26) Ahrenholtz, S. R.; Epley, C. C.; Morris, A. J. Solvothermal Preparation of an Electrocatalytic Metalloporphyrin MOF Thin Film and its Redox Hopping Charge-Transfer Mechanism. *Journal of the American Chemical Society* **2014**, *136* (6), 2464-2472. DOI: 10.1021/ja410684q.

(27) Thomas, B.; Morris, A. J. Chapter Five - Photoactive MOFs for CO2 activation utilizing earth abundant metals. In *Advances in Inorganic Chemistry*, van Eldik, R., Ford, P. C. Eds.; Vol. 83; Academic Press, 2024; pp 161-187.

(28) Wang, L.; Zhang, Y.; Li, X.; Xie, Y.; He, J.; Yu, J.; Song, Y. The MIL-88A-Derived Fe3O4-Carbon Hierarchical Nanocomposites for Electrochemical Sensing. *Scientific Reports* **2015**, *5* (1), 14341. DOI: 10.1038/srep14341.

(29) Zhou, W.; Tang, Y.; Zhang, X.; Zhang, S.; Xue, H.; Pang, H. MOF derived metal oxide composites and their applications in energy storage. *Coordination Chemistry Reviews* **2023**, *477*, 214949. DOI: https://doi.org/10.1016/j.ccr.2022.214949.

(30) Shit, S. C.; Mondal, I.; Pendem, S.; Bai, L.; Park, J. Y.; Mondal, J. MOF-Derived Bifunctional Iron Oxide and Iron Phosphide Nanoarchitecture Photoelectrode for Neutral Water Splitting. *ChemElectroChem* **2018**, *5* (19), 2842-2849. DOI: https://doi.org/10.1002/celc.201800744.

(31) Shin, S.; Shin, M. W. Nickel metal–organic framework (Ni-MOF) derived NiO/C@CNF composite for the application of high performance self-standing supercapacitor electrode. *Applied Surface Science* **2021**, *540*, 148295. DOI: https://doi.org/10.1016/j.apsusc.2020.148295.

(32) Bai, Y.; Dou, Y.; Xie, L.-H.; Rutledge, W.; Li, J.-R.; Zhou, H.-C. Zr-based metal–organic frameworks: design, synthesis, structure, and applications. *Chemical Society Reviews* **2016**, *45* (8), 2327-2367, 10.1039/C5CS00837A. DOI: 10.1039/C5CS00837A.

(33) Johnson, E. M.; Ilic, S.; Morris, A. J. Design Strategies for Enhanced Conductivity in Metal–Organic Frameworks. *ACS Central Science* **2021**, *7* (3), 445-453. DOI: 10.1021/acscentsci.1c00047.

(34) Yan, M.; Johnson, E. M.; Morris, A. J. Redox Hopping in Metal–Organic Frameworks through the Lens of the Scholz Model. *The Journal of Physical Chemistry Letters* **2023**, *14* (47), 10700-10709. DOI: 10.1021/acs.jpclett.3c02641.

(35) Lin, S.; Usov, P. M.; Morris, A. J. The role of redox hopping in metal–organic framework electrocatalysis. *Chemical Communications* **2018**, *54* (51), 6965-6974, 10.1039/C8CC01664J. DOI: 10.1039/C8CC01664J.

(36) Cai, M.; Loague, Q.; Morris, A. J. Design Rules for Efficient Charge Transfer in Metal–Organic Framework Films: The Pore Size Effect. *The Journal of Physical Chemistry Letters* **2020**, *11* (3), 702-709. DOI: 10.1021/acs.jpclett.9b03285.

(37) Cardon, J. M.; Krueper, G.; Kautz, R.; Fabian, D. M.; Angsono, J.; Chen, H.-Y.; Ardo, S. Reconciliation of Differences in Apparent Diffusion Coefficients Measured for Self-Exchange

Electron Transfer between Molecules Anchored to Mesoporous Titanium Dioxide Thin Films. *ACS Applied Materials & Interfaces* **2021**, *13* (35), 41396-41404. DOI: 10.1021/acsami.9b19096.

(38) Bard, A. J.; Faulkner, L. R. *Electrochemical Methods: Fundamentals and Applications*; John Wiley & Sons, Inc, 2000.

(39) Schröder, U.; Oldham, K. B.; Myland, J. C.; Mahon, P. J.; Scholz, F. Modelling of solid state voltammetry of immobilized microcrystals assuming an initiation of the electrochemical reaction at a three-phase junction. *Journal of Solid State Electrochemistry* **2000**, *4* (6), 314-324. DOI: 10.1007/s100080000130.

(40) Celis-Salazar, P. J.; Cai, M.; Cucinell, C. A.; Ahrenholtz, S. R.; Epley, C. C.; Usov, P. M.; Morris, A. J. Independent Quantification of Electron and Ion Diffusion in Metallocene-Doped Metal–Organic Frameworks Thin Films. *Journal of the American Chemical Society* **2019**, *141* (30), 11947-11953. DOI: 10.1021/jacs.9b03609.

(41) Nicholson, R. S.; Shain, I. Theory of Stationary Electrode Polarography. Single Scan and Cyclic Methods Applied to Reversible, Irreversible, and Kinetic Systems. *Analytical Chemistry* **1964**, *36* (4), 706-723. DOI: 10.1021/ac60210a007.

(42) Kumar, A.; Li, J.; Inge, A. K.; Ott, S. Electrochromism in Isoreticular Metal–Organic Framework Thin Films with Record High Coloration Efficiency. *ACS Nano* **2023**, *17* (21), 21595-21603. DOI: 10.1021/acsnano.3c06621.

(43) Siu, J. C.; Fu, N.; Lin, S. Catalyzing Electrosynthesis: A Homogeneous Electrocatalytic Approach to Reaction Discovery. *Accounts of Chemical Research* **2020**, *53* (3), 547-560. DOI: 10.1021/acs.accounts.9b00529.

(44) Shatskiy, A.; Lundberg, H.; Kärkäs, M. D. Organic Electrosynthesis: Applications in Complex Molecule Synthesis. *ChemElectroChem* **2019**, *6* (16), 4067-4092. DOI: https://doi.org/10.1002/celc.201900435.

(45) Fan, L.; Tu, Z.; Chan, S. H. Recent development of hydrogen and fuel cell technologies: A review. *Energy Reports* **2021**, *7*, 8421-8446. DOI: https://doi.org/10.1016/j.egyr.2021.08.003.

(46) Matheu, R.; Garrido-Barros, P.; Gil-Sepulcre, M.; Ertem, M. Z.; Sala, X.; Gimbert-Suriñach, C.; Llobet, A. The development of molecular water oxidation catalysts. *Nature Reviews Chemistry* **2019**, *3* (5), 331-341. DOI: 10.1038/s41570-019-0096-0.

(47) Shen, J. R. The Structure of Photosystem II and the Mechanism of Water Oxidation in Photosynthesis. *Annu Rev Plant Biol* **2015**, *66*, 23-48. DOI: 10.1146/annurev-arplant-050312-120129 From NLM.

(48) Das, B.; Rahaman, A.; Shatskiy, A.; Verho, O.; Kärkäs, M. D.; Åkermark, B. The Impact of Ligand Carboxylates on Electrocatalyzed Water Oxidation. *Accounts of Chemical Research* **2021**, *54* (17), 3326-3337. DOI: 10.1021/acs.accounts.1c00298.

(49) Rüttinger, W.; Dismukes, G. C. Synthetic Water-Oxidation Catalysts for Artificial Photosynthetic Water Oxidation. *Chemical Reviews* **1997**, *97* (1), 1-24. DOI: 10.1021/cr950201z.

(50) Yagi, M.; Kaneko, M. Molecular Catalysts for Water Oxidation. *Chemical Reviews* **2001**, *101* (1), 21-36. DOI: 10.1021/cr980108l.

(51) Liu, F.; Concepcion, J. J.; Jurss, J. W.; Cardolaccia, T.; Templeton, J. L.; Meyer, T. J. Mechanisms of Water Oxidation from the Blue Dimer to Photosystem II. *Inorganic Chemistry* **2008**, *47* (6), 1727-1752. DOI: 10.1021/ic701249s.

(52) Wasylenko, D. J.; Ganesamoorthy, C.; Henderson, M. A.; Koivisto, B. D.; Osthoff, H. D.; Berlinguette, C. P. Electronic Modification of the [RuII(tpy)(bpy)(OH2)]2+ Scaffold: Effects on Catalytic Water Oxidation. *Journal of the American Chemical Society* **2010**, *132* (45), 16094-16106. DOI: 10.1021/ja106108y.

(53) Chen, Z.; Concepcion, J. J.; Hu, X.; Yang, W.; Hoertz, P. G.; Meyer, T. J. Concerted O atom–proton transfer in the O—O bond forming step in water oxidation. *Proceedings of the National Academy of Sciences* **2010**, *107* (16), 7225-7229. DOI: doi:10.1073/pnas.1001132107.

(54) Lin, S.; Ravari, A. K.; Zhu, J.; Usov, P. M.; Cai, M.; Ahrenholtz, S. R.; Pushkar, Y.; Morris, A. J. Insight into Metal–Organic Framework Reactivity: Chemical Water Oxidation Catalyzed by a [Ru(tpy)(dcbpy)(OH2)]2+-Modified UiO-67. *ChemSusChem* **2018**, *11* (2), 464-471. DOI: https://doi.org/10.1002/cssc.201701644.

(55) Bao, H.; Dilbeck, P. L.; Burnap, R. L. Proton transport facilitating water-oxidation: the role of second sphere ligands surrounding the catalytic metal cluster. *Photosynthesis Research* **2013**, *116* (2), 215-229. DOI: 10.1007/s11120-013-9907-1.

(56) Brahmachari, U.; Gonthier, J. F.; Sherrill, C. D.; Barry, B. A. Water Bridges Conduct Sequential Proton Transfer in Photosynthetic Oxygen Evolution. *The Journal of Physical Chemistry B* **2019**, *123* (21), 4487-4496. DOI: 10.1021/acs.jpcb.9b01523.

(57) Matheu, R.; Ertem, M. Z.; Benet-Buchholz, J.; Coronado, E.; Batista, V. S.; Sala, X.; Llobet, A. Intramolecular Proton Transfer Boosts Water Oxidation Catalyzed by a Ru Complex. *Journal of the American Chemical Society* **2015**, *137* (33), 10786-10795. DOI: 10.1021/jacs.5b06541.

(58) Song, N.; Concepcion, J. J.; Binstead, R. A.; Rudd, J. A.; Vannucci, A. K.; Dares, C. J.; Coggins, M. K.; Meyer, T. J. Base-enhanced catalytic water oxidation by a carboxylate–bipyridine Ru(II) complex. *Proceedings of the National Academy of Sciences* **2015**, *112* (16), 4935-4940. DOI: doi:10.1073/pnas.1500245112.

(59) Deng, H.; Doonan, C. J.; Furukawa, H.; Ferreira, R. B.; Towne, J.; Knobler, C. B.; Wang, B.; Yaghi, O. M. Multiple Functional Groups of Varying Ratios in Metal-Organic Frameworks. *Science* **2010**, *327* (5967), 846-850. DOI: doi:10.1126/science.1181761.

(60) Xia, Q.; Li, Z.; Tan, C.; Liu, Y.; Gong, W.; Cui, Y. Multivariate Metal–Organic Frameworks as Multifunctional Heterogeneous Asymmetric Catalysts for Sequential Reactions. *Journal of the American Chemical Society* **2017**, *139* (24), 8259-8266. DOI: 10.1021/jacs.7b03113.

(61) Lindsey, R. *Climate Change: Atomospheric Carbon Dioxide*. 2024. https://www.climate.gov/news-features/understanding-climate/climate-change-atmospheric-carbon-dioxidehttps://netl.doe.gov/carbon-management/carbon-storage/faqs/carbon-dioxide-101#:~:text=Carbon%20dioxide%20occurs%20naturally%20in,percent)%20in%20the%20Earth's%20atmosphere.&text=Carbon%20dioxide%20is%20a%20minor,subsequently%20exhaled%20from%20the%20lungs. (accessed 2024 09/02).

(62) Dziejarski, B.; Serafin, J.; Andersson, K.; Krzyżyńska, R. CO2 capture materials: a review of current trends and future challenges. *Materials Today Sustainability* **2023**, 100483.

(63) Wang, J.; Fu, R.; Wen, S.; Ning, P.; Helal, M. H.; Salem, M. A.; Xu, B. B.; El-Bahy, Z. M.; Huang, M.; Guo, Z. Progress and current challenges for CO2 capture materials from ambient air. *Advanced Composites and Hybrid Materials* **2022**, *5* (4), 2721-2759.

(64) Meng, D.; Unluer, C.; Yang, E.-H.; Qian, S. Recent advances in magnesium-based materials: CO2 sequestration and utilization, mechanical properties and environmental impact. *Cement and Concrete Composites* **2023**, *138*, 104983.

(65) Froehlich, J. D.; Kubiak, C. P. Homogeneous CO2 Reduction by Ni(cyclam) at a Glassy Carbon Electrode. *Inorganic Chemistry* **2012**, *51* (7), 3932-3934. DOI: 10.1021/ic3001619.

(66) Qiao, J.; Liu, Y.; Hong, F.; Zhang, J. A review of catalysts for the electroreduction of carbon dioxide to produce low-carbon fuels. *Chemical Society Reviews* **2014**, *43* (2), 631-675.

(67) Nitopi, S.; Bertheussen, E.; Scott, S. B.; Liu, X.; Engstfeld, A. K.; Horch, S.; Seger, B.; Stephens, I. E. L.; Chan, K.; Hahn, C.; et al. Progress and Perspectives of Electrochemical CO2 Reduction on Copper in Aqueous Electrolyte. *Chemical Reviews* **2019**, *119* (12), 7610-7672. DOI: 10.1021/acs.chemrev.8b00705.

(68) Birdja, Y. Y.; Pérez-Gallent, E.; Figueiredo, M. C.; Göttle, A. J.; Calle-Vallejo, F.; Koper, M. T. M. Advances and challenges in understanding the electrocatalytic conversion of carbon dioxide to fuels. *Nature Energy* **2019**, *4* (9), 732-745. DOI: 10.1038/s41560-019-0450-y.

(69) Shen, J.; Kortlever, R.; Kas, R.; Birdja, Y. Y.; Diaz-Morales, O.; Kwon, Y.; Ledezma-Yanez, I.; Schouten, K. J. P.; Mul, G.; Koper, M. T. M. Electrocatalytic reduction of carbon dioxide to carbon monoxide and methane at an immobilized cobalt protoporphyrin. *Nature Communications* **2015**, *6* (1), 8177. DOI: 10.1038/ncomms9177.

(70) Lim, C. F. C.; Harrington, D. A.; Marshall, A. T. Effects of mass transfer on the electrocatalytic CO2 reduction on Cu. *Electrochimica Acta* **2017**, *238*, 56-63. DOI: https://doi.org/10.1016/j.electacta.2017.04.017.

(71) Kumar, B.; Brian, J. P.; Atla, V.; Kumari, S.; Bertram, K. A.; White, R. T.; Spurgeon, J. M. New trends in the development of heterogeneous catalysts for electrochemical CO2 reduction. *Catalysis Today* **2016**, *270*, 19-30. DOI: https://doi.org/10.1016/j.cattod.2016.02.006.

(72) Salehi-Khojin, A.; Jhong, H.-R. M.; Rosen, B. A.; Zhu, W.; Ma, S.; Kenis, P. J. A.; Masel, R. I. Nanoparticle Silver Catalysts That Show Enhanced Activity for Carbon Dioxide Electrolysis. *The Journal of Physical Chemistry C* **2013**, *117* (4), 1627-1632. DOI: 10.1021/jp310509z.

(73) Zheng, T.; Jiang, K.; Wang, H. Recent Advances in Electrochemical CO2-to-CO Conversion on Heterogeneous Catalysts. *Advanced Materials* **2018**, *30* (48), 1802066. DOI: https://doi.org/10.1002/adma.201802066.

(74) Zhang, H.; Liang, Q.; Xie, K. How to rationally design homogeneous catalysts for efficient CO2 electroreduction? *iScience* **2024**, *27* (2), 108973. DOI: https://doi.org/10.1016/j.isci.2024.108973.

(75) Whang, H. S.; Lim, J.; Choi, M. S.; Lee, J.; Lee, H. Heterogeneous catalysts for catalytic CO2 conversion into value-added chemicals. *BMC Chemical Engineering* **2019**, *1* (1), 9. DOI: 10.1186/s42480-019-0007-7.

(76) Saha, P.; Amanullah, S.; Dey, A. Selectivity in Electrochemical CO2 Reduction. *Accounts of Chemical Research* **2022**, *55* (2), 134-144. DOI: 10.1021/acs.accounts.1c00678.

(77) Huff, C. A.; Sanford, M. S. Cascade catalysis for the homogeneous hydrogenation of CO2 to methanol. *J Am Chem Soc* **2011**, *133* (45), 18122-18125. DOI: 10.1021/ja208760j.

(78) Nichols, A. W.; Machan, C. W. Secondary-Sphere Effects in Molecular Electrocatalytic CO2 Reduction. *Frontiers in Chemistry* **2019**, *7* (397), Review. DOI: 10.3389/fchem.2019.00397.

(79) Francke, R.; Schille, B.; Roemelt, M. Homogeneously Catalyzed Electroreduction of Carbon Dioxide—Methods, Mechanisms, and Catalysts. *Chemical Reviews* **2018**, *118* (9), 4631-4701. DOI: 10.1021/acs.chemrev.7b00459.

(80) Zhao, Y.; Zheng, L.; Jiang, D.; Xia, W.; Xu, X.; Yamauchi, Y.; Ge, J.; Tang, J. Nanoengineering Metal–Organic Framework-Based Materials for Use in Electrochemical CO2 Reduction Reactions. *Small* **2021**, *17* (16), 2006590. DOI: https://doi.org/10.1002/smll.202006590.

(81) Perfecto-Irigaray, M.; Albo, J.; Beobide, G.; Castillo, O.; Irabien, A.; Pérez-Yáñez, S. Synthesis of heterometallic metal–organic frameworks and their performance as electrocatalyst for CO2 reduction. *RSC Advances* **2018**, *8* (38), 21092-21099, 10.1039/C8RA02676A. DOI: 10.1039/C8RA02676A.

(82) Zhao, K.; Liu, Y.; Quan, X.; Chen, S.; Yu, H. CO2 Electroreduction at Low Overpotential on Oxide-Derived Cu/Carbons Fabricated from Metal Organic Framework. *ACS Applied Materials & Interfaces* **2017**, *9* (6), 5302-5311. DOI: 10.1021/acsami.6b15402.

(83) Zhu, J.; Usov, P. M.; Xu, W.; Celis-Salazar, P. J.; Lin, S.; Kessinger, M. C.; Landaverde-Alvarado, C.; Cai, M.; May, A. M.; Slebodnick, C.; et al. A New Class of Metal-Cyclam-Based Zirconium Metal–Organic Frameworks for CO2 Adsorption and Chemical Fixation. *Journal of the American Chemical Society* **2018**, *140* (3), 993-1003. DOI: 10.1021/jacs.7b10643.

(84) Zhu, J.; Liu, J.; Machain, Y.; Bonnett, B.; Lin, S.; Cai, M.; Kessinger, M. C.; Usov, P. M.; Xu, W.; Senanayake, S. D.; et al. Insights into CO2 adsorption and chemical fixation properties of VPI-100 metal–organic frameworks. *Journal of Materials Chemistry A* **2018**, *6* (44), 22195-22203, 10.1039/C8TA06383D. DOI: 10.1039/C8TA06383D.

2. Incorporation of Sulfonate Groups into Metal-Organic Frameworks for Increased Charge Transfer Capabilities

Benjamin Thomas, Quinn Smith, Minliang Yan, Amanda Morris

Abstract

Electrochromic materials exploit the change in absorbance of a compound after an electrochemical redox event to be used in applications like smart glass and segmented displays. Current applications use metal oxides; however, these materials are plagued by slow response times to applied potential changes. This study investigates a metal-organic framework (MOF) film loaded with a ruthenium redox carrier for its electrochromic capabilities. Initial studies showed a lack of charge percolation throughout the framework, giving an apparent diffusion coefficient, D_{app} of 3.6(±4.8) x10^{-8} cm^2/s and 55% converted. Incorporating sulfonate groups into the backbone of the MOF allowed for charge transfer throughout the MOF with a D_{app} around 7.8(±6.8)x10^{-8} cm^2/s and 100% conversion, the fastest reported diffusion coefficients in the MOF literature. The sulfonate group is hypothesized to break ion pairs, allowing for higher ionic conductivity, which facilitated fast and complete charge transfer.

2.1 INTRODUCTION

Electrochromic materials are redox-active materials that undergo reversible optical property changes when exposed to an applied potential bias. They are used in smart glass, segmented displays, and sensing materials. [1, 2] The most common electrochromics are metal oxides. Oxides exhibit favorable stability to prolonged electrochemical cycling. During the reduction of these oxides, small ions intercalate into their crystal structure, stabilizing the injected electrons, which in some cases results in broad spectral absorbance, e.g., V_2O_5. However, the de-intercalation process is slow; therefore, these materials are plagued by slow recovery of the initial spectral state. The metal oxides also lack versatility in tint color and synthetically tractable

improvements in the rate of switching.[3] Therefore, there is a desire to develop new electrochromic materials that exhibit similar stability, more rapid color change response, and tunable colors beyond broad spectrum.

Metal-organic frameworks (MOFs) are highly crystalline, porous frameworks consisting of metal oxide clusters bound by multidentate organic ligands.[4] The versatility of metal ions and polydentate linkers that can be combined has led to MOFs being explored for a variety of applications, including gas storage[5], catalysis[6-9], drug delivery[10], and energy storage.[11] MOF thin films grown on electrode surfaces can be used for electrochemical applications. Understanding charge transfer mechanisms in these porous frameworks is important for uses in electrocatalysis, battery, and long-range charge transfer applications.[12] Several mechanisms of charge transfer have been explored for porous frameworks, including through-space, through-bond, redox hopping, and guest-promoted.[13] The MOF's crystalline nature, coupled with the insulating properties of common MOF nodes, electronically isolates the redox units in locked positions in the framework. Thus, the dominant charge transfer mechanism is redox hopping, i.e., self-exchange electron transfer is coupled to the diffusion of counterbalancing ions through the MOF pores.[14, 15] The diffusion of both the electrons and ions contributes to the overall charge transfer kinetics giving an apparent diffusion coefficient, D_{app}. The Morris group has previously investigated the charge transfer properties of these materials through the Scholz Model.[15] The Scholz model defines the movement of charge through a microporous particle on an electrode surface. By using the Scholz model, the bottleneck of charge transport was determined to be the diffusion of the counterbalancing ions.[14] On average, MOFs exhibit redox charge transfer with D_{app} of 1-3x10^{-10} cm^2/s.[16] Previous reports of electrochromic MOFs incorporate redox active linkers such as porphyrins or naphthalenediimide (NDI) derivatives.[17] The incorporation of the electrochromic redox linkers

allows absorbance to be used to monitor charge transfer within MOFs while determining the percent conversion of the redox centers. The Ott group developed a series of NDI-based MOFs with different linker lengths, changing the pore aperture of the grown MOFs.[17] The increase in pore size did not increase the switching rate of the MOF films as they all displayed similar D_{app} values of $1x10^{-10}$ cm^2/s. Similar diffusion rates indicate that the bottleneck of the charge transfer is not the pore size, so other methods to increase charge transport rates must be explored.

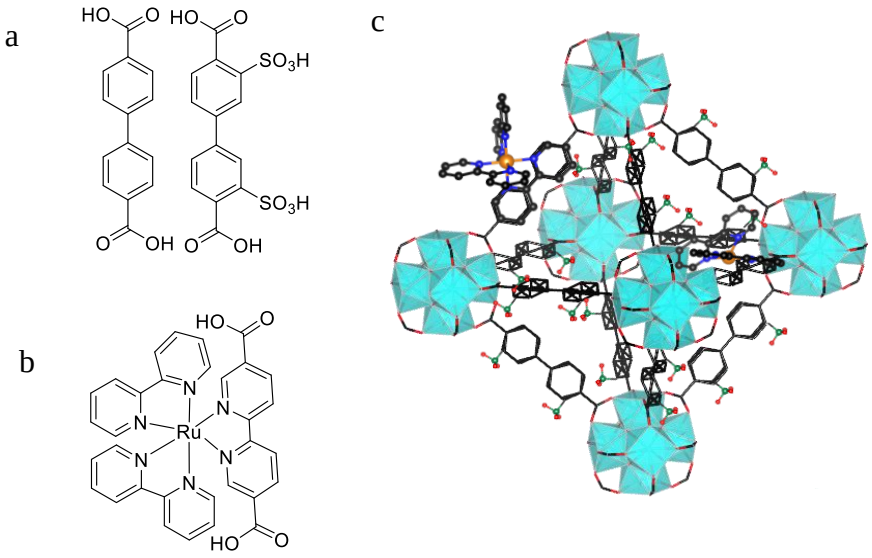

Figure 12: Linker structures of a) BPDC and BPDC-SO_3H b) RuBPY and c) single cage of RuBPY-UiO-67-SO_3H

Herein, we report the redox-hopping-driven electrochromic response of UiO-67 MOF films with electrochromic $Ru(bpy)_2(bpy\text{-}(COOH)_2)$ (bpy = 2,2′-bipyridine; bpy-$(COOH)_2$ = 5,5′-dicarboxylic acid-2,2′-bipyridine) (RuBPY) linkers incorporated along with the substituted biphenyl dicarboxylic acid in a multivariate (MTV) approach, shown in Figure 1. MTV MOFs allow for the incorporation of multiple functional groups in locked positions that lead to improved activity compared to the sum of their parts. The Morris group has previously incorporated RuBPY, $Ru(bpy)_2(bpy\text{-}(COOH)_2)$ into UiO-67 to study photophysical properties.[18] The incorporation of RuBPY is limited to one RuBPY per Zr node due to the confined pore space of the UiO-67

structure. The low ratio of redox centers can make the distance between them a barrier for charge transfer, making many of the RuBPY electrochemically inaccessible. The native RuBPY-UiO-67 MOF films showed slow charge transfer rates with D_{app} of 3.6(±4.8) x10^{-8} across 55% of the film. Interestingly, adding sulfonate groups to the native BPDC linkers improved charge transport through the RUBPY-UiO-67-SO_3H MOF, giving a D_{app} of 7.8(±6.8) x10^{-8} 100% of the film. The full charge transfer in the MOF allows for the use of the material in electrochromic applications. Complete oxidation of the RuBPY centers allows for complete color change as opposed to limited change in absorbance. The completely reversible color change would make the material more attractive for electrochromic applications

2.2 METHODS

BPDC-SO_3H Synthesis

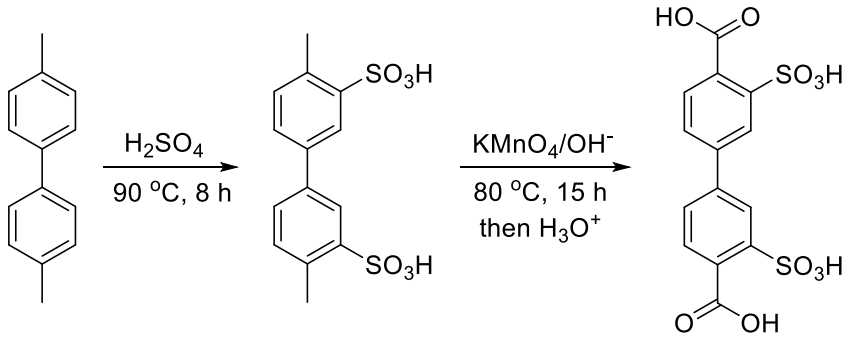

Figure 13: Synthesis Procedure for BPDC-SO_3H

Biphenyl-3,3′-disulfonyl-4,4′-dicarboxylic acid (BPDC-SO_3H) was synthesized via a previously reported procedure.[19] Briefly, 4,4′-dimethylbiphenyl was stirred and heated in concentrated sulfuric acid at 90 °C for 8 h. After the solution was cooled to room temperature, acetonitrile and dichloromethane were added to precipitate out the intermediate product. The resultant precipitant, 3,3′-disulfonyl-4,4′-dimethylbiphenyl, was dried and dissolved in an aqueous sodium hydroxide solution before the addition of potassium permanganate. The purple solution was heated overnight

at 90 °C, and the brown solid was filtered out. The filtrate was acidified with HCl and placed in the fridge for 10 hours to precipitate the biphenyl-3,3′-disulfonyl-4,4′-dicarboxylic acid, which was then filtered and washed with 1 M HCl. NMR: (DMSO-*d6*, ppm): 7.85 (s,4H), 8.10 (s,2H).

RuBPY Synthesis

RuBPY, $(Ru(bpy)_2(bpy\text{-}(COOH)_2)Cl_2$ where bpy = 2,2′-bipyridine; bpy-$(COOH)_2$ = 5,5′-dicarboxylic acid-2,2′-bipyridine, was synthesized by adding $Ru(bpy)_2Cl_2$ (200 mg) and bpy-$(COOH)_2$ (160 mg) were added to a 3:1 ethanol/water mixture and refluxed overnight. The product was collected by rotary evaporation and recrystallized with methanol and diethyl ether. NMR: (DMSO-*d6*, ppm): 7.51 (t,2H), 7.60 (t,2H), 7.79 (d,2H), 7.86 (d,2H), 8.01 (d,2H), 8.17 (t,2H), 8.23 (t,2H), 8.53 (d,2H), 8.84 (d,2H), 8.88 (d,2H), 9.00 (d,2H).

Ru-UiO-67 Film Synthesis

Ru-UiO-67 films were prepared using a reported procedure.[20] $ZrCl_4$ (23 mg), 4,4′-biphenyl dicarboxylic acid (21 mg), and, RuBPY (20 mg) were added to a 6-dram scintillation vial. DMF,10 mL, and 90 µL of difluroroacetic acid were added, and the vial was sonicated to dissolve the reagents. Fluorine-doped tin oxide (FTO) glass slides were soaked in piranha solution, followed by sonication in alconox, water, and finally methanol before being placed in a 120 °C oven to dry. A cleaned FTO slide was placed in the vial, conductive side down. The vial was sealed and placed in a 120 °C oven for 24 h. The vials were removed and cooled to room temperature. The films were removed from the vial and rinsed with DMF and acetonitrile. The powder on the non-conductive sides was removed using a sodium hydroxide solution. The films were stored in MeCN for further use.

Ru-UiO-67-SO_3H films were prepared using the same procedure as above; however, the BPDC was substituted for BPDC-SO_3H (40 mg).

XRD

X-ray Diffraction patterns for the MOF films were collected on a Bruker D8 Discover Wide Angle X-ray Diffractometer. The measurements were collected from 2Θ values of 2° to 30° with a resolution of 0.02° at a rate of 0.25° per minute.

Electrochemical Measurements

Electrochemical measurements were conducted with a Pine Instruments Wavenow potentiostat using a three-electrode setup with the MOF film coated on an FTO slide as the working electrode, an Ag^{+}/AgCl reference electrode, and a platinum mesh counter electrode. All electrochemical experiments were done in 0.1 M $LiClO_4$ in MeCN.

For cyclic voltammetry measurements, the potential was swept from the OCP to 2000 mV vs. NHE, which was well past the $Ru^{II/III}$ couple. At least five sweeps were done until the current response was stable and the final cycle was reported. The scan rate was varied from 10 mV/s to 1000 mV/s to obtain various data points within this range for diffusion coefficient calculations.

Spectroelectrochemical Measurements

Absorbance measurements were taken on a Cary UV-vis-NIR spectrophotometer from Agilent Technologies. Spectral scan measurements were taken in MeCN from 800 nm to 200 nm at a scan rate of 600 nm per minute.

The molar extinction coefficients were collected in a specialized quartz cuvette from Pine Research Instrumentation. A solution of 7.67×10^{-5} M RuBPY in acetonitrile was used to fill the cell. A honeycomb electrode from Pine Research Instrumentation with a platinum working electrode and counter electrode was placed in the cell along with a Ag/AgCl reference electrode. The cuvette was loaded into the UV-vis and positioned so the light beam would go through the honeycomb electrode. An absorbance spectrum was taken to get the standard spectra of the RuBPY molecule.

A potential of 1.5 V vs. Ag/AgCl was applied for 5 min to oxidize the RuBPY at the electrode surface. The absorbance spectrum of the cell was then taken while holding the potential at 1.5 V vs. Ag/AgCl.

For kinetics measurements, the absorbance at the selected wavelength was tracked with data points collected every 0.033 s. The MOF film was placed in a glass cuvette so the beamline would travel directly through the film. The cuvette was filled with 0.1 M $LiClO_4$ MeCN, and a Ag/Ag^+ reference electrode and platinum wire counter electrode were placed in the cell without blocking the beamline. A standard spectral scan was taken to determine the λ max, and a cyclic voltammogram at 50 mv/s was taken to determine the $E_{1/2}$. A cyclic step chronoamperometry experiment was performed by applying 1800 mv vs. NHE and subsequently applying the open circuit potential; the two potentials were cycled up to 10 times as the absorbance at the λ_{max} was collected.

FTIR

FTIR on the MOF samples was done using an ATR crystal attachment. A background scan was taken and the MOF films were scraped off the FTO slide and collected into the sample holder where contact was made with the ATR crystal. The FTIR spectrum was taken from an average of 64 scans from 400 to 4000 wavenumbers.

2.3 Results and Discussion

MOF films of RuBPY-UiO-67 and RuBPY-UiO-67-SO_3H were solvothermally grown on transparent FTO electrode glass slides. The powder X-ray diffraction (PXRD) patterns for the synthesized MOFs closely match simulated UiO-67 patterns, Figure 3a. SEM images show characteristic octahedral crystals, consistent with the morphology of UiO-type MOFs, Figure 3b and 3c. The films shows several intergrown particles; however, the coverage of the film is still intact. Cross section SEM gave film thickness of 1-3μm.

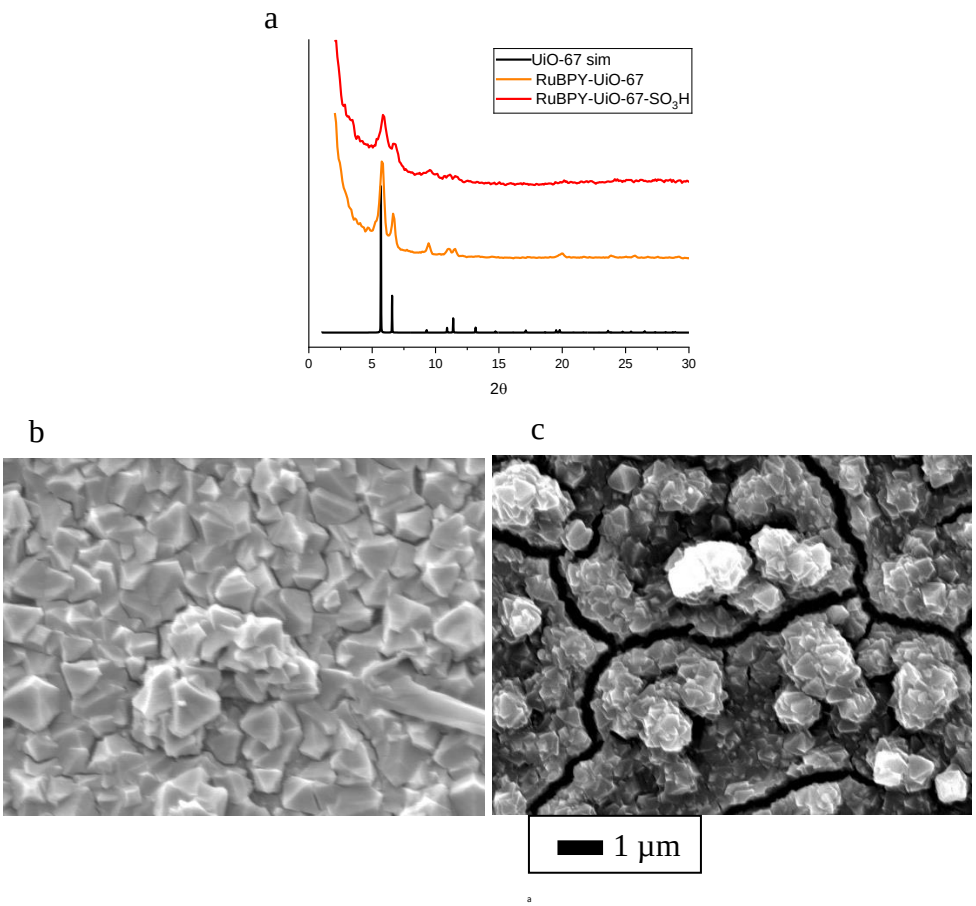

Figure 3: Characterization of MOF films: a) XRD patterns of Ru-UiO-67 and Ru-UiO-67-SO_3H, b) SEM image of a RuBPY-UiO-67 film, c) SEM image of a RuBPY-UiO-67-SO_3H film

There are several electrochemical techniques that can be used to determine the apparent diffusion coefficient.[21] Traditional electrochemical processes are diffusion-limited, following Fick's Laws. Electron transfer reactions occur at an electrode surface, and the diffusion of the redox species from the bulk to the surface is driven by a concentration gradient. The diffusion rate is quantitively

$$i = \frac{nFAc^0\sqrt{D_{app}}}{\sqrt{\pi t}} \qquad \text{Eq. 1}$$

determined via an apparent diffusion coefficient, D_{app}, Equation 1. When a MOF is grown on the surface of an electrode, the redox species are locked, and thus, the diffusional species are the

electrons themselves, as well as charge-balancing ions. The diffusion of the ions is much slower than that of electrons because of the inherent mass associated with the two species and limits the rate of charge transfer over longer distances.[14]

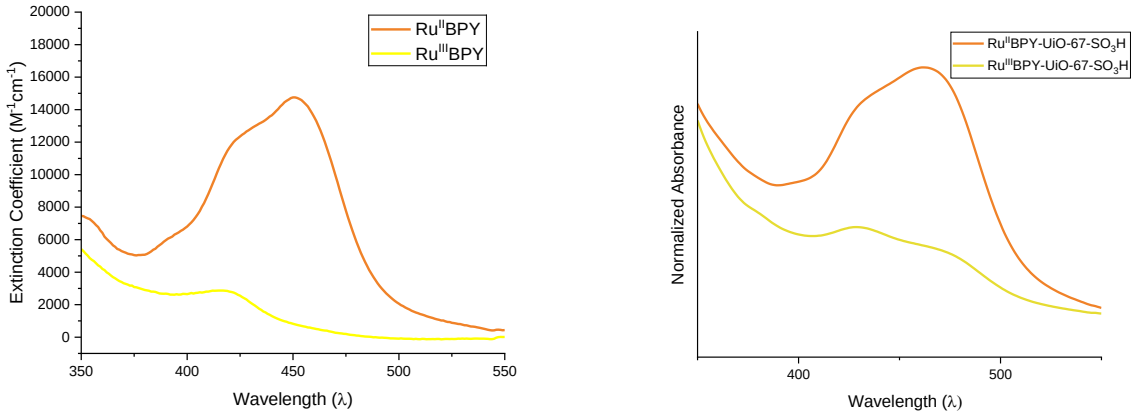

Figure 4: Molecular absorbance spectra of the $Ru^{2+}(bpy)_2$ (bpy-COOH) (orange) and the oxidized counterpart, $Ru^{3+}(bpy)_2$(bpy-COOH) (yellow) and the absorbance spectra of RuBPY-UiO-67-SO_3H before (orange) and after (yellow) oxidation

Incorporating the RuBPY chromophore gives the UiO-67 MOF film a similar absorption profile to the molecule in homogeneous solution. RuBPY in the Ru^{II} oxidation state displays the classic metal-ligand charge transfer (MLCT) absorption band with a λ_{max} at 456 nm and a molecular extinction coefficient of 14670 M^{-1} cm^{-1}. The molar extinction coefficient of the oxidized RuBPY in the Ru^{III} state at 456 nm is 978 M^{-1} cm^{-1}. The lower extinction coefficient results from the oxidized metal center making the MLCT transition more difficult due to the higher energies required to further oxidize the metal. The change in extinction coefficients can be used to track the conversion of the film from Ru^{II} to Ru^{III} by monitoring the absorbance as a function of time upon application of a potential bias. The diffusion of charge from the electrode surface throughout

the MOF can be calculated using the rate of absorbance change according to a modified Anson equation, Equation 2.

$$\Delta A = \frac{2A_{max}\sqrt{D_{app}t}}{d\sqrt{\pi}} \qquad \text{Eq. 2}$$

In Figure 5, the absorbance at 456 nm is tracked for the MOF film when a potential of 1600 mV vs. NHE was applied for 120 s followed by application of the original OCP of 50 mV vs. NHE for 180 s. The sulfonated MOF film sample, shown in black, shows an immediate 100% conversion of the Ru^{II} in the sample to Ru^{III}. Using Equation 2, the D_{app} for the RuBPY-UiO-67-SO_3H was calculated to be 2.3(±3.7) x10^{-7} cm^2/s. The native sample showed a smaller change in overall absorbance at 456 nm over a 600 second period. Maximum conversion is reached when only 55% of ruthenium is oxidized to Ru^{III}. The absorbance data suggests that not all the RuBPY centers are electrochemically accessible and converted from the ground state Ru^{II} to the oxidized $Ru^{III,}$ and the charge is not fully diffusing throughout the framework.

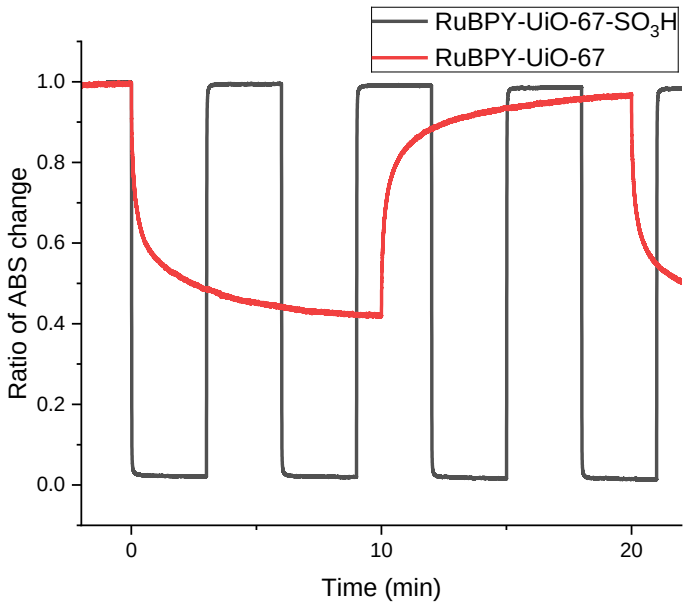

Figure 5: Kinetics plotsof absorbance upon oxidation and subsequent reduction of Ru-UiO-67 (red) and Ru-UiO-67-SO_3H (black) normalized to max absorbance in Ru^{II} state (1) and expected absorbance in Ru^{III} (0)

Scan rate-dependent cyclic voltammetry (CV) can also be used to determine the D_{app} for MOF thin films on the surface of an electrode according to Equation 3[22]

$$\lambda_e = d_f \sqrt{\frac{Fv}{D_{app}RT}} \qquad \text{Eq. 3}$$

At low scan rates, v, the current response follows surface-based charge transfer, meaning the diffusion coefficient is fast enough to keep up with the rate of potential change meaning the peak current is linear with v. At higher scan rates, the current follows a diffusional charge transfer process as the D_{app} is too slow to keep up with the potential sweep meaning the current response is linear against $v^{1/2}$ The crossover scan rate can be used to determine the D_{app} of the sample using Equation 3.

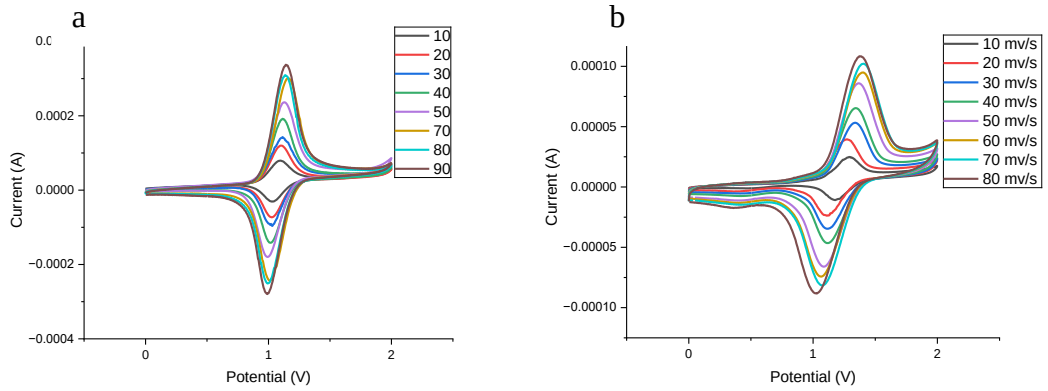

Figure 6: Cyclic voltammetry at varying scan rates for a) Ru-UiO-67 b) Ru-UiO-67-SO_3H

At this point, λ_e is about 1, and a D_{app} can be found for a known film thickness calculated from cross-section SEM images.[22] Figure 6 shows scan rate-dependent cyclic voltammetry of Ru-UiO-67 and Ru-UiO-67-SO_3H. The $E_{1/2}$ for both MOF films is shown to be 1.1 V vs. NHE, which

a

matches literature values for RuBPY.[20] For the Ru-UiO-67-SO3H sample in 6b, we see a shift in the correlation with *v* to $v^{1/2}$ between the 40 and 50 mV/s scan rates in Figures 7a and b.

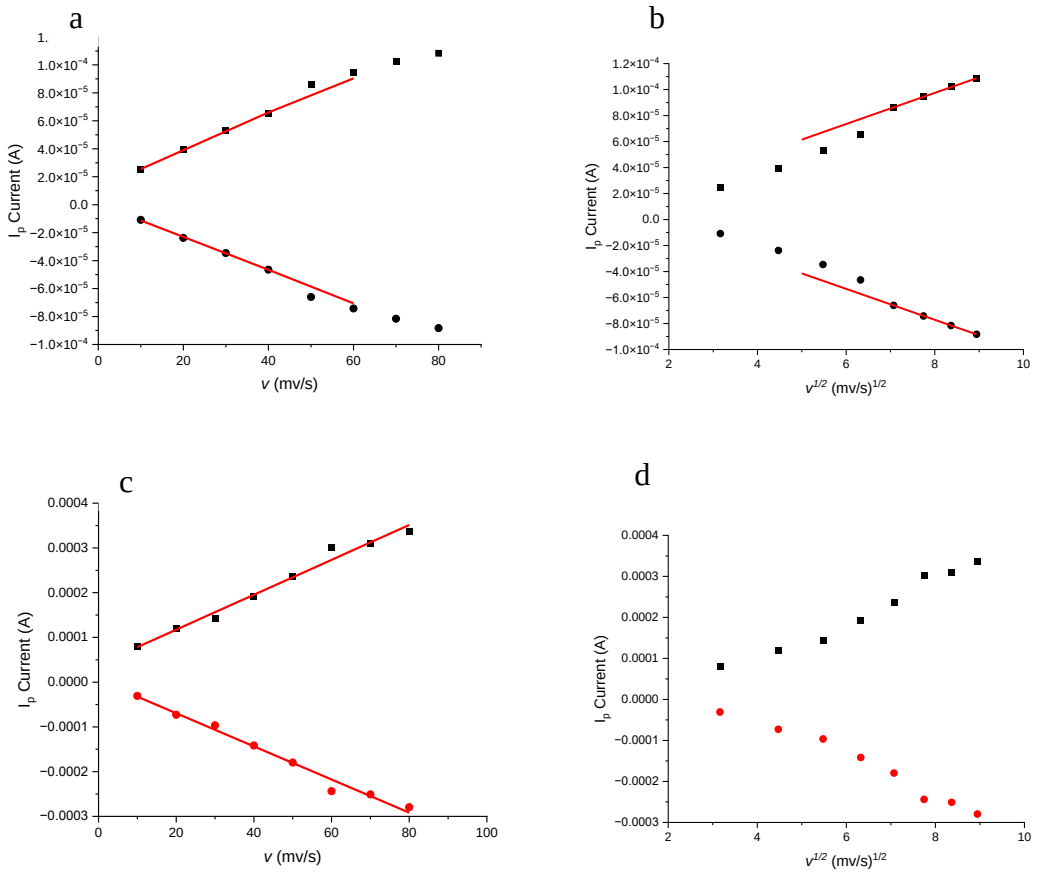

Figure 7: A) Peak current vs scan rate for RuBPY-UiO-67-SO$_3$H, B) Peak current vs square root scan rate for RuBPY-UiO-67-SO$_3$H C) Peak current vs scan rate for RuBPY-UiO-67, D) Peak current vs square root scan rate for RuBPY-UiO-67

Using a scan rate of 45 mV/s gives a D_{app} of 8.1x10^{-8} cm^2/s. For the native Ru-UiO-67, the scan rate dependence plot shown in Figure 6a, the transition to a diffusion-controlled process is never seen, which can indicate one of two things; the first is the electron transport is so fast that the scan rate will only show a surface-bound process. However, increasing the scan rate up to 1000 mV/s, Figure S3, does not show a diffusion-based process, which would indicate a D_{app} that is extremely fast and unlike any similar literature values. The second explanation is that only the Ru centers,

close to the surface, are being oxidized, and the rest of the material is electrochemically inactive. The absorbance data supports the second explanation.

Chronoamperometry, along with cyclic voltammetry, can also be used to determine the D_{app}. Diffusional electrochemical processes, namely the time-dependent current after a potential jump, are accurately modeled using the Cottrell equation, Eq. 2.[21] Where *i* is current, n is moles of electrons transferred, F is Faraday's constant (C/mol e^-), C^0 is the concentration of redox species (mol/cm^3), and t is time (s). The plot of current versus $1/t^{1/2}$ can be used to extract the D_{app}. Chronoamperometry was performed on the MOF samples by applying 1800 mV vs. Ag^+/AgCl to apply a potential beyond the $Ru^{II/III}$ couple. The current response for the films is shown in Figure 8.

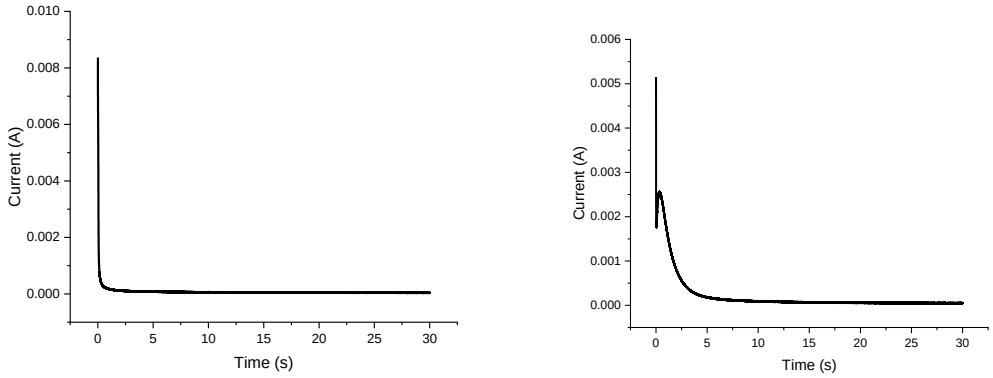

Figure 8: Chronoamperometry data for Ru-UiO-67 and Ru-UiO-67-SO_3H

The chronoamperometry response for the RuBPY-UiO-67 displays a standard Cottrell response. The response of RuBPY-UiO-67-SO_3H shows a standard max in current at the initial potential application and then a subsequent rise in current after 0.6 s. This rise in current is unexpected as it is not indicated in a Cottrell response. RuBPY only has one accessible oxidation from $Ru^{II/III}$ within the potential range applied, so a second electrochemical event is unlikely. A deviation from the Cottrell response suggests a drastic change in the electron transfer rate. The phenomenon was previously ovserved for redox active self-assembled monolayers of varying lengths bound to Ru

redox centers.[23] These fatty acid chains vary in length by as little as one carbon but show significant deviations in electron transfer rates upon constant electrolysis. Finklea and Hanshew propose two different explanations for the non-linear current response. The first is at high overpotentials, the resistance across the monolayer creates *iR* drop effects that lower the potential applied significantly enough to change the electron transfer rate. The second is the varying distance of electron travel changes the diffusion rate. At short times, the redox centers at the electrode surface dominate the rate of electron transfer while at longer times the more distant redox centers control the current response. Thus, the MOF samples could have varying distances of redox centers leading to a variety of D_{app} values which would lead to the non-linearity of the chronoamperometry plots.

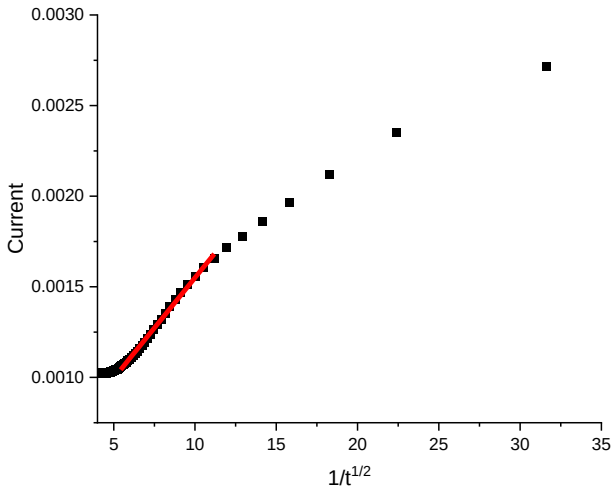

Figure 9: Cottrell plot of Ru-UiO-67-SO_3H film. Slope calculated in linear range on relevant time scale (red)

A Cottrell plot of the oxidation of Ru-UiO-67-SO_3H is shown in Figure 9. The D_{app} can be calculated using the slope of the line for the linear portion of the plot. The D_{app} calculated using this method was 7.8(±6.8) x10^{-8} cm^2/s, which is within error of the CV method determination. The current plot can also be integrated to determine the charge transferred within the entire experiment.

This charge can be plotted against $t^{1/2}$ which can be modelled to Equation 6, also termed the Anson equation, where q is charge.

$$q = \frac{2nFAc^0\sqrt{D_{app}t}}{\sqrt{\pi}} \quad \text{Eq. 6}$$

From the slope of the Anson plot, Figure S4, the D_{app} was determined to be 1.1(±.97) x10^{-7} cm^2/s. The chronocoulometric method is also within error of both previous methods because the charge data is generated from the chronoamperometry data.

Table 1. Summary of calculated D_{app}s from various methods for Ru-UiO-67-SO_3H

METHOD	D_{app} (cm^2/s)
CV	8.6(±3.6) x10^{-8}
Cottrell	7.8(±6.8) x10^{-8}
Anson (electrochemical)	1.1(±.97) x10^{-7}
Anson (spectrochemical)	2.3(±3.7) x10^{-7}

Table 1 shows the calculated D_{app}s using various techniques for the RuBPY-UiO-67-SO_3H. The D_{app}s are within error of each other, indicating the likelihood that the accurate D_{app} of the MOF is close to 1.26x10^{-7} cm^2/s. The same calculations cannot be done for the native sample because all the methods assume full oxidation of the thin film, therefore the lack of percolation throughout the Ru-UiO-67 makes any D_{app} meaningless.

The data above shows that the Ru-UiO-67-SO_3H sample has far higher conductivity than the Ru-UiO-67 counterpart. Given the ambipolar nature of redox hopping, i.e., both an electron and an ion need to diffuse, it is likely that the –SO_3H groups modify electron or ion transport rates. A couple of theories were explored to explain the sulfonate's role in charge transfer. The first was that the BPDC-SO_3H groups themselves were redox-active and could mediate charge transport.

However, no electrochemical signature was observed for a -SO_3H-derived UiO-67 within a reasonable electrochemical window compared to RuBPY shown in Figure S4. The second theory relates our structure to that of polyelectrolytes. Polyelectrolytes are polymers consisting of repeating units that contain an ionizable species.[24] When dissolved in solutions, the ionic groups disassociate and create a charged polymer backbone. Polyelectrolytes with sulfate functional groups quickly deprotonate in solution because of their low pKa.[25] Incorporating the negatively charged sulfate groups has improved the conductivity in batteries because the sulfate groups attract the Li^+ in the $LiClO_4$, freeing up the ClO_4^- increasing the ionic conductivity.[26] The native MOF lacking the charged functional groups on the biphenyl linkers has a higher concentration of the contact ion pair, $LiClO_4$. To further support this theory, FTIR measurements were done to measure the presence of lithium. MOF films after electrolysis were scrapped off the FTO slide and measured using ATR-FTIR. Figure 10 shows the sulfonated sample has a large peak appear at 1075 wavenumbers after electrolysis indicative of lithium sulfate found in the sample.[27] The RuBPY-UiO-67 MOF film did not see this same peak as the sulfate groups are not present for the Li^+ to bind.

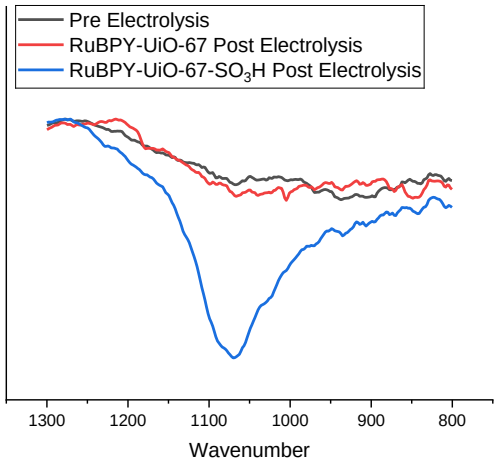

Figure 10: ATR-FTIR of MOF samples before electrolysis (black), RuBPY-UiO-67 post electrolysis (red) and RuTPY-UiO-67-SO_3H post electrolysis (blue)

In the sulfonated MOF, the Li^+ cations are attracted to the charged sulfate groups on the MOF, and thus, the concentration of free ClO_4^- increases, promoting charge transfer and allowing the entire sample to be oxidized.

2.4 CONCLUSION

In this work, the electrochromic behavior of two MOFs, RuBPY-UiO-67 and RuBPY-UiO-67-SO_3H were investigated. Despite including the same redox active center, RuBPY, at the same concentration, the electrochromic response of Ru-UiO-67-SO_3H was more complete (55% vs. 100%) and occurred more rapidly. Cyclic voltammetry and spectroelectrochemistry support a lack of charge percolation through Ru-UiO-67 and surface-limited redox activity. Whereas the Ru-UiO-67-SO_3H displayed classic diffusional transport with an apparent diffusion coefficient measured via a combination of methods to be $1x10^{-7}$ cm^2/s, to our knowledge the largest coefficient reported for a MOF to date. We hypothesize that incorporating charged groups breaks ion pairs, enabling increased charge propagation throughout the framework as opposed to surface-limited oxidation. The results highlight the value of multivariate MOFs in electrochemical applications,

where redox activity can be tuned significantly by easy modification of proximal but independent linkers.

2.5 REFERENCES

(1) Xu, T.; Walter, E. C.; Agrawal, A.; Bohn, C.; Velmurugan, J.; Zhu, W.; Lezec, H. J.; Talin, A. A. High-contrast and fast electrochromic switching enabled by plasmonics. *Nat Commun* **2016**, *7*, 10479. DOI: 10.1038/ncomms10479 From NLM.

(2) Applications of electrochromic devices. In *Electrochromism and Electrochromic Devices*, Monk, P., Mortimer, R., Rosseinsky, D. Eds.; Cambridge University Press, 2007; pp 395-416.

(3) Mortimer, R. J. Electrochromic Materials. *Annual Review of Materials Research* **2011**, *41* (Volume 41, 2011), 241-268. DOI: https://doi.org/10.1146/annurev-matsci-062910-100344.

(4) Lee, S. J.; Telfer, S. G. Multicomponent Metal-Organic Frameworks. *Angewandte Chemie International Edition* **2023**, *62* (44), e202306341. DOI: https://doi.org/10.1002/anie.202306341.

(5) Li, H.; Wang, K.; Sun, Y.; Lollar, C. T.; Li, J.; Zhou, H.-C. Recent advances in gas storage and separation using metal–organic frameworks. *Materials Today* **2018**, *21* (2), 108-121. DOI: https://doi.org/10.1016/j.mattod.2017.07.006.

(6) Bavykina, A.; Kolobov, N.; Khan, I. S.; Bau, J. A.; Ramirez, A.; Gascon, J. Metal–Organic Frameworks in Heterogeneous Catalysis: Recent Progress, New Trends, and Future Perspectives. *Chemical Reviews* **2020**, *120* (16), 8468-8535. DOI: 10.1021/acs.chemrev.9b00685.

(7) Gibbons, B.; Bartlett, E. C.; Cai, M.; Yang, X.; Johnson, E. M.; Morris, A. J. Defect Level and Particle Size Effects on the Hydrolysis of a Chemical Warfare Agent Simulant by UiO-66. *Inorganic Chemistry* **2021**, *60* (21), 16378-16387. DOI: 10.1021/acs.inorgchem.1c02224.

(8) Lin, S.; Pineda-Galvan, Y.; Maza, W. A.; Epley, C. C.; Zhu, J.; Kessinger, M. C.; Pushkar, Y.; Morris, A. J. Electrochemical Water Oxidation by a Catalyst-Modified Metal–Organic Framework Thin Film. *ChemSusChem* **2017**, *10* (3), 514-522. DOI: https://doi.org/10.1002/cssc.201601181.

(9) Gibbons, B.; Cairnie, D. R.; Thomas, B.; Yang, X.; Ilic, S.; Morris, A. J. Photoelectrochemical water oxidation by a MOF/semiconductor composite. *Chemical Science* **2023**, *14* (18), 4672-4680, 10.1039/D2SC06361A. DOI: 10.1039/D2SC06361A.

(10) Cornell, H. D.; Zhu, Y.; Ilic, S.; Lidman, N. E.; Yang, X.; Matson, J. B.; Morris, A. J. Green-light-responsive metal–organic frameworks for colorectal cancer treatment. *Chemical Communications* **2022**, *58* (34), 5225-5228, 10.1039/D2CC00591C. DOI: 10.1039/D2CC00591C.

(11) Baumann, A. E.; Burns, D. A.; Liu, B.; Thoi, V. S. Metal-organic framework functionalization and design strategies for advanced electrochemical energy storage devices. *Communications Chemistry* **2019**, *2* (1), 86. DOI: 10.1038/s42004-019-0184-6.

(12) Li, H.; Wang, Z.; Chen, L.; Huang, X. Research on Advanced Materials for Li-ion Batteries. *Advanced Materials* **2009**, *21* (45), 4593-4607. DOI: https://doi.org/10.1002/adma.200901710.

(13) Johnson, E. M.; Ilic, S.; Morris, A. J. Design Strategies for Enhanced Conductivity in Metal–Organic Frameworks. *ACS Central Science* **2021**, *7* (3), 445-453. DOI: 10.1021/acscentsci.1c00047.

(14) Cai, M.; Loague, Q.; Morris, A. J. Design Rules for Efficient Charge Transfer in Metal–Organic Framework Films: The Pore Size Effect. *The Journal of Physical Chemistry Letters* **2020**, *11* (3), 702-709. DOI: 10.1021/acs.jpclett.9b03285.

(15) Yan, M.; Johnson, E. M.; Morris, A. J. Redox Hopping in Metal–Organic Frameworks through the Lens of the Scholz Model. *The Journal of Physical Chemistry Letters* **2023**, *14* (47), 10700-10709. DOI: 10.1021/acs.jpclett.3c02641.

(16) Johnson, B. A.; Bhunia, A.; Fei, H.; Cohen, S. M.; Ott, S. Development of a UiO-Type Thin Film Electrocatalysis Platform with Redox-Active Linkers. *Journal of the American Chemical Society* **2018**, *140* (8), 2985-2994. DOI: 10.1021/jacs.7b13077.

(17) Kumar, A.; Li, J.; Inge, A. K.; Ott, S. Electrochromism in Isoreticular Metal–Organic Framework Thin Films with Record High Coloration Efficiency. *ACS Nano* **2023**, *17* (21), 21595-21603. DOI: 10.1021/acsnano.3c06621.

(18) Maza, W. A.; Morris, A. J. Photophysical Characterization of a Ruthenium(II) Tris(2,2′-bipyridine)-Doped Zirconium UiO-67 Metal–Organic Framework. *The Journal of Physical Chemistry C* **2014**, *118* (17), 8803-8817. DOI: 10.1021/jp501140r.

(19) Zhou, L.-J.; Deng, W.-H.; Wang, Y.-L.; Xu, G.; Yin, S.-G.; Liu, Q.-Y. Lanthanide–Potassium Biphenyl-3,3′-disulfonyl-4,4′-dicarboxylate Frameworks: Gas Sorption, Proton Conductivity, and Luminescent Sensing of Metal Ions. *Inorganic Chemistry* **2016**, *55* (12), 6271-6277. DOI: 10.1021/acs.inorgchem.6b00928.

(20) Cai, M.; Loague, Q. R.; Zhu, J.; Lin, S.; Usov, P. M.; Morris, A. J. Ruthenium(ii)-polypyridyl doped zirconium(iv) metal–organic frameworks for solid-state electrochemiluminescence. *Dalton Transactions* **2018**, *47* (46), 16807-16812, 10.1039/C8DT03906B. DOI: 10.1039/C8DT03906B.

(21) Cardon, J. M.; Krueper, G.; Kautz, R.; Fabian, D. M.; Angsono, J.; Chen, H.-Y.; Ardo, S. Reconciliation of Differences in Apparent Diffusion Coefficients Measured for Self-Exchange Electron Transfer between Molecules Anchored to Mesoporous Titanium Dioxide Thin Films. *ACS Applied Materials & Interfaces* **2021**, *13* (35), 41396-41404. DOI: 10.1021/acsami.9b19096.

(22) Johnson, B. A.; Beiler, A. M.; McCarthy, B. D.; Ott, S. Transport Phenomena: Challenges and Opportunities for Molecular Catalysis in Metal–Organic Frameworks. *Journal of the American Chemical Society* **2020**, *142* (28), 11941-11956. DOI: 10.1021/jacs.0c02899.

(23) Finklea, H. O.; Hanshew, D. D. Electron-transfer kinetics in organized thiol monolayers with attached pentaammine(pyridine)ruthenium redox centers. *Journal of the American Chemical Society* **1992**, *114* (9), 3173-3181. DOI: 10.1021/ja00035a001.

(24) Fu, J.; Fares, H. M.; Schlenoff, J. B. Ion-Pairing Strength in Polyelectrolyte Complexes. *Macromolecules* **2017**, *50* (3), 1066-1074. DOI: 10.1021/acs.macromol.6b02445.

(25) Akahane, T.; Takeuchi, S.; Minakata, A. Conductimetric titration of polyelectrolytes having sulfate and carboxyl groups. *Polymer Bulletin* **1990**, *24* (4), 437-444. DOI: 10.1007/BF00294098.

(26) Zhang, H.; Li, C.; Piszcz, M.; Coya, E.; Rojo, T.; Rodriguez-Martinez, L. M.; Armand, M.; Zhou, Z. Single lithium-ion conducting solid polymer electrolytes: advances and perspectives. *Chemical Society Reviews* **2017**, *46* (3), 797-815, 10.1039/C6CS00491A. DOI: 10.1039/C6CS00491A.

(27) Information, N. C. f. B. *PubChem Compound Summary for CID 66320, Lithium sulfate*. 2024. https://pubchem.ncbi.nlm.nih.gov/compound/Lithium-sulfate (accessed 2024 December 7).

SI

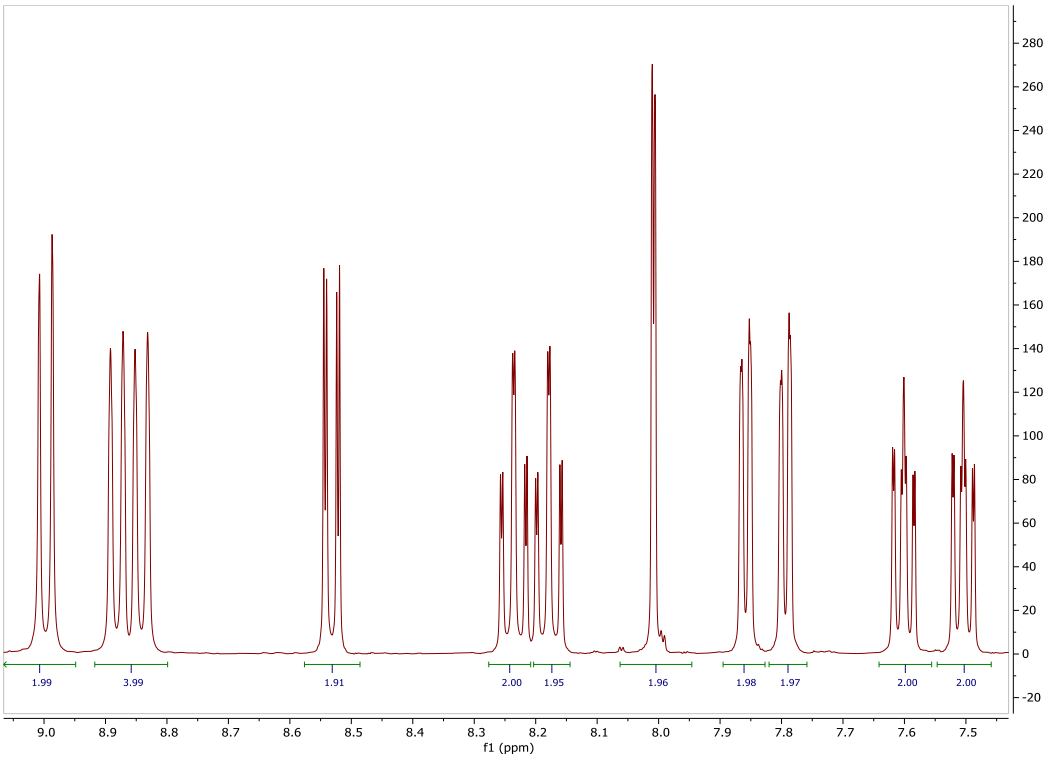

Figure S1: 400 MHz NMR of RuBPY in d_6-DMSO

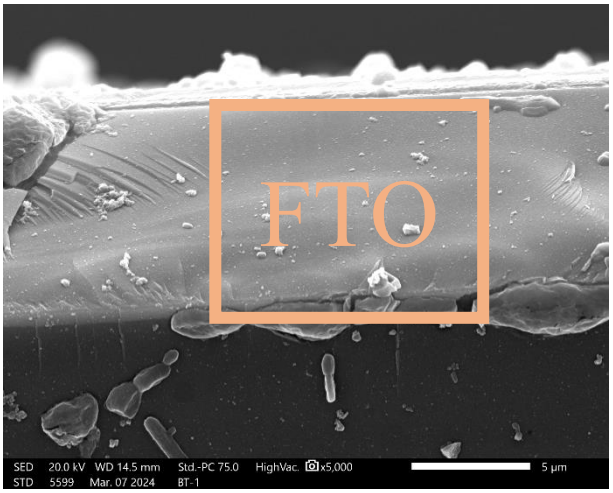

Figure S2: Cross Section SEM of RuBPY-UiO-67-SO_3H film on FTO

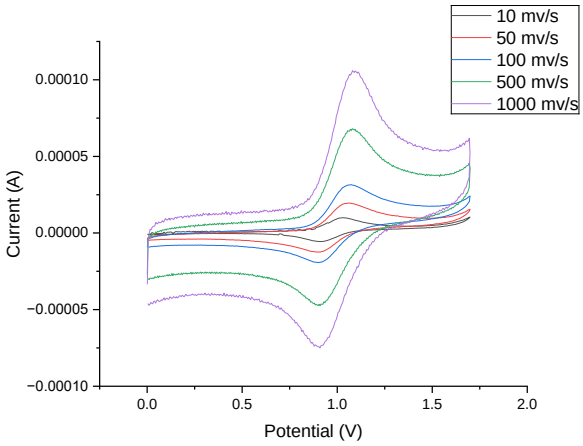

Figure S3: Scan Rate Dependence up to 1000 mV/s for RuBPY-UiO-67

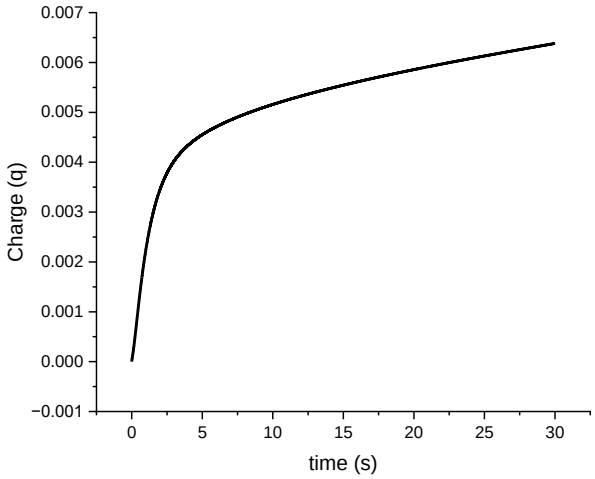

Figure S3: Anson Plot from Current Response for RuTPY-UiO-67-SO_3H

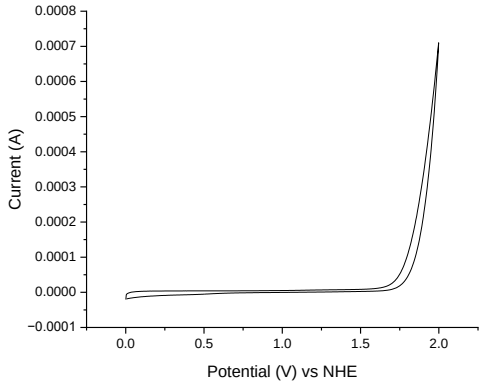

Figure S4: CV for catalyst free UiO-67-SO_3H

3. Incorporation of Ion Transport Chains into Metal-Organic Frameworks for Improved Water Oxidation

Ben Thomas, Quinn Smith, Minliang Yan, and Amanda Morris

ABSTRACT

The climate crisis has created a need for new, clean energy resources to mitigate the CO_2 emissions from the combustion of fossil fuels. Hydrogen fuel cells and carbon dioxide reduction powered by solar energy are two technologies that are key to creating a carbon-neutral future.[1] Water oxidation, or the conversion of water into oxygen and protons, is a crucial component of both reactions. Polypyridyl ruthenium complexes have a rich history of being highly active in electrochemical water oxidation. Our group previously incorporated these complexes into metal-organic frameworks (MOF) to overcome the complexes' low stability and recyclability in homogeneous solution.[2] Due to water oxidation's pH-dependent nature, incorporation of proton management has shown to increase reactivity.[3, 4] Incorporating a proton transfer chain into the MOF backbone should shuttle these protons away from the active site to increase turnover for oxygen evolution. To this end, we incorporated -SO_3H groups onto the biphenyl linkers of UiO-67 loaded with a catalytically active ruthenium complex, RuTPY: [Ru(tpy)(dcbpy)Cl]PF_6, tpy = 2,2′:6′,2″-terpyridine and dcbpy = 5,5-dicarboxy-2,2′-bipyridine. The sulfonated MOF showed an improved rate of oxygen evolution of 2.5 times compared to the RuTPY-UiO-67 MOF containing just the biphenyl linkers and RuTPY. The RuTPY-UiO-67 MOF film had a turnover of 10 per Ru atom, while the RuTPY-UiO-67-SO_3H MOF film had a turnover of 25 per Ru atom after an hour of electrolysis at 1.7 V vs. NHE. Using spectroelectrochemistry, the RuTPY-UiO-67-SO_3H showed improved redox conductivity, increasing electrochemically accessible ruthenium within the framework from 55% to 100%. The results highlight the capabilities of a multivariate approach to MOF synthesis for active catalysis to enable synergistic effects within the confined pores of the framework.

3.1 INTRODUCTION

Water oxidation plays a crucial role in the future of clean energy. The process of water oxidation, shown in equation 1, involves the conversion of water molecules into oxygen gas, protons, and electrons. The electrons generated are needed in reduction processes such as carbon dioxide (CO_2) reduction and proton reduction for use in combustion reactions and fuel cells.[1, 5, 6] Highly efficient water oxidation replaces the need for sacrificial electron donors in the reduction reactions, making the processes genuinely catalytic.

$$2H_2O \rightarrow O_2 + 4H^+ + 4e^- \quad (1)$$

Polypyridyl ruthenium complexes are well-studied water oxidation catalysts that exhibit some of the fastest turnover rates within the literature.[7] These catalysts are hindered by their instability in solution, the high cost of Ru, and difficult recyclability that stems from the need to separate a homogenous compound from the solution. To address these issues, monolayers of molecular catalysts have been built on electrode surfaces.[8-10] These monolayers showed similar redox properties to their solution counterparts while eliminating the diffusional aspect of the charge transfer steps. These monolayers are limited by the surface area of the electrode meaning the amount of catalyst incorporated is capped, limiting catalytic efficiency.

MOFs are highly crystalline, porous materials with high surface area. These properties have led to MOF investigations for several applications, including gas storage and separation[9], drug delivery[11], electrode materials[12], and catalysis[13-16]. The highly ordered nature of these materials leads to multiple isolated, accessible active sites spaced throughout the framework.

Incorporating commonly used homogenous catalysts into the backbone of the MOF leads to higher turnovers than their natural counterparts because their stability is increased through site isolation.[17-20] Several MOF films have been studied for their activity in CO_2 reduction and have

shown significant improvements over their homogenous counterparts.[21] Fewer studies have been done on MOF materials for water oxidation.[22, 23] Our group has previously incorporated RuTPY, a highly active water oxidation catalyst, into the backbone of UiO-67, a biphenyl-based Zr-MOF.[7,8] The results showed improved water oxidation and the ability to recycle the material for multiple catalytic runs.[2] While incorporating the catalyst alone has improved the oxidation efficiency, understanding the mechanism of both charge transfer and water oxidation within the framework can lead to increased efficiency of the MOF materials.

Water oxidation is one of the most studied reactions because of its pivotal role in photosynthesis. Photosystem II, responsible for the photochemical water oxidation step in photosynthesis, contains a $MnCaO_5$ active site responsible for oxygen generation.[13] The generated H^+s from the reaction are shuttled away to create a proton gradient necessary to drive ATP production. Proton transport is critical for continued oxygen production. Proton buildup around the active site increases the thermodynamic barrier for oxidation. The transport chain in Photosystem II is made up of surrounding amino acids that facilitate this proton transport. Amino acids with charged groups like aspartic acid, glutamic acid, lysine, and arginine make up the bulk of this proton transport channel. The order of amino acids is specially designed to generate a path of water molecules that can transfer the protons rapidly. A lack of defined surroundings besides solvent poses an issue for improving reactivity of traditionally synthesized molecular catalysts for water oxidation. A controlled environment surrounding the catalyst with distinct functional groups to could improve the oxidation efficiency. MOFs provide a unique answer to this problem. Utilizing the framework as a protein-like backbone, the MOF can be decorated with functional groups to achieve the desired ion transport. The modular nature of MOFs allows for the incorporation of both active water oxidation catalysts and molecules which can shuttle protons

away from the active sites. A multivariate strategy can be employed to incorporate linkers with active catalytic sites in combination with linkers containing desired functional groups for ion shuttling. Aiming to mimic nature, we can use charged functional groups such as sulfates to achieve a proton transport gradient.

Herein, we report the synthesis of a new multivariate MOF, RuTPY-UiO-67-SO_3H. The MOF contains two linkers; the known water oxidation catalyst, RuTPY, [Ru(tpy)(dcbpy)Cl]PF_6, where tpy = 2,2′:6′,2″-terpyridine and dcbpy = 5,5-dicarboxy-2,2′-bipyridine, and a disulfonated biphenyl dicarboxylic acid, 3,3'-disulfo-[1,1'-biphenyl]-4,4'-dicarboxylic acid. Incorporating both linkers primes the structure for synergistic effects by having the sulfate groups proximal to the active RuTPY catalyst, increasing water oxidation activity. A thin film of the MOF was grown on an FTO electrode. The deprotonated sulfonate groups bound to the native biphenyl linkers of UiO-67 create an ion transport chain away from active catalysis sites and show an increased rate of oxygen production per Ru active site.

The sulfonate groups were found to increase the rate of redox-hopping charge transport and thus the number of electrochemically accessible RuTPY active sites from 55% to 100%. We attribute this phenomenon to an increase in free ion concentration driven by a polyelectrolyte effect on $LiClO_4$ ion pair.

3.2 METHODS AND MATERIALS

3,3'-disulfo-[1,1'-biphenyl]-4,4'-dicarboxylic acid synthesis

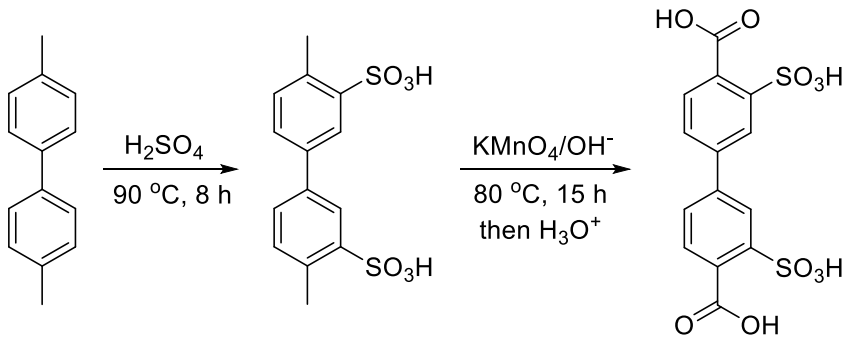

Figure 1: Synthesis scheme of the sulfonated biphenyl dicarboxylic acid through the sulfonation of dimethyl biphenyl followed by oxidation of methyl groups to carboxylic acids

The sulfonated biphenyl dicarboxylic acid linker, 3,3'-disulfo-[1,1'-biphenyl]-4,4'-dicarboxylic acid, was synthesized via a previously reported procedure.[14] Briefly, 4,4′-dimethyl biphenyl was stirred and heated in concentrated sulfuric acid at 90 °C for 8 h. After cooling to room temperature 100 mL of acetonitrile and dichloromethane were added to precipitate the product. The solid was filtered and dried then the sulfonated dimethyl-biphenyl was dissolved in an aqueous sodium hydroxide solution before the addition of potassium permanganate. The purple solution was heated to 80 °C overnight and filtered. The filtrate was acidified with HCl and placed in the fridge for 10 hours to precipitate the linker which was then filtered and washed with 1 M HCl. NMR 400 MHz: (DMSO-*d6*, ppm): 7.85 (s, 4H), 8.10 (s, 2H).

RuTPY Synthesis

RuTPY, [Ru(tpy)(dcbpy)Cl]PF_6, where tpy = 2,2′:6′,2″-terpyridine and dcbpy = 5,5-dicarboxy-2,2′ - bipyridine, was synthesized from a previously reported procedure in which $RuCl_3 \cdot xH_2O$ was refluxed with 2,2′:6′,2″-terpyridine in ethanol for 4 h.[24] The resulting brown precipitate was collected through filtration then dried in a 120 °C oven. The collected Ru(tpy)Cl_3 was dissolved in 3:1 ethanol:water along with 5,5-dicarboxy-2,2′-bipyridine and 1 mL of N-ethylmorpholine. The solution was refluxed overnight then filtered hot. The filtrate was reduced using rotary evaporation, and 10 mL of 1 M HCl was added to the solution, followed by 10 mL of saturated

NH_4PF_6 aqueous solution. The solution was placed in the fridge for 10 hours. The precipitate was filtered and washed with cold 1 M HCl and then dried. NMR 400 MHz: (DMSO-*d6*, ppm): 7.31 (m,2H), 7.61 (s,1H), 7.69 (m,2H), 7.99 (t,2H), 8.12 (d,1H), 8.28 (t,1H), 8.69 (m,3H), 8.79 (d,1H), 8.85 (d,2H), 9.15 (d,1H), 10.6(s,1H).

RuTPY-UiO-67 Synthesis

RuTPY-UiO-67 was synthesized from a literature procedure.[2] $ZrCl_4$, (21 mg), biphenyl dicarboxylic acid (20 mg), and RuTPY (18 mg), were added to a 6-dram scintillation vial along with 10 mL of dry DMF and 90 uL of difluoroacetic acid was added and the solution was sonicated for 10 min. A clean FTO slide was added to the vial laying diagonally across the solution with the conductive side down. The vial was capped and placed in an 120 °C oven for 24 h. The MOF vial was removed from the oven and allowed to cool to room temperature. The film was removed from solution and washed with DMF and water before being placed in water for 24 h to exchange the Cl ligand for an aqua ligand on the ruthenium catalyst. PXRD and SEM were collected to verify the identity and morphology of the MOF film.

The sulfonated MOF, RuTPY-UiO-67-SO_3H was made following the same procedure as the RuTPY-UiO-67 synthesis with the biphenyl dicarboxylic acid replaced with 3,3'-disulfo-[1,1'-biphenyl]-4,4'-dicarboxylic acid (41 mg).

PXRD

Powder X-ray Diffraction (PXRD) patterns were collected on a Rigaku Miniflex instrument (Cu Kα, λ= 1.5418 Å) from 2° to 30° with a resolution of 0.05° at a rate of 0.5° per min.

Electrochemical Methods

Electrochemical measurements were conducted using a Pine Instruments Wavenow potentiostat using a three-electrode arrangement with the MOF film coated on an FTO slide as the working

electrode, an Ag^+/AgCl reference electrode, and a platinum mesh counter electrode. Water oxidation studies were done in 0.1 M $LiClO_4$ adjusted to pH 6 using HCl. Bulk electrolysis was conducted at 1.70 V vs. NHE. O_2 production was measured with a Clarke-type dissolved oxygen probe (Unisense OX-NP). A blank FTO slide in a solution of potassium ferricyanide ($Fe^{II/III}$ $E_{1/2}$ = 0.361 V vs. NHE) was tested before every oxidation run to calibrate the reference electrode.

Absorbance Measurements

Absorbance measurements were taken on a Cary UV-Vis-NIR spectrophotometer. The full absorption spectra were taken from 800 nm to 200 nm at a speed of 600 nm per minute.

The molar extinction coefficients were collected in a specialized quartz cuvette from Pine Research Instrumentation. A solution of $9.54x10^{-5}$ M RuTPY in acetonitrile was used to fill the cell. A honeycomb electrode from Pine Research Instrumentation with a platinum working electrode and counter electrode was placed in the cell along with a Ag/AgCl reference electrode. The cuvette was loaded into the Uv-Vis and positioned so the light beam would go through the honeycomb electrode. An absorbance spectrum was taken to get the standard spectra of the RuTPY molecule. A potential of 1.2 V vs. Ag/AgCl was applied for 5 min to oxidize the RuTPY at the electrode surface. The absorbance spectrum of the cell was then taken while holding the potential at 1.2 V vs. Ag/AgCl.

For kinetics measurements, the absorbance at the selected wavelength was tracked with data points collected every 0.033 seconds. The MOF film was placed in a glass cuvette so the beamline would travel directly through the film. The cuvette was filled with 0.1 M $LiClO_4$ MeCN, and a Ag/Ag^+ reference electrode and platinum wire counter electrode were placed in the cell without blocking the beamline. A standard spectral scan was taken to determine the λ max, and a cyclic voltammogram at 50 mv/s was taken to determine the $E^{1/2}$. A cyclic step chronoamperometry

experiment was performed by applying 1.2 V vs. NHE and subsequently applying the open circuit potential; the two potentials were cycled up to 10 times as the absorbance at the λ max was collected.

3.3 RESULTS AND DISCUSSION

Figure 2 shows an idealized cage of the multivariate RuTPY-UiO-67-SO_3H MOF. The RuTPY catalyst is incorporated in a 1:5 ratio to the sulfonated biphenyl linkers, giving a ratio of one RuTPY per Zr node. The bulkiness of the terpyridine group limits the amount of catalyst that can be incorporated due to the constricted pore size of UiO-67.

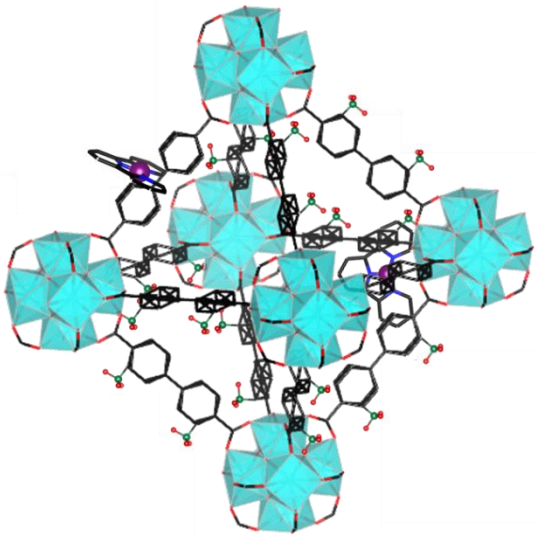

Figure 2: Idealized octahedral cage of Ru-TPY-UiO-67-SO_3H, Zr: Light blue, C: black, O: red, N: blue, and S: green

The PXRD patterns of both the MOF films agree with the simulated pattern of base UiO-67, indicating the ruthenium catalyst and sulfonated biphenyl linker were incorporated into the framework and did not alter the crystal structure of the three-dimensional framework. NMR analysis of degraded MOF showed the expected 1:5 ratio of Ru catalyst to linker. The SEM images of the thin films show the octahedral crystals indicative of a UiO-type MOF. Some of the crystals

appear to be intergrown among each other but the general octahedral structure holds for most of the microcrystals.

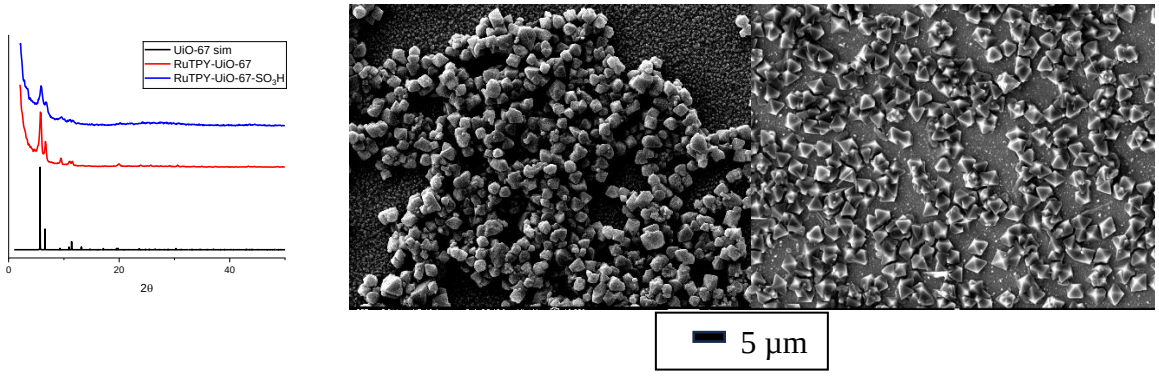

Figure 14: a) PXRD patterns for both MOFs compared to simulated UiO-67 and SEM images of b) RuTPY-UiO-67 and c) RuTPY-UiO-67-SO_3H

The PXRD patterns of both the MOFs agree with the simulated pattern of base UiO-67, indicating the ruthenium catalyst and sulfonated biphenyl linker were incorporated into the framework and did not alter the crystal structure of the three-dimensional framework. NMR analysis of degraded MOF showed the expected 1:5 ratio of Ru catalyst to linker. The SEM images of the thin films show the octahedral crystals indicative of a UiO-type MOF. Some of the crystals appear to be intergrown among each other but the general octahedral structure holds for most of the nanocrystals.

The total ruthenium amounts on the electrode were determined by UV-Vis of the degraded sample, Figure S2. The average amount of ruthenium found on the RuTPY-UiO-67 is $2.0(\pm0.42)x10^{-7}$ mol RuTPY. The average amount of ruthenium found on the RuTPY-UiO-67-SO_3H is $1.3(\pm0.3)x10^{-7}$ mol RuTPY.

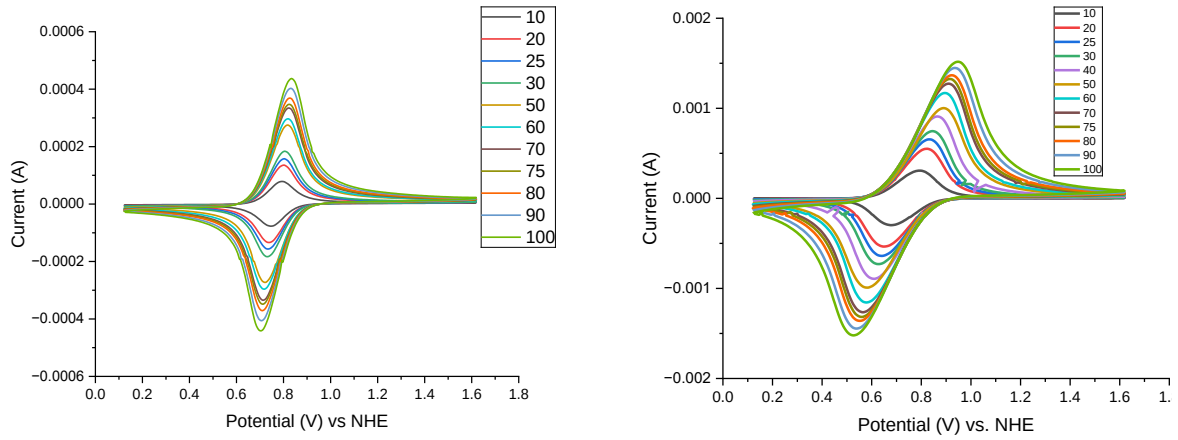

Figure 15: Scan rate dependent cyclic voltammetry from 10 to 100 mV/s for both a) RuTPY-UiO-67 and b) RuTPY-UiO-67-SO3H

Due to the insulating nature of the Zr nodes in UiO-67 and the isolated positions of the RuTPY redox centers, charge transfer in RuTPY-UiO-67 type MOFs occurs through a redox hopping mechanism.[25] The charge hops from redox center to redox center coupled with the diffusion of a charge balancing ion. Cyclic voltammograms in 0.1 M $LiClO_4$ acetonitrile show the redox response for RuTPY-UiO-67 and RuTPY-UiO-67-SO_3H, Figure 4. The $Ru^{II/III}$ couple is present with an $E_{1/2}$ at 0.770 V vs. NHE. Differential pulse voltammetry in Figure S4 shows a shoulder peak around 1.2 V vs. NHE which is attributed to the $Ru^{III/IV}$ couple.

Scan rate-dependent cyclic voltammetry can be used to determine the rate of the redox hopping within the framework known as the diffusion coefficient or D_{app}. At low scan rates, the MOF shows characteristic "surface-bound" redox behavior with the peak current being linear with v, while at fast scan rates, the charge transfer displays diffusion like behavior with peak currents being linear with $v^{1/2}$. The cyclic voltammograms shown in Figure 4 show the scan rate dependence for both RuTPY-UiO-67 and RuTPY-UiO-67-SO_3H MOF films. The RuTPY-UiO-67 film showed surface-like behavior for all scan rates up to 1000 mv/s indicating only the surface of the MOF is electrochemically active and there is a lack of diffusion throughout the MOF. The RuTPY-

UiO-67-SO_3H showed more peak separation and diffusion like behavior with a shift in the current response from surface to diffusion within the 50-60 mv/s range. Using equation 4, the transition scan rate can be used to find a D_{app} value by setting λ to 1. This would give a D_{app} of 8.3 x10^{-8} cm^2/s.

$$\lambda = d_f \sqrt{\frac{Fv}{D_{app}RT}} \tag{2}$$

As per previous reports, the diffusion of charge throughout the MOF film can be calculated using spectroelectrochemistry.[15-17] RuTPY is an electrochromic molecule where upon oxidation of Ru^{II} to Ru^{III}, spectral changes consistent with a visible color change from deep purple to pale yellow is observed.[18] The absorbance spectra in Figure 5 shows the absorbance of the RuTPY molecule in solution in the Ru^{II} and Ru^{III} oxidation states. The characteristic MLCT band has a λ_{max} of 527 nm. The extinction coefficient in the Ru^{II} of 23,221 $M^{-1}cm^{-1}$ and the oxidation of the complex shows a drop in this coefficient to 3,597 $M^{-1}cm^{-1}$. Using the modified Anson equation, equation 3, the change in absorbance upon oxidation at a potential beyond the $Ru^{II/III}$ redox couple can be used to calculate a D_{app}.

$$\Delta A = \frac{2A_{max}}{d_f} \sqrt{\frac{D_{app}t}{\pi}} \tag{3}$$

The parent and sulfonated MOF films were subjected to oxidation in 0.1 M $LiClO_4$ in acetonitrile at 1.2 V vs Ag/Ag^+, which is beyond the oxidative wave for $Ru^{II/III}$ shown in Figure 4. The change

in absorption was measured at 527 nm, the λ_{max} of the MLCT for RuTPY. The oxidized films were then reduced back to the ground state Ru^{II} by applying the open circuit potential.

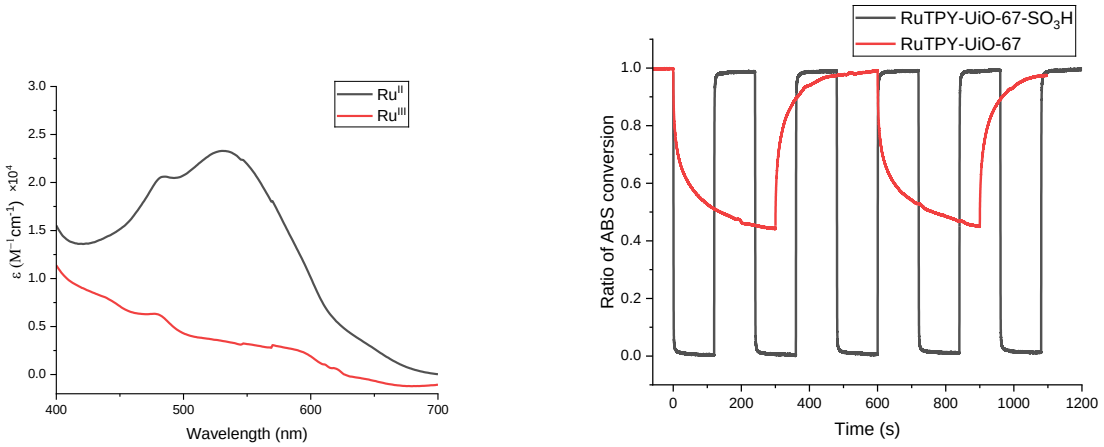

Figure 16: Molar extinction coefficient spectra of RuTPY in the Ru^{II} and Ru^{III} state and Absorbance plot of wavelength 527 nm upon oxidation and subsequent reduction for both RuTPY-UiO-67 and RuTPY-UiO-67-SO_3H

The RuTPY-UiO-67-SO_3H film saw an immediate drop in absorbance of over 85% which is indicative of the full conversion to Ru^{III} because the molar absorptivity for Ru^{III} is 85% lower than that of Ru^{II}. The absorbance returned fully to its initial amount, indicating the MOF was not degraded and the absorbance change is due to the oxidation of RuTPY to the Ru^{III} oxidation state. Oxidation and reduction were cycled several times to show stability in the absorbance change over at least 5 cycles. The D_{app} for the RuTPY-UiO-67-SO_3H was 3.1(±0.5)x10^{-7} cm^2/s.[19] In contrast, RuTPY-UiO-67, did not show a full color shift, reaching only 50% oxidation. The calculated diffusion coefficient for the RuTPY-UiO-67 is 4.7(±0.9)x10^{-11} cm^2/s over 55% of the MOF. The lack of full oxidation of the MOF indicates incomplete charge intercalation throughout the framework.

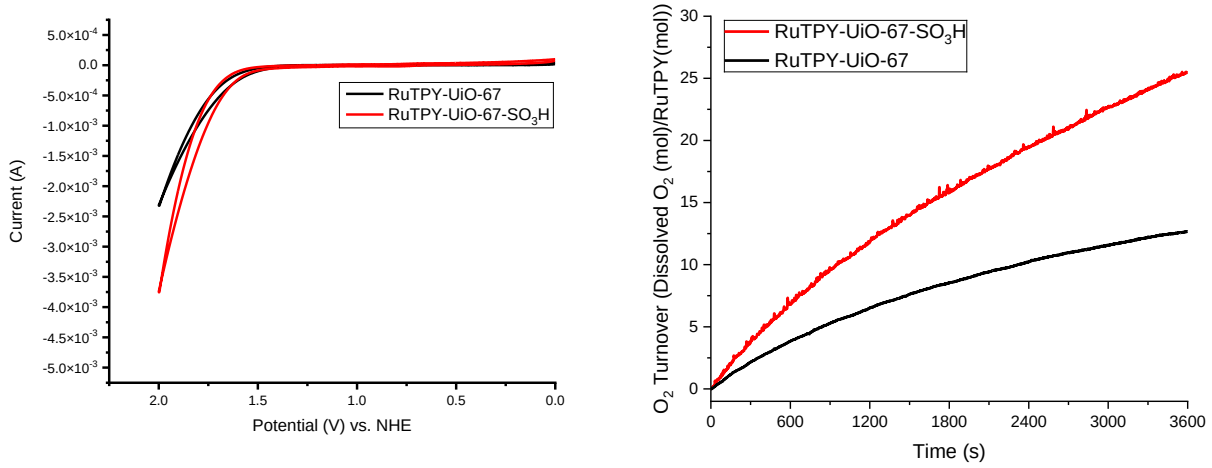

Figure 17: a) Cyclic voltammetry of MOF samples in 0.1 M $LiClO_4$ aqueous solution and b) turnover numbers for oxygen generation during bulk electrolysis of MOF films

The MOF films were tested for their electrochemical water oxidation capacity. The concentration of oxygen over time for both the RuTPY-UiO-67 and RuTPY-UiO-67-SO_3H is shown in Figure 3. The turnover rate for the RuTPY-UiO-67-SO_3H reaches an average of 25±3 mol of O_2 per Ru mol in an hour two times that of the native RuTPY-UiO-67 which only reaches 10±2 turnovers for oxygen. The thin films were tested for repeated reactivity and showed similar oxidation rates for multiple electrolysis periods when fresh electrolyte solution was replaced in the cell seen in Figure 7a. The retained reactivity indicates the MOF is not degrading into solution and the -SO_3H groups continue to provide increased reactivity. The MOF films were also confirmed to retain their crystallinity as shown in Figure 7b with the XRD of the MOF retaining its peak positions and intensities.

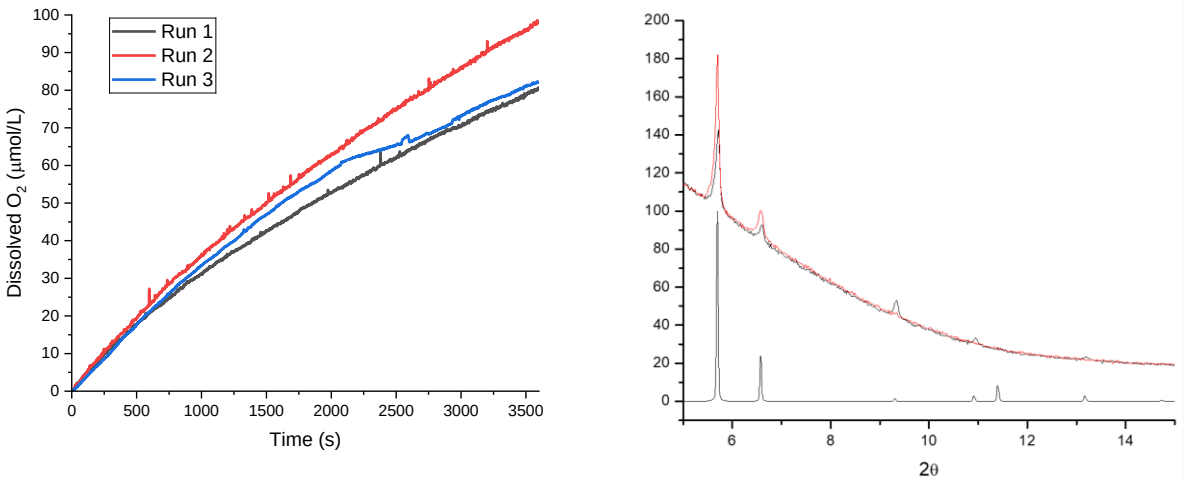

Figure 18: Reproducibility of RuTPY-UiO-67-SO3H films a)3 runs of the same film with fresh solution b) simulated pattern of UiO-67 (bottom), XRD of film pre-catalysis (black) and post-catalysis (red)

The lower turnover rate indicates an increase in thermodynamic barrier to the water oxidation which is likely due to the buildup of protons near the active site. The sustained increased rate of oxygen production indicates the sulfonate groups are aiding the catalysis in some way. While the RuTPY-UiO-67-SO_3H has all Ru within the MOF electrochemically accessible which would show increased activity, using the absorbance data, the RuTPY-UiO-67 has access to 55% of the Ru sites. The Ru-TPY-UiO-67 MOF then has $1.1x10^{-7}$ mol of electrochemically active Ru compared to the $1.3\ x10^{-7}$ mol for the RuTPY-UiO-67-SO_3H which is not 2.5 times more. The increase in reactivity is higher than the change of electrochemically accessible Ru indicates the sulfonate groups proximal to the active sites are contributing to the reactivity of the MOF film. Other reports have indicated the dangling -SO_3H groups have shown increased proton transport through a porous film.

To further confirm the involvement of the sulfonate groups in catalysis, the pH of the solution was lowered to shut down the ion transport capabilities by protonating the groups thus removing the charge. A drastic lowering in reactivity was seen when the pH was lowered to 2 with almost no

oxygen being produced. The pH was then returned to pH 6 and the initial high reactivity was returned.

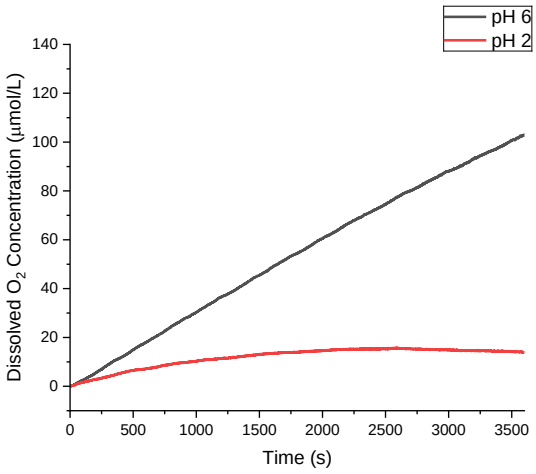

Figure 8: Reactivity of RuTPY-UiO-67-SO3H at pH 2(red) and pH 6(black)

3.4 CONCLUSION

We report the incorporation of sulfonate groups into the backbone of UiO-67 loaded with a known water oxidation catalyst, RuTPY by decorating the native biphenyl linkers within the framework. The incorporation of the proximal sulfonate groups within the confined space of the MOF intends to create a proton shuttle to remove generated H^+ near the active site to increase turnover similar to proximal amino acids within Photosystem II.[20] The RuTPY-UiO-67-SO_3H showed higher oxygen production per electrochemically active Ru atom compared to the RuTPY-UiO-67 with the -SO_3H film reaching 25 turnovers over an hour while the native RuTPY-UiO-67 only reached close to 10. The native MOF also showed a slowdown of reactivity over the course of oxidation which could be due to build up of protons near the ruthenium centers, decreasing the pH and increasing the thermodynamic barrier of water splitting. Charge transfer studies also showed an increase of charge diffusion throughout the sulfonated MOF. The sulfate ions lead to higher conductivity throughout the framework itself, allowing all RuTPY centers to be electrochemically

active for oxidation while the RuTPY-UiO-67 showed only 55% of the RuTPY could be electrochemically accessed making them useless. This work shows the power of a multivariate approach to MOFs and the synergistic effect that can be seen with the sulfonate functional groups and the water oxidation catalyst. The confined nature of MOFs should further be exploited to improve catalytic activity.

Supplemental Information

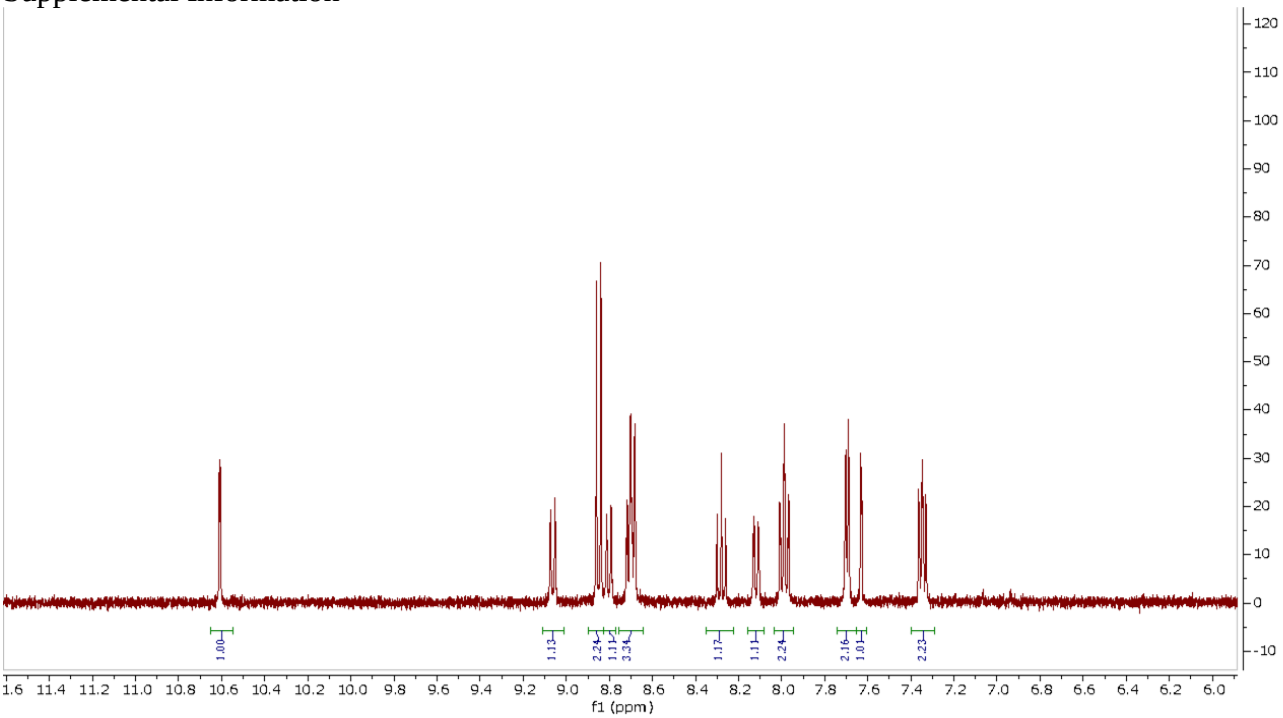

Figure S1: 1H 400 MHz NMR in DMSO of RuTPY complex

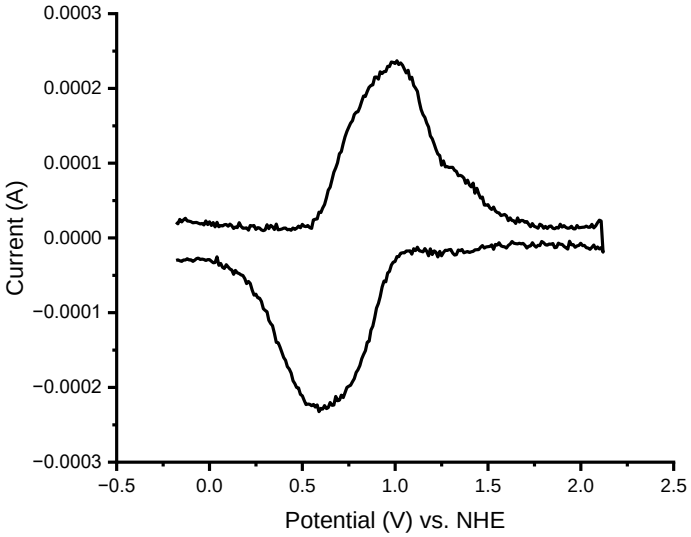

Figure S2: DPV curve of RuTPY-UiO-67-SO_3H

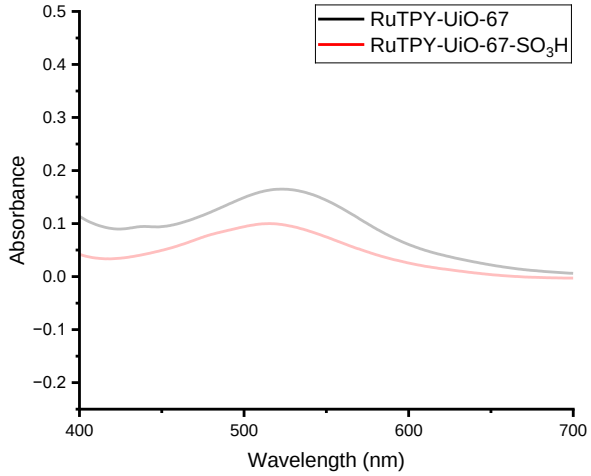

Figure S3: Absorbance spectra of the degraded MOFs

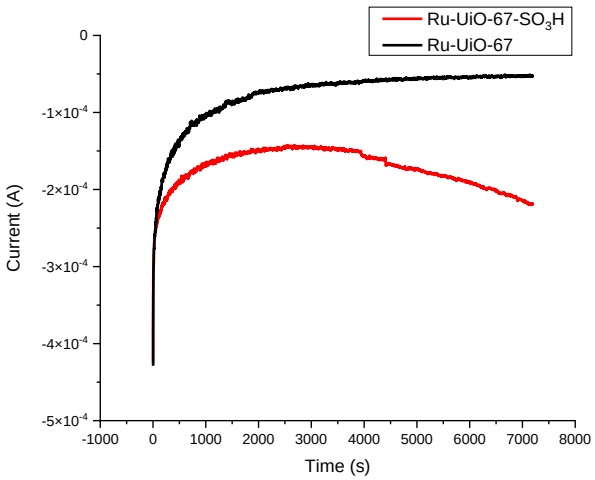

Figure S4: Chronoamperometry plots of bulk electrolysis runs for both MOF films

3.5 References

(1) Fan, L.; Tu, Z.; Chan, S. H. Recent development of hydrogen and fuel cell technologies: A review. *Energy Reports* **2021**, *7*, 8421-8446. DOI: https://doi.org/10.1016/j.egyr.2021.08.003.

(2) Lin, S.; Pineda-Galvan, Y.; Maza, W. A.; Epley, C. C.; Zhu, J.; Kessinger, M. C.; Pushkar, Y.; Morris, A. J. Electrochemical Water Oxidation by a Catalyst-Modified Metal–Organic Framework Thin Film. *ChemSusChem* **2017**, *10* (3), 514-522. DOI: https://doi.org/10.1002/cssc.201601181.

(3) Matheu, R.; Ertem, M. Z.; Benet-Buchholz, J.; Coronado, E.; Batista, V. S.; Sala, X.; Llobet, A. Intramolecular Proton Transfer Boosts Water Oxidation Catalyzed by a Ru Complex. *Journal of the American Chemical Society* **2015**, *137* (33), 10786-10795. DOI: 10.1021/jacs.5b06541.

(4) DePasquale, J.; Nieto, I.; Reuther, L. E.; Herbst-Gervasoni, C. J.; Paul, J. J.; Mochalin, V.; Zeller, M.; Thomas, C. M.; Addison, A. W.; Papish, E. T. Iridium Dihydroxybipyridine Complexes Show That Ligand Deprotonation Dramatically Speeds Rates of Catalytic Water Oxidation. *Inorganic Chemistry* **2013**, *52* (16), 9175-9183. DOI: 10.1021/ic302448d.

(5) Zhang, L.; Wang, Y. Decoupled Artificial Photosynthesis. *Angewandte Chemie International Edition* **2023**, *62* (23), e202219076. DOI: https://doi.org/10.1002/anie.202219076.

(6) Gibbons, B.; Cai, M.; Morris, A. J. A Potential Roadmap to Integrated Metal Organic Framework Artificial Photosynthetic Arrays. *Journal of the American Chemical Society* **2022**, *144* (39), 17723-17736. DOI: 10.1021/jacs.2c04144.

(7) Wasylenko, D. J.; Ganesamoorthy, C.; Henderson, M. A.; Koivisto, B. D.; Osthoff, H. D.; Berlinguette, C. P. Electronic Modification of the [RuII(tpy)(bpy)(OH2)]2+ Scaffold: Effects on Catalytic Water Oxidation. *Journal of the American Chemical Society* **2010**, *132* (45), 16094-16106. DOI: 10.1021/ja106108y.

(8) Figgemeier, E.; Constable, E. C.; Housecroft, C. E.; Zimmermann, Y. C. Self-Assembled Monolayers of Ru/Os Dinuclear Complexes: Probing Monolayer Structure and Interaction Energies by Electrochemical Means. *Langmuir* **2004**, *20* (21), 9242-9248. DOI: 10.1021/la048762l.

(9) Concepcion, J. J.; Binstead, R. A.; Alibabaei, L.; Meyer, T. J. Application of the Rotating Ring-Disc-Electrode Technique to Water Oxidation by Surface-Bound Molecular Catalysts. *Inorganic Chemistry* **2013**, *52* (19), 10744-10746. DOI: 10.1021/ic402240t.

(10) Chen, Z.; Concepcion, J. J.; Jurss, J. W.; Meyer, T. J. Single-Site, Catalytic Water Oxidation on Oxide Surfaces. *Journal of the American Chemical Society* **2009**, *131* (43), 15580-15581. DOI: 10.1021/ja906391w.

(11) Cornell, H. D.; Zhu, Y.; Ilic, S.; Lidman, N. E.; Yang, X.; Matson, J. B.; Morris, A. J. Green-light-responsive metal–organic frameworks for colorectal cancer treatment. *Chemical Communications* **2022**, *58* (34), 5225-5228, 10.1039/D2CC00591C. DOI: 10.1039/D2CC00591C.

(12) Baumann, A. E.; Burns, D. A.; Liu, B.; Thoi, V. S. Metal-organic framework functionalization and design strategies for advanced electrochemical energy storage devices. *Communications Chemistry* **2019**, *2* (1), 86. DOI: 10.1038/s42004-019-0184-6.

(13) Fu, Y.; Sun, D.; Chen, Y.; Huang, R.; Ding, Z.; Fu, X.; Li, Z. An Amine-Functionalized Titanium Metal–Organic Framework Photocatalyst with Visible-Light-Induced Activity for CO2 Reduction. *Angewandte Chemie International Edition* **2012**, *51* (14), 3364-3367. DOI: https://doi.org/10.1002/anie.201108357.

(14) Thomas, B.; Morris, A. J. Chapter Five - Photoactive MOFs for CO2 activation utilizing earth abundant metals. In *Advances in Inorganic Chemistry*, van Eldik, R., Ford, P. C. Eds.; Vol. 83; Academic Press, 2024; pp 161-187.

(15) Xia, Q.; Li, Z.; Tan, C.; Liu, Y.; Gong, W.; Cui, Y. Multivariate Metal–Organic Frameworks as Multifunctional Heterogeneous Asymmetric Catalysts for Sequential Reactions. *Journal of the American Chemical Society* **2017**, *139* (24), 8259-8266. DOI: 10.1021/jacs.7b03113.

(16) Benseghir, Y.; Solé-Daura, A.; Cairnie, D. R.; Robinson, A. L.; Duguet, M.; Mialane, P.; Gairola, P.; Gomez-Mingot, M.; Fontecave, M.; Iovan, D.; et al. Unveiling the mechanism of the photocatalytic reduction of CO2 to formate promoted by porphyrinic Zr-based metal–organic frameworks. *Journal of Materials Chemistry A* **2022**, *10* (35), 18103-18115, 10.1039/D2TA04164B. DOI: 10.1039/D2TA04164B.

(17) Lin, S.; Ravari, A. K.; Zhu, J.; Usov, P. M.; Cai, M.; Ahrenholtz, S. R.; Pushkar, Y.; Morris, A. J. Insight into Metal–Organic Framework Reactivity: Chemical Water Oxidation Catalyzed by a [Ru(tpy)(dcbpy)(OH2)]2+-Modified UiO-67. *ChemSusChem* **2018**, *11* (2), 464-471. DOI: https://doi.org/10.1002/cssc.201701644.

(18) Yan, Z.-H.; Ma, B.; Li, S.-R.; Liu, J.; Chen, R.; Du, M.-H.; Jin, S.; Zhuang, G.-L.; Long, L.-S.; Kong, X.-J.; et al. Encapsulating a Ni(II) molecular catalyst in photoactive metal–organic framework for highly efficient photoreduction of CO2. *Science Bulletin* **2019**, *64* (14), 976-985. DOI: https://doi.org/10.1016/j.scib.2019.05.014.

(19) Ma, Y.; Du, J.; Fang, Y.; Wang, X. Encapsulation of Cobalt Oxide into Metal-Organic Frameworks for an Improved Photocatalytic CO2 Reduction. *ChemSusChem* **2021**, *14* (3), 946-951. DOI: https://doi.org/10.1002/cssc.202002656.

(20) Gao, W.-Y.; Ngo, H. T.; Niu, Z.; Zhang, W.; Pan, Y.; Yang, Z.; Bhethanabotla, V. R.; Joseph, B.; Aguila, B.; Ma, S. A Mixed-Metal Porphyrinic Framework Promoting Gas-Phase CO2 Photoreduction without Organic Sacrificial Agents. *ChemSusChem* **2020**, *13* (23), 6273-6277. DOI: https://doi.org/10.1002/cssc.202001610.

(21) Huang, J.-M.; Zhang, X.-D.; Huang, J.-Y.; Zheng, D.-S.; Xu, M.; Gu, Z.-Y. MOF-based materials for electrochemical reduction of carbon dioxide. *Coordination Chemistry Reviews* **2023**, *494*, 215333. DOI: https://doi.org/10.1016/j.ccr.2023.215333.

(22) Johnson, B. A.; Bhunia, A.; Ott, S. Electrocatalytic water oxidation by a molecular catalyst incorporated into a metal–organic framework thin film. *Dalton Transactions* **2017**, *46* (5), 1382-1388, 10.1039/C6DT03718F. DOI: 10.1039/C6DT03718F.

(23) Mukhopadhyay, S.; Basu, O.; Nasani, R.; Das, S. K. Evolution of metal organic frameworks as electrocatalysts for water oxidation. *Chemical Communications* **2020**, *56* (79), 11735-11748, 10.1039/D0CC03659E. DOI: 10.1039/D0CC03659E.

(24) Gibbons, B.; Cairnie, D. R.; Thomas, B.; Yang, X.; Ilic, S.; Morris, A. J. Photoelectrochemical water oxidation by a MOF/semiconductor composite. *Chemical Science* **2023**, *14* (18), 4672-4680, 10.1039/D2SC06361A. DOI: 10.1039/D2SC06361A.

(25) Lin, S.; Usov, P. M.; Morris, A. J. The role of redox hopping in metal–organic framework electrocatalysis. *Chemical Communications* **2018**, *54* (51), 6965-6974, 10.1039/C8CC01664J. DOI: 10.1039/C8CC01664J.

4. Electrochemical Reduction of CO_2 by a Cyclam-based Catalyst in a Metal Organic Framework

Ben Thomas, Amanda Morris

Abstract

The abundance of carbon dioxide (CO_2) released from the combustion of fossil fuels has plagued research groups for decades to find a way to scrub the atmosphere of the greenhouse gas and utilize the byproduct for chemical synthesis. Recent progress has focused on developing catalysts for selective electrochemical reduction of CO_2 to carbon monoxide and other C_1 products. Solid metal based catalysts provide high recyclability but lack methods to tune their structures. Homogenous molecular catalysts, on the other hand, are more easily tunable, yet their difficulty in separation from products makes them difficult to utilize. Metal-organic frameworks (MOFs) provide a method to employ the tunability of a molecular catalyst with the recyclability of a heterogeneous catalyst. Herein, we report the incorporation of a known electrocatalyst for CO_2 reduction into a MOF, VPI-100. The MOF was deposited onto a glassy carbon electrode and subjected to bulk electrolysis. Under a CO_2 atmosphere, carbon monoxide was detected as the major product of the MOF-coated film with a faradaic efficiency of 56%. The result shows MOFs as a promising scaffold for carbon dioxide reduction and an avenue to a clean energy future.

4.1 INTRODUCTION

The climate crisis has been an issue since the start of the Industrial Revolution. Nearly 4/5ths of our energy comes from fossil fuel combustion.[1] The use of fossil fuels has led to an increased CO_2 concentration in the atmosphere, which, due to greenhouse gas effects, is correlated with an increase in global temperature. While removal of these greenhouse gases from the atmosphere is vital to a sustainable future, the abundance of CO_2 generated can be used to create feedstock

chemicals for industrial processes like polymer production and synthetic fuels.[2] While the conversion of CO_2 to value-added chemicals has been done, the several different products that can be generated pose an issue with product collection.[3, 4] Table 1 shows the possible C1 reduction products of CO_2 and their relative standard reduction potentials as well as the standard reduction potential for hydrogen production.

Table 1: CO_2 reduction products and their standard reduction potentials

Reaction	E(V) vs. SCE
$CO_2 + e^- \longrightarrow CO_2^{\bullet -}$	-2.14
$CO_2 + 2H^+ + 2e^- \longrightarrow CO + H_2O$	-0.77
$CO_2 + 2H^+ + 2e^- \longrightarrow HCO_2H$	-0.85
$CO_2 + 6H^+ + 6e^- \longrightarrow CH_3OH + H_2O$	-0.62
$CO_2 + 8H^+ + 8e^- \longrightarrow CH_4 + 2H_2O$	-0.48
$2H^+ + 2e^- \longrightarrow H_2$	-0.24

Several catalysts have shown high activity for reducing CO_2 to these products. Copper metal has been shown to reduce CO_2 efficiently to over 30 different products [5] Monometallic catalysts are hard to understand mechanistically, and catalyst properties such as local pH, grain boundaries, and absorbed species can impact the mechanism and, therefore, product of the reduction.[6] The low valent, electron-rich nature of these metal surfaces favors the reduction of both protons and CO_2 in favorable conditions, making the selectivity of generating the desired product much harder. Homogenous molecular catalysts, on the other hand, are more easily tunable to generate the desired

product.[7] The molecular nature of organometallic catalysts gives a synthetic handle to understand the mechanism of CO_2.[7] These catalysts have shown high selectivity for CO, formic acid, and other desired CO_2 reduction products.[5] Metal cyclams have been shown to have high activity for the reduction of CO_2 to both CO and formic acid.[8] $[Ni^{2+}(cyclam)Cl]Cl_2$ (cyclam = 1,4,8,11-tetraazacyclotetradecane) complexes are well known to selectively reduce CO_2 to in aqueous solutions. The structure is a macrocycle with 4 pendant nitrogen atoms giving a binding site for the transition metal in the middle of the cycle. The pendant amine groups protonated with hydrogens provide ease of access to protons needed for the reduction of CO_2.[9] These complexes are much harder to recycle and can be difficult to separate from liquid products, leading to issues with industrial applications due to the high cost-to-product ratio.[10]

Newer studies have focused on immobilizing homogenous catalysts onto electrode surfaces.[11, 12] Metal-organic frameworks (MOFs) provide one platform for this immobilization. MOFs are highly crystalline materials comprised of organic polydentate linkers and inorganic metal-oxo clusters. This combination of nodes and linkers crystallizes into a highly porous, highly tunable microcrystal. MOFs have previously been used for various applications, including drug delivery[13], electrocatalysis[14, 15], gas adsorption[16], and photochemical applications.[17] The MOF structure provides multiple avenues for catalyst incorporation. First, the node can have open binding sites that can be used for the incorporation of single atoms or other catalysts for reactivity.[18] Second, the organic linker can be directly swapped for, or functionalized to contain an organometallic catalyst.[19, 20] The benefits of combining a molecular catalyst into a MOF allow for the selectivity

and tunability of the molecular complexes to be combined with the recyclability and separation of the solid metal catalysts.

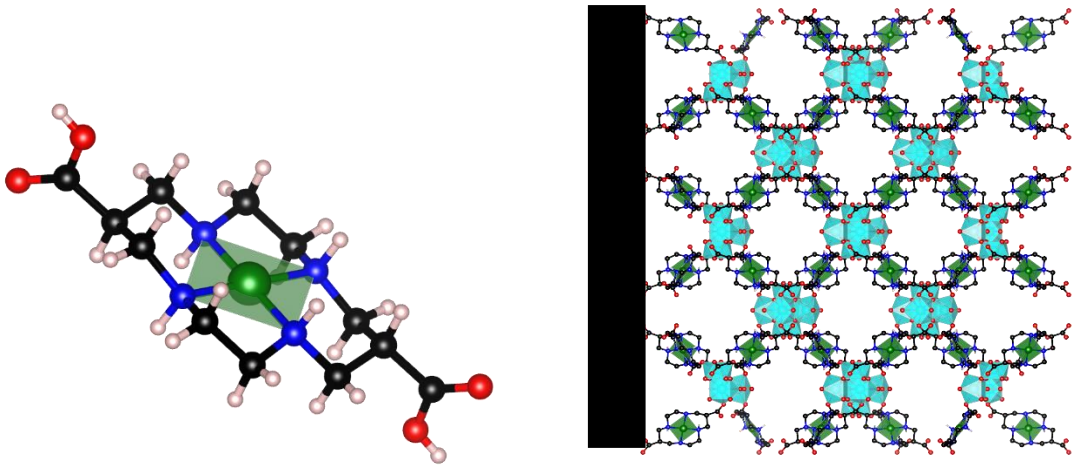

Figure 19: a) structure of Ni(cyclam) ligand, Ni-green, N-blue, C-black, H-white, O-Red. b) Structure of VPI-100 on glassy carbon, Zr-light blue

By incorporation of a known CO_2 reduction electrocatalyst into a MOF. The solid framework can be used several times over to reduce CO_2. Our group has previously incorporated metal cyclam complexes into a MOF, VPI-100.[21] Figure 1 shows the structure of the linker of VPI-100(Ni), Ni(cyclam), (6,13-dicarboxy-1,4,8,1l-tetraazacyclotetradecane)nickel(II) chloride as well as the crystal structure of VPI-100(Ni) grown on a glassy carbon electrode. The VPI-100 MOF has previously shown activity for CO_2 adsorption and activation with catalytic cycloaddition with epoxides. Herein, we report the growth of a thin film of VPI-100 (Ni) powder on a glassy carbon electrode using electrochemical deposition for the electrochemical reduction of CO_2 into carbon monoxide.

4.2 MATERIALS AND METHODS

Synthesis of 6,13-dicarboxy-1,4,8,11-tetraazacyclotetradecane

The synthesis of the cyclam ligand, 6,13-dicarboxy-1,4,8,11-tetraazacyclotetradecane was followed a literature procedure.[22] The copper metalated complex, (6,13-dicarboxy-1,4,8,1l-tetraazacyclotetradecane)copper(II) perchlorate, was refluxed in concentrated hydrochloric acid until the solution charged from purple to yellow. The white precipitate was collected, rinsed with cold water and ethanol and dried in a 120 °C oven. ^{1}H NMR, Figure 2, (deuterium oxide/NaOH, ppm): 2.05(m, 3H), 2.21(q, 2H), 2.28(d, 2H), 2.35(d, 2H).

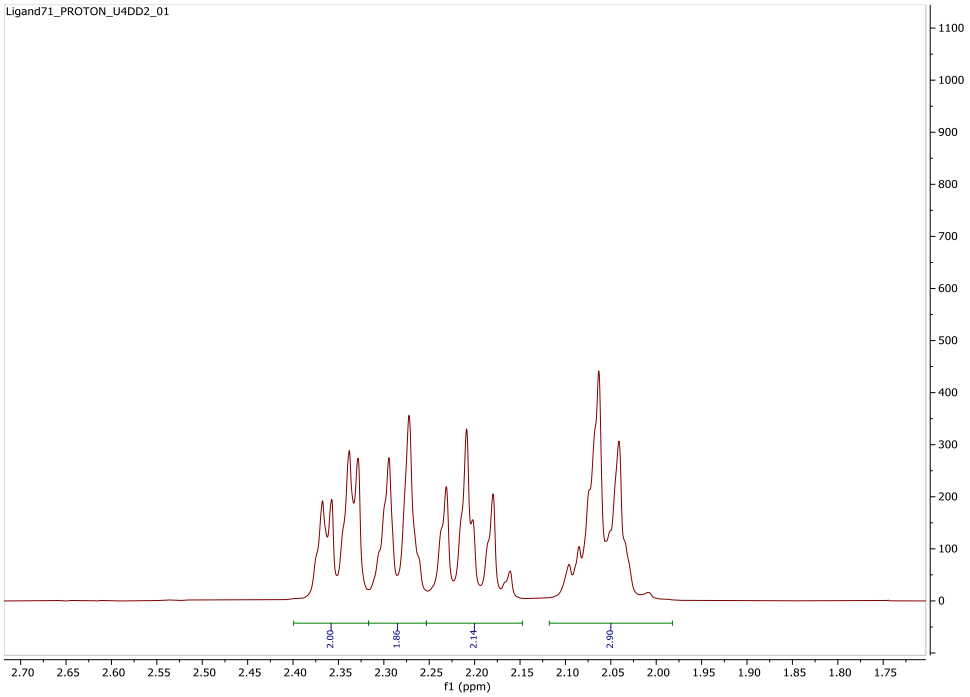

Figure 20: 1H 400 MHz NMR in D_2O of Cyclam ligand, 6,13-dicarboxy-1,4,8,11-tetraazacyclotetradecane

VPI-100(Ni) Synthesis

VPI-100(Ni) MOF was synthesized following a published procedure.[21] $ZrCl_4$ (14 mg) was added to a 2-dram scintillation vial with 2 mL of dry DMF and 0.44 mL. 6,13-dicarboxy-1,4,8,11-tetraazacyclotetradecane (17 mg) and $NiCl_2x6H_2O$ (14 mg) were combined in a separate 2-dram scintillation vial and dissolved in 2 mL of dry DMF. The vials were sonicated then placed in an 80 °C oven for one hour. The vials were removed from the oven and cooled to room temperature. The solutions were combined into one vial and placed in a 120 °C oven for 24 hours. The vial was

allowed to cool to room temperature. A pale pink powder was collected through centrifuge and washed with DMF and methanol. The powder was air dried, and the identity of the powder was confirmed using P-XRD.

PXRD Analysis

Powder X-ray Diffraction (PXRD) patterns were collected on a Rigaku Miniflex instrument (Cu Kα, λ= 1.5418 Å) from 2° to 30° with a resolution of 0.05° at a rate of 0.5° per minute.

Electrophoretic Deposition

Ten milligrams of VPI-100(Ni) were measured into a 6-dram scintillation vial with 10 mL of toluene. The vial was sonicated to suspend the MOF in the toluene. Two cleaned glassy carbon plates were connected to electrodes and placed in solution about 1 cm apart. An electric field was generated by applying 135 V for 6 hours. The films were removed from solution, rinsed with fresh toluene and a pale white film appeared on both electrodes. The electrodes were placed in 120 °C oven to dry.

Electrochemical Methods

The cyclic voltammetry and the electrolysis of the MOF film was done in a three-electrode set up using a Pine Wavenow instrument. The MOF-deposited film was used as the working electrode. An Ag/Ag^+ non-aqueous reference electrode was used as well as platinum mesh as the counter electrode. The cell was sealed using rubber septa and purged with either Ar or CO_2 for at least two hours before data collection. During bulk electrolysis, the headspace was circled in a gas loop using a micropump connected to an injection port in the Agilent GC system. During headspace analysis the column, (Agilent Technologies 7890A GC System using an Agilent J&W GC Columns Select Permanent Gases/CO2 Molsieve S3 5A/Porabond Q Tandem column) was heated from 50 °C to 220 °C at a ramp rate of 15 °C/min then held at 220 °C for 8 minutes.

4.3 RESULTS AND DISCUSSION

The MOF powder was successfully grown following the literature procedure as shown in Figure 3a with the experimental PXRD pattern matching closely with the simulated pattern. The MOF film was then grown onto a glassy carbon electrode with electrophoretic deposition. The SEM images show the quasi-spherical particles that have been shown with VPI-100 in previous reports indicating a successful deposition of the MOF film onto the electrode.

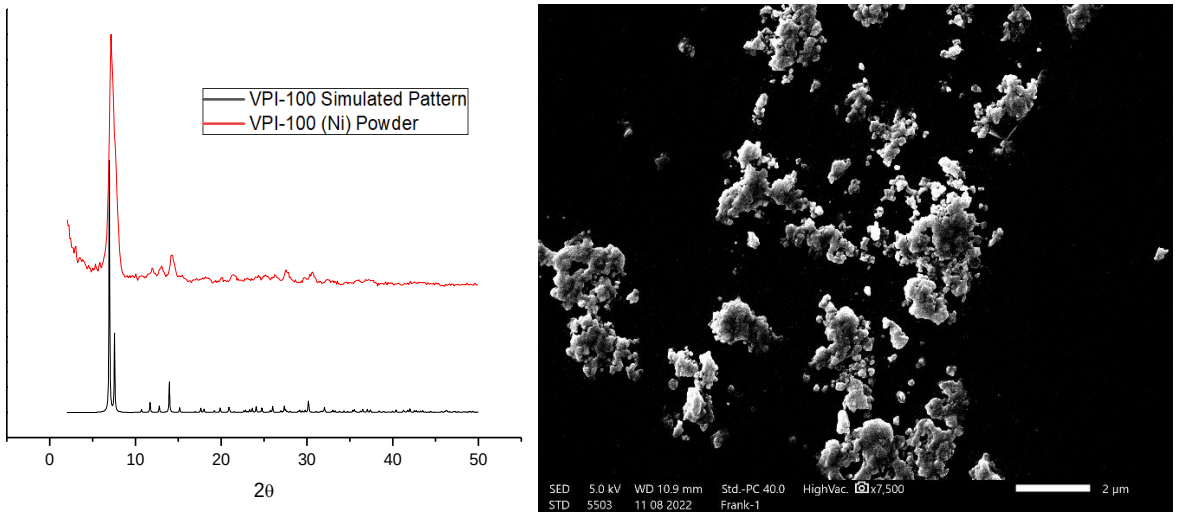

Figure 21: a) simulated pattern for VPI-100 and synthesized VPI-100(Ni) powder b) SEM imagine of electrophoretically deposited VPI-100(Ni) on glassy carbon.

Cyclic voltammetry studies were done on the MOF film shown in Figure 4 in 0.1 M $TBAPF_6$ $MeCN/H_2O$ 4:1 in an Argon atmosphere shows large resistive current with catalytic current taking off around -1.6 V vs NHE for the hydrogen evolution reaction. When the cell was saturated with CO_2, the catalytic current takes off much earlier, around -1.1 V vs. NHE which indicates the CO_2 is being reduced at a lower potential than protons. An oxidative peak appears near -0.3 V vs NHE which only appears after the introduction of CO_2 and scan to negative potentials. This peak could be attributed to the release of a reductive product from the framework.

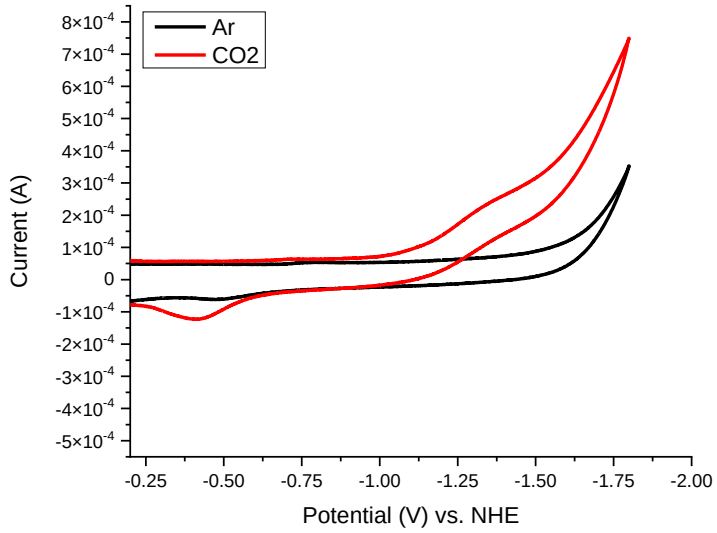

Figure 22: Cyclic voltammetry of VPI-100(Ni) MOF film done in 0.1 $TBAPF_6$ MeCN/H_2O 4:1 under Ar (black) and CO_2(Red)

The MOF was electrochemically active showing the production of CO from CO_2 when a potential of -1.5 V was applied to the VPI-100 (Ni) coated electrode in 0.1 M $TBAPF_6$ MeCN/H_2O 4:1 for 2 hours. After electrolysis, GC chromatograms were taken to evaluate the gaseous products. NMR of the solution was taken to evaluate the liquid products and stability of the catalyst. No liquid products were detected, and the MOF seemed to be stable to electrolysis due to the absence of ligand peaks in the NMR spectrum.

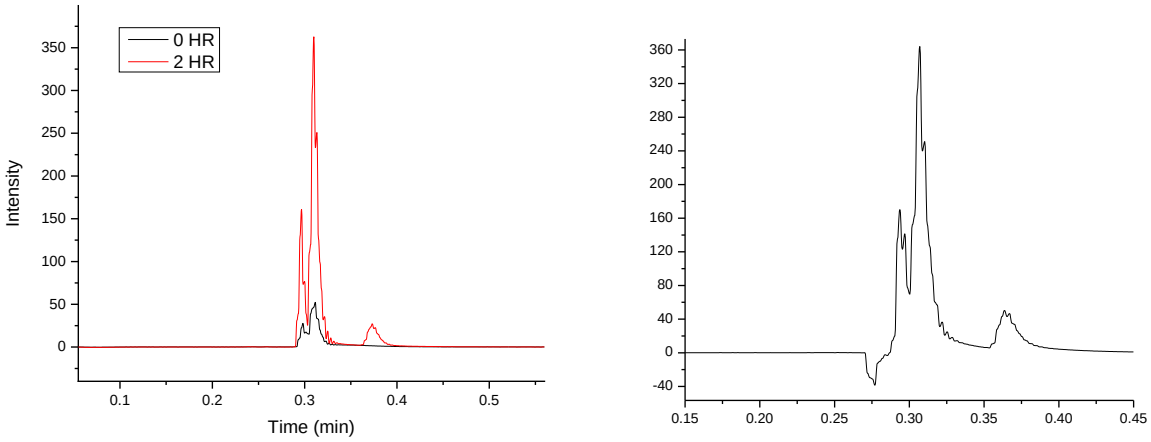

Figure 23:Chromatograms from CO_2 reduction bulk electrolysis a) at 0 h (black) and 2 h (red) b) 16 h

Figure 5 shows the GC results of the electrolysis after 2 hours of electrolysis. The two peaks near 0.30 min are oxygen and nitrogen. The micropump used is pressurized with compressed air so the peaks will be present upon injection. The peak at 0.37 min is carbon monoxide. Using a calibration curve of different amounts of CO injected into the GC, the amount of CO produced is about 1000 µL which translates to a faradaic efficiency of 56%.[23] Some of the missing current density can be attributed to resistance across the MOF film. Upon oxidation for 16 hours a negative peak appears in the chromatogram. The negative peak at 0.27 minutes is hydrogen gas. The peak is negative because the thermal conductivity of hydrogen is higher than that of helium resulting in the detector recognizing a lower thermal conductivity when the hydrogen passes through therefore producing a negative peak. Due to similarities in thermal conductivity between the carrier gas, helium, and hydrogen, the sensitivity for hydrogen is low and thus does not appear until a much higher concentration is reached.

4.4 CONCLUSION

In this report, the MOF VPI-100(Ni) was synthesized, and a thin film was electrochemically deposited onto a glassy carbon electrode. The MOF-coated electrode was subjected to electrolysis

under a CO_2 atmosphere, and CO was seen as the major product with a faradaic efficiency of 56%. The result shows that cyclam retains its catalytic activity even when incorporated into the framework. More work can be done to investigate ways to tune the reactivity to increase efficiency and selectivity for CO as a singular product of the reduction.

4.5 REFERENCES

(1) Administration, U. S. E. I. *Electricity Explained*. 2023. https://www.eia.gov/energyexplained/electricity/electricity-in-the-us.php (accessed 2023 07/03).

(2) Zhang, L.; Wang, Y. Decoupled Artificial Photosynthesis. *Angewandte Chemie International Edition* **2023**, *62* (23), e202219076. DOI: https://doi.org/10.1002/anie.202219076.

(3) Song, J. T.; Song, H.; Kim, B.; Oh, J. Towards Higher Rate Electrochemical CO2 Conversion: From Liquid-Phase to Gas-Phase Systems. *Catalysts* **2019**, *9* (3), 224.

(4) Zhang, S.; Fan, Q.; Xia, R.; Meyer, T. J. CO2 Reduction: From Homogeneous to Heterogeneous Electrocatalysis. *Accounts of Chemical Research* **2020**, *53* (1), 255-264. DOI: 10.1021/acs.accounts.9b00496.

(5) Kuhl, K. P.; Cave, E. R.; Abram, D. N.; Jaramillo, T. F. New insights into the electrochemical reduction of carbon dioxide on metallic copper surfaces. *Energy & Environmental Science* **2012**, *5* (5), 7050-7059, 10.1039/C2EE21234J. DOI: 10.1039/C2EE21234J.

(6) Raciti, D.; Wang, C. Recent Advances in CO2 Reduction Electrocatalysis on Copper. *ACS Energy Letters* **2018**, *3* (7), 1545-1556. DOI: 10.1021/acsenergylett.8b00553.

(7) Zhang, H.; Liang, Q.; Xie, K. How to rationally design homogeneous catalysts for efficient CO2 electroreduction? *iScience* **2024**, *27* (2), 108973. DOI: https://doi.org/10.1016/j.isci.2024.108973.

(8) Froehlich, J. D.; Kubiak, C. P. Homogeneous CO2 Reduction by Ni(cyclam) at a Glassy Carbon Electrode. *Inorganic Chemistry* **2012**, *51* (7), 3932-3934. DOI: 10.1021/ic3001619.

(9) Froehlich, J. D.; Kubiak, C. P. The Homogeneous Reduction of CO2 by [Ni(cyclam)]+: Increased Catalytic Rates with the Addition of a CO Scavenger. *Journal of the American Chemical Society* **2015**, *137* (10), 3565-3573. DOI: 10.1021/ja512575v.

(10) Feng, D.-M.; Zhu, Y.-P.; Chen, P.; Ma, T.-Y. Recent Advances in Transition-Metal-Mediated Electrocatalytic CO2 Reduction: From Homogeneous to Heterogeneous Systems. *Catalysts* **2017**, *7* (12), 373.

(11) Maurin, A.; Robert, M. Noncovalent Immobilization of a Molecular Iron-Based Electrocatalyst on Carbon Electrodes for Selective, Efficient CO2-to-CO Conversion in Water. *Journal of the American Chemical Society* **2016**, *138* (8), 2492-2495. DOI: 10.1021/jacs.5b12652.

(12) Bullock, R. M.; Das, A. K.; Appel, A. M. Surface Immobilization of Molecular Electrocatalysts for Energy Conversion. *Chemistry – A European Journal* **2017**, *23* (32), 7626-7641. DOI: https://doi.org/10.1002/chem.201605066.

(13) Cornell, H. D.; Zhu, Y.; Ilic, S.; Lidman, N. E.; Yang, X.; Matson, J. B.; Morris, A. J. Green-light-responsive metal–organic frameworks for colorectal cancer treatment. *Chemical*

Communications **2022**, *58* (34), 5225-5228, 10.1039/D2CC00591C. DOI: 10.1039/D2CC00591C.

(14) Lin, S.; Usov, P. M.; Morris, A. J. The role of redox hopping in metal–organic framework electrocatalysis. *Chemical Communications* **2018**, *54* (51), 6965-6974, 10.1039/C8CC01664J. DOI: 10.1039/C8CC01664J.

(15) Bavykina, A.; Kolobov, N.; Khan, I. S.; Bau, J. A.; Ramirez, A.; Gascon, J. Metal–Organic Frameworks in Heterogeneous Catalysis: Recent Progress, New Trends, and Future Perspectives. *Chemical Reviews* **2020**, *120* (16), 8468-8535. DOI: 10.1021/acs.chemrev.9b00685.

(16) Li, H.; Wang, K.; Sun, Y.; Lollar, C. T.; Li, J.; Zhou, H.-C. Recent advances in gas storage and separation using metal–organic frameworks. *Materials Today* **2018**, *21* (2), 108-121. DOI: https://doi.org/10.1016/j.mattod.2017.07.006.

(17) Thomas, B.; Morris, A. J. Chapter Five - Photoactive MOFs for CO2 activation utilizing earth abundant metals. In *Advances in Inorganic Chemistry*, van Eldik, R., Ford, P. C. Eds.; Vol. 83; Academic Press, 2024; pp 161-187.

(18) Johnson, E. M.; Boyanich, M. C.; Gibbons, B.; Sapienza, N. S.; Yang, X.; Karim, A. M.; Morris, J. R.; Troya, D.; Morris, A. J. Aqueous-Phase Destruction of Nerve-Agent Simulants at Copper Single Atoms in UiO-66. *Inorganic Chemistry* **2022**, *61* (22), 8585-8591. DOI: 10.1021/acs.inorgchem.2c01351.

(19) Lin, S.; Pineda-Galvan, Y.; Maza, W. A.; Epley, C. C.; Zhu, J.; Kessinger, M. C.; Pushkar, Y.; Morris, A. J. Electrochemical Water Oxidation by a Catalyst-Modified Metal–Organic

Framework Thin Film. *ChemSusChem* **2017**, *10* (3), 514-522. DOI: https://doi.org/10.1002/cssc.201601181.

(20) Ahrenholtz, S. R.; Epley, C. C.; Morris, A. J. Solvothermal Preparation of an Electrocatalytic Metalloporphyrin MOF Thin Film and its Redox Hopping Charge-Transfer Mechanism. *Journal of the American Chemical Society* **2014**, *136* (6), 2464-2472. DOI: 10.1021/ja410684q.

(21) Zhu, J.; Usov, P. M.; Xu, W.; Celis-Salazar, P. J.; Lin, S.; Kessinger, M. C.; Landaverde-Alvarado, C.; Cai, M.; May, A. M.; Slebodnick, C.; et al. A New Class of Metal-Cyclam-Based Zirconium Metal–Organic Frameworks for CO2 Adsorption and Chemical Fixation. *Journal of the American Chemical Society* **2018**, *140* (3), 993-1003. DOI: 10.1021/jacs.7b10643.

(22) Xin, L.; Curtis, N. F.; Weatherburn, D. C. Compounds of copper(II) and nickel(II) with 6,6,13,13-tetracarboxy-(andE-6,13-dicarboxy-) substituted 1,4,8,11-tetrazacyclotetradecanes, and carbomethoxy- and carbethoxy- derivatives. Structures of two isomericE-6,13-dicarboxy- (and anE-6,13-dicarbomethoxy-)1,4,8,11-tetrazacyclotetradecane copper(II) perchlorates. *Transition Metal Chemistry* **1992**, *17* (2), 147-154. DOI: 10.1007/BF02910808.

(23) Dutta, N.; Bagchi, D.; Chawla, G.; Peter, S. C. A Guideline to Determine Faradaic Efficiency in Electrochemical CO2 Reduction. *ACS Energy Letters* **2024**, *9* (1), 323-328. DOI: 10.1021/acsenergylett.3c02362.

Photoactive MOFs for CO_2 Activation Utilizing Earth Abundant Metals

Benjamin Thomas and Amanda J. Morris*
Department of Chemistry, Virginia Tech – College of Science, Blacksburg, VA 24061
Corresponding author: e-mail address- ajmorris@vt.edu

Contents

ABSTRACT

The production of carbon dioxide from the continued burning of fossil fuels has stressed our global climate and led to drastic environmental impacts. Methods to convert CO_2 captured at the point of combustion or collected from the atmosphere have emerged as a promising solution to the continued use of fossil fuels. One potential solution is to use the energy of the sun to promote the photoreduction of CO_2 into useful chemicals, e.g., fuels or feedstocks. To this end, both heterogeneous and homogeneous light absorbers and coupled catalysis have been extensively explored. Many of these processes and systems utilize noble and rare-earth metals, which limits the commercial applicability and sustainability of such solutions. The exploration of earth abundant metals in photocatalysis is of growing interest, but the stability of earth-abundant molecular catalysts and the lack of tunability with solid state approaches has hampered progress. Metal-organic frameworks (MOFs) are a class of materials that combine metal clusters and organic linkers into permanently porous materials. MOFs have shown immense promise in catalysis due to their synthetic tunability, facile incorporation of molecular photosensitizers and catalysts, and increased stability (compared to molecular analogs). Earth abundant metals can be used to prepare catalytically active scaffolds by incorporation into the nodes, alteration of organic linkers to

contain transition metal complexes, guest introduction into the pores, or creation of composite materials. Herein, we discuss the prominent examples of earth abundant metal containing MOFs for the reduction of CO_2.

5.1 Introduction

Carbon dioxide emissions from the use of fossil fuels and the resulting environmental impacts are arguably the most pressing scientific challenge that faces our generation. About 80% of the energy we produce comes from fossil fuel combustion and while alternative energy sources are emerging, the continued use of fossil fuels is projected for the foreseeable future.[1] Current efforts in the removal of CO_2 from the point sources and the atmosphere are focused on geological storage.[2] However, the utilization of CO_2 in the production of value-added chemicals, e.g., recycled fuels or chemical feedstocks, provides an additional economic advantage and a pathway to carbon neutrality.

The energy from the sun is a vastly untapped resource that can be used in creating a sustainable energy future. Solar panels are being installed at higher and higher rates due to increased energy costs and policies that incentivize cleaner energy sources.[3] The Department of Energy has launched a program in 2011 known as the Sunshot Initiative to further the use of solar power in the U.S. electricity supply.[4] The Sunshot Initiative, focused on scientific and engineering advances to lower the price of solar energy, caused the solar capacity in the energy grid to increase from less than 0.1% to 1%. In just 6 years since the initiative launched, the per kilowatt-hour price of solar power had dropped across all sectors by an average of 75%. As a result, solar energy capacity is projected to surpass natural gas and be the leading energy source by 2027.

While direct solar-to-electrical conversion has promise, energy storage remains a challenge. The intermittent nature of the sun requires energy to be stored for use when direct solar energy is not available. Methods to store solar energy include batteries and artificial photosynthesis. In the latter, energy from the sun can directly (or indirectly using electrolysis) form chemical products through the oxidation of water and reduction of CO_2. Both molecular photosensitizers and catalysts as well as solid-state semiconductors and nanoparticulate catalysts have been used in artificial photosynthetic schemes. We restrict our introductory discussion to molecular approaches. In a reductive process (relevant to our challenge of CO_2 reduction), a photosensitizer absorbs a photon of light, and an electron is promoted from the highest occupied molecular orbital (HOMO) of the sensitizer to a higher energy molecular orbital, creating an excited state. The electron vacancy, called a hole, generated in the HOMO is filled by a sacrificial electron donor while the excited electron is transferred to an active catalyst competent in reductive chemistry. While this is the ideal pathway several non-productive pathways are possible. For example, the excited electron and hole can recombine before interaction with the sacrificial electron donor. The excited state could also interact with other species present to produce unwanted products, e.g., proton or oxygen reduction. Therefore, much effort has been made to study the rates of photoinduced processes in such systems, in addition to developing selective catalysts.

CO_2 is an incredibly stable linear molecule, where the carbon exists in its most oxidized state. Thus, for the conversion of CO_2 to value-added products, the reduction is necessary. CO_2 has been reduced to numerous products ranging from carbon monoxide to hydroxyacetone.[5] That said, the most common products observed contain a single carbon center, including CO, formic acid (HCOOH), methanol (CH_3OH), and methane (CH_4). The number of protons and electrons transferred in each reaction are shown in the following Equations.

CO_2 Half Reaction	Electrochemical Potential (vs. SHE)	
$CO_2 + 2H^+ + 2e^- \rightarrow H_2O + CO$	-0.53	Equation 1
$CO_2 + 2H^+ + 2e^- \rightarrow HCOOH$	-0.61	Equation 2
$CO_2 + 6H^+ + 6e^- \rightarrow H_2O + CH_3OH$	-0.38	Equation 3
$CO_2 + 8H^+ + 8e^- \rightarrow 2H_2O + CH_4$	-0.24	Equation 4

Converting all the global CO_2 into one product would flood the market and render the chemicals' production economically worthless. Therefore, the development of viable pathways to several of these value-added products is key to keeping CO_2 reduction an economically profitable process.[6]

Given the high activation barriers to the reduction of CO_2, new catalysts that can selectively produce a desired product with minimal energy input are needed. Most commercial catalysts are heterogeneous metals and metal oxides because of their high stability in reaction conditions and ease of separation from liquid or gaseous products.[7] However, these catalysts often result in a mixture of products due to the non-specific nature of heterogeneous surfaces. For example, metallic copper, one of the most well-studied CO_2 reduction catalysts, forms no less than 16 different products.[5] For this reason, molecular CO_2 reduction catalysts have also received attention. Through synthetic manipulation and thus, control over reaction mechanism, selectivity for one CO_2 reduction product has been achieved. That said, homogeneous complexes are prone to deactivation and dimerization. The low stability renders these complexes less feasible for large scale, industrial applications. The combination of the tunability in homogenous complexes with the stability and recyclability of heterogenous complexes is crucial for future catalyst engineering.

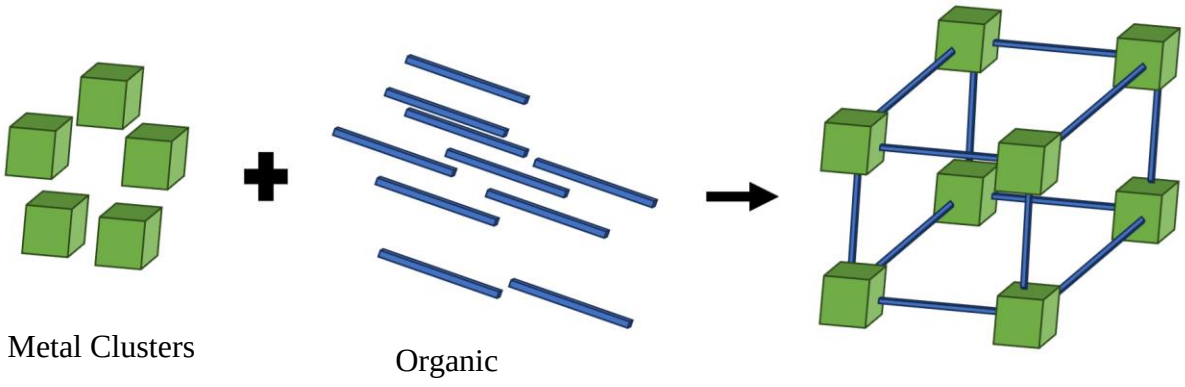

Figure 24: MOF synthesis scheme

Metal-organic frameworks (MOFs) provide a unique platform to combine the synthetic tunability of molecules and the stability of heterogeneous approaches. MOFs are a class of materials typically consisting of metal-oxo nodes connected by multidentate organic linkers to create 3-D porous scaffolds. MOFs feature permanent porosity, high surface area, and synthetic tunability.[8] Because of the vast array of building blocks available, the metal nodes and linkers used to assemble the MOFs can be judiciously chosen and synthetically manipulated for the desired application. MOFs have been functionalized with chromophores and/or catalysts for several applications including those relevant to artificial photosynthesis – water oxidation and CO_2 conversion.[9-11] The porosity and resulting accessible surface area of MOFs provide an additional advantage in catalysis – namely, all catalytic centers incorporated are theoretically accessible and active. Thus, MOFs have the potential for unmatched turnover numbers and frequencies on a per atom basis.[12]

There are several ways MOFs can be functionalized to create active materials for photochemical CO_2 activation. The metal node itself can be an active site for catalysis. Many MOFs are composed of metal-oxo clusters with open coordination sites capped by modulators, defined as monocarboxylic acids added to the synthesis to control crystallization, or solvent. These capping agents may be removed to provide an active site for CO_2 binding and activation. The open coordination sites on the nodes can also be post-synthetically modified with other transition metal

catalysts.[11] Alternatively, the linker can be itself a transition metal catalyst or post-synthetically modified to introduce a metal catalyst.[13] Indeed, MOFs using traditional homogeneous catalysts as linkers have been well established including porphyrins and other macrocyclic light absorbers.[14-16]

5.1.1Benchmarking

Numerous MOF platforms have been explored for the photoreduction of CO_2. Herein, they are divided into the following approaches - (1) Node-based Catalysts, (2) Linker-based Catalysts, (3) Pore Guest Catalysts, (4) MOF Composites. To compare the efficiency of these catalysts in an effective manner a few parameters are defined below followed by a comprehensive, to our knowledge, collection of these parameters for earth-abundant MOF-based approaches.

Turnover Number (TON). Turnover number is a critical parameter used to identify a true catalytic approach. Specifically, a true catalyst must exhibit a turnover number greater than one. Simply, turnover number is the ratio of the moles of product to the moles of active site, Eq. 1.

$$TON = \frac{moles\ of\ product\ produced}{moles\ of\ catalyst} \qquad \text{Eq. 5}$$

However, we caution the reader in direct comparisons of TONs. TONs, to be appropriately defined, should be measured at the point of catalyst deactivation. That said, many TONs are reported instead for a period of time. Thus, comparison between different catalysts over different periods is meaningless. MOFs provide a unique challenge in that MOF unit cells can include multiple metal centers. Turnover numbers should be reported per metal center or active site to properly report efficiencies of the catalyst, which means the active site should be well defined when catalytic activity is reported.

Turnover Frequency (TOF). To further define efficiency, the rate of catalysis is calculated as a TOF, which is simply the TON divided by the reaction time, Eq. 2.

$$TOF = \frac{TON}{time} \quad \text{Eq. 6}$$

While TOF is a figure of merit, researchers should also consider reporting initial rates. It is common to observe a decrease in the rate of catalysis over the course of the reaction. Given that the TOF is defined over the entire reaction period, the true rate of the catalysts may be masked by other effects, i.e., catalyst deactivation and/or substrate/product diffusion. Therefore, the initial rate, defined as the initial linear portion of a product vs. time plot can provide a more accurate assessment of the true rate of the catalytic platform.

Selectivity. CO_2 can be reduced into several hydrogenated products including carbon monoxide, formic acid, methanol, methane, and even C_2+ products such as ethane, ethanol, and more (*vide supra*). In addition to carbon-containing products, most CO_2 reduction catalysts are also active for proton reduction to produce hydrogen gas. Because of the several different products of CO_2 conversion reactions, the production of a target product compared to other products produced by the catalyst is defined as selectivity. The equation for selectivity is:

$$\text{Selectivity} = \frac{moles\ desired\ product}{moles\ total\ products} \quad \text{Eq. 7}$$

5.2 Node Based Catalysts

Table 1: Summary of Earth-Abundant MOF-based Approaches for CO_2 Reduction with Node based active sites.

MOF	Light Absorber	Active Site	e^- donor	Light Source (nm)	Product	µmol/g	Time	Ref.
MIL-125(Ti)	BDC	Ti Node	TEOA[c]	420-800	$HCOO^-$	-	10 h	[17]
NH_2-MIL-125(Ti)	NH_2-BDC	Ti Node	TEOA	420-800	$HCOO^-$	162.8	10 h	[17]
MIL-101	BDC	Fe node	TEOA	420-800	$HCOO^-$	1180	8 h	[18]
MIL-53	BDC	Fe node	TEOA	420-800	$HCOO^-$	594	8 h	[18]

MIL-88	BDC	Fe node	TEOA	420-800	$HCOO^-$	180	8 h	[18]
NH_2-MIL-101	NH_2-BDC	Fe node	TEOA	420-800	$HCOO^-$	3560	8 h	[18]
NH_2-MIL-53	NH_2-BDC	Fe node	TEOA	420-800	$HCOO^-$	930	8 h	[18]
NH_2-MIL-88	NH_2-BDC	Fe node	TEOA	420-800	$HCOO^-$	600	8 h	[18]
MOF-545	TCPP[b]	Zr node	TEOA	>415	$HCOO^-$	636	4 h	[13]
MOF-545(Cu)	TCPP	Zr node	TEOA	>415	$HCOO^-$	668	4 h	[13]
MOF-545(Co)	TCPP	Zr node	TEOA	>415	$HCOO^-$	900	4 h	[13]
MOF-545(Mn)	TCPP	Zr node	TEOA	>415	$HCOO^-$	1528	4 h	[13]
MOF-545(Zn)	TCPP	Zr node	TEOA	>415	$HCOO^-$	1668	4 h	[13]
MOF-545(Fe)	TCPP	Zr node	TEOA	>415	$HCOO^-$	2264	4 h	[13]
NanoMOF-545	TCPP	Zr node	TEOA	>415	$HCOO^-$	1600	4 h	[13]
NanoMOF-545(Fe)	TCPP	Zr node	TEOA	>415	$HCOO^-$	4640	4 h	[13]
MAF-X27*l*-Cl	$Ru(bpy)_3$	Co node	TEOA	420	$HCOO^-$	24685	1 h	[19]
MAF-X27*l*-OH	$Ru(bpy)_3$	Co node	TEOA	420	$HCOO^-$	121371	1 h	[19]
Co-ZIF-9	$Ru(bpy)_3$	Co node	TEOA	>420	$HCOO^-$	36000	1 h	[20]
UiO-67-0[a]	BDC	Zr node	H_2O	White light (Xe lamp)	CO	28	12 h	[21]
UiO-67-100[a]	BDC	Zr node	H_2O	White light (Xe lamp)	CO	110	12 h	[21]
UiO-67-200[a]	BDC	Zr node	H_2O	White light (Xe lamp)	CO	148	12 h	[21]
UiO-67-300[a]	BDC	Zr node	H_2O	White light (Xe lamp)	CO	76	12 h	[21]
In-Fe TCPP MOF	TCPP	Fe TCPP	L-AP[d]	>400	$HCOO^-$	3469	24 h	[22]
Ti/Zr-MOF-525	TCPP	Ti/Zr cluster	H_2O	>400	CH_4 CO	2.14 0.79	6 h	[23]

[a]amount of formic acid added to reaction to induce defects
[b]TCPP- Tetrakis(4-carboxyphenyl)porphyrin
[c]TEOA- triethanolamine
[d]L-AP-$_L$-ascorbgyl palmitate

The most widely studied class of MOF CO_2 reduction platforms involves catalytic nodes that are activated through direct excitation or charge transfer chemistry with the organic linkers. To be active, the MOF should contain an open coordination site on the node for CO_2 binding and activation. Many MOFs feature sites that can be accessible in this regard. Typically, these sites are

capped by mono-carboxylic acids (termed modulator in MOF synthesis), solvent, or an anion, e.g., chloride. If these species are removed, by either activation (heating typically under vacuum) or simple equilibrium-drive exchange, then the node can act as a catalyst for CO_2 reduction.

One common approach prevalent with MOF catalysis is to couple light absorption by a proximal linker with catalytic activity at the metal node.

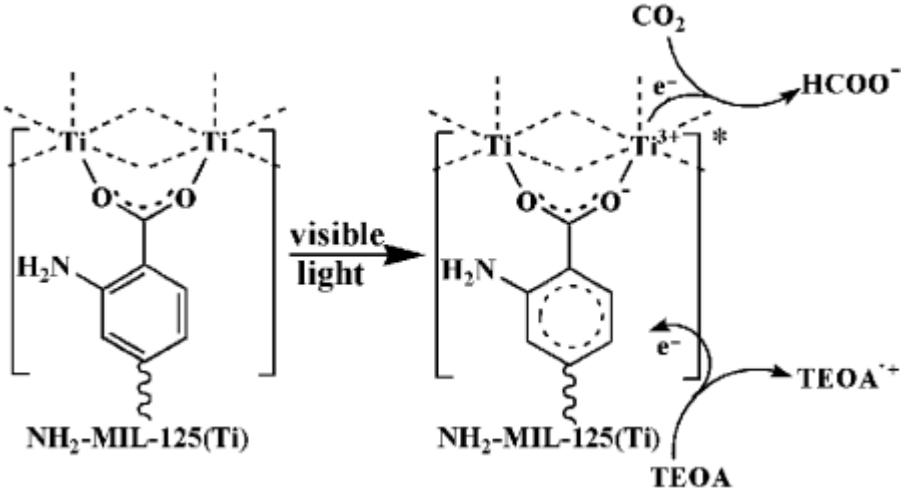

*Figure 25: Proposed mechanism of CO_2 conversion in NH_2-MIL-125(Ti). . Reprinted with permission from Angewandte Chemie International Edition **2012**, 51 (14), 3364-3367., Copyright 2012, Wiley Materials.*[17]

The quintessential example for such an approach in MOF-based photochemical CO_2 reactivity is titanium-based NH_2-MIL-125(Ti), Figure 2[17]. The linker, BDC-NH_2 is photoexcited in the visible range of the electromagnetic spectrum. The excited state of the linker donates an electron to the titanium node forming a charge separated state. The charge separated state takes the form of NH_2-$BDC^{\bullet+}$-Ti^{III}. The generation of the Ti^{III} species was demonstrated with electron paramagnetic resonance. For completion of the catalytic cycle, the oxidized linker is regenerated by triethanolamine (TEOA), a sacrificial electron donor (SED). The use of the organic linker as the photosensitizer allows for modification of spectral response. For example, the modification of the native BDC linker in MIL-125(Ti) with an $–NH_2$ moiety enables absorption of light to extend into the yellow. Crystal engineering has also been used to improve reactivity. The morphology of the MIL-125 crystal has two facets implicated in CO_2 activation, {001} and {111}. By altering

synthesis conditions, the different facets of this crystal can be exposed.[24] Through synthetic manipulation of the exposed facets, it was determined that the {111} facet enables a 10-fold increase in reactivity over the crystals with only exposed {001} which is attributed to increased CO_2 adsorption and increased lifetime of the excited state.

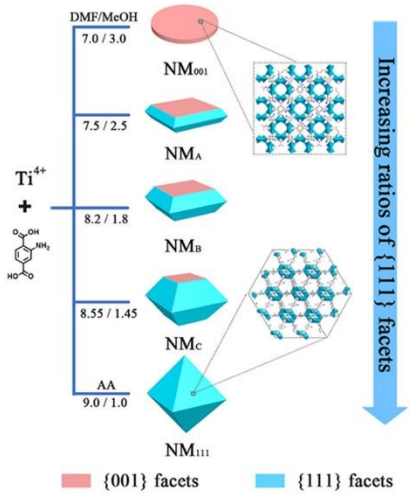

Figure 26: Design of different shaped MIL-125 crystals. Reprinted with permission from ACS Catalysis 2021, 11 (2), 650-658. Copyright 2021 American Chemical Society.[24]

Iron-based MOFs have been reported as an efficient photochemical CO_2 conversion catalyst into formate at different rates based on reaction conditions and 3D structure.[18, 25] Like MIL-125(Ti), light absorption by the organic linker is implicated in the formation of a charge separated state with reduction of iron(III) to iron (II). Linker modification analogous to MIL-125(Ti) and NH_2-MIL-125(Ti), i.e., MIL-101, MIL-88, MIL-53, demonstrated that the addition of an amine group to the organic linker contributed to increased light absorption and thus, reactivity. The class of iron-based MOFs enabled the systematic study of 3D structure and node composition on observed reactivity.[18] MIL-101, MIL-53, and MIL-88 all contain benzene dicarboxylic acid as the organic linker but have different node structures and morphologies, Figure 4. The critical feature of the MOFs that determined reaction rate was the open coordination site content and the ability for the CO_2 to adsorb to those sites. Indeed, MIL-101 was the most active as it features three open

coordination sites in comparison to MIL-53 which only contained open coordination sites on the ends of the FeO cluster chains. While MIL-101 contained coordinated 4 hydroxide groups per node, the ability for CO_2 to bind to the iron centers was not seen in IR measurements under CO_2

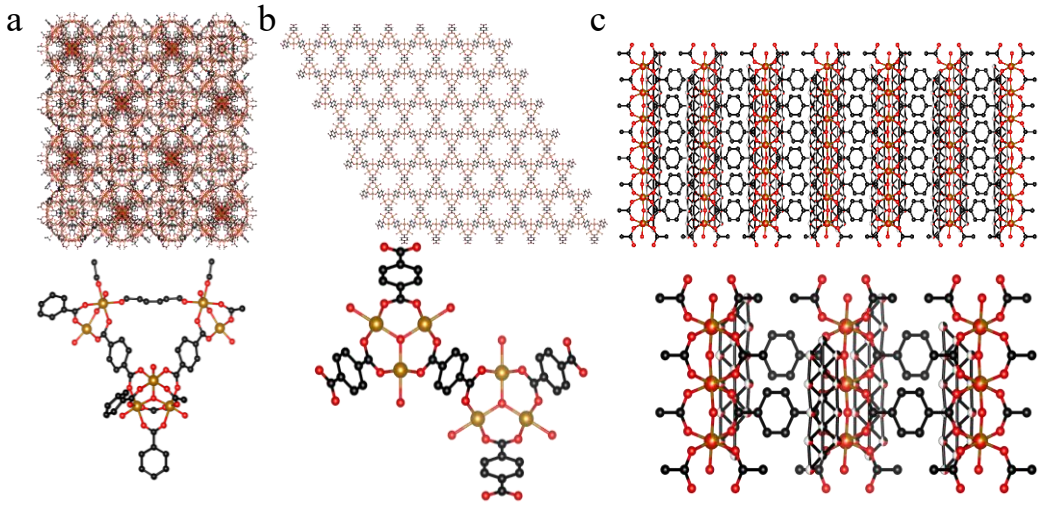

Figure 27: Crystal structure and zoomed in node structures of a) MIL-101, b) MIL-88, and c) MIL-53

atmosphere. The lack of binding to the node leads to a lower CO_2 adsorption capacity, 10.4 cm^3/g compared to 26.4 cm^3/g in MIL-101, which explains the reduced reactivity.

The importance of mechanistic investigations cannot be understated. By exploring the pathway of CO_2 conversion, active sites can be synthetically tuned to promote activity or selectivity toward a certain product. A recent investigation of the mechanism of photochemical reduction by a porphyrin-based MOF series based on MOF-545-M (where M = Cu, Co, Mn, Zn, Fe, and free base) offered critical insight into the observed formation of formate.[13] Porphyrins are well known macrocyclic photoactive molecules that have shown to photo catalyze the CO_2 reduction reaction in homogeneous solution. Hence, the linker has gained significant popularity in photochemical MOF CO_2 reduction reactivity.[13, 22, 23, 26, 27] MOF-545-M contains tetracarboxyphenylporphyrin linkers and Zr^{IV} nodes. Transient absorption spectroscopy was used to probe the existence of a putative charge separated state ($Por^{\bullet+}$-Zr^{III}) within the MOF. No evidence for such a photo-induced charge separated state was found. Additionally, while the SED was competent in reduction of

porphyrin contained metals (e.g., Fe^{III} to Fe^{II}), the catalytic state of these species (e.g., Fe^{0}) was not reached under bulk photolysis conditions. Further studies pointed to another critical function of the SED. A mechanism in which the Zr-oxo clusters act as a Lewis acid active site for CO_2 activation and $TEOA^{\bullet+}$ generated by reduction of the porphyrin transfers a hydride to the proximal CO_2 was supported by both DFT calculations (showing modest energy barriers) and control experiments with different SEDs. Decreasing the hydricity of the SED led to lower formate production further indicating the prominent role the SED has in the CO_2 reduction reaction. Additionally, the mechanism would indicate a trend in reactivity that tracked with the ability of the porphyrin to generate $TEAO^{\bullet+}$ which was indeed observed.

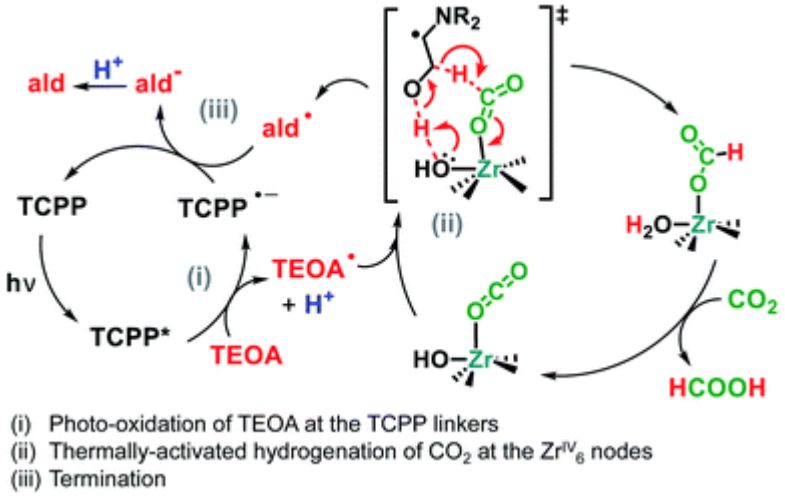

Figure 28: Proposed mechanism for CO_2 Reduction in MOF-545 frameworks. Reproduced from Journal of Materials Chemistry A 2022, 10 (35), 18103-18115, with permission from the Royal Society of Chemistry. [13]

The non-innocent role of SEDs was previously demonstrated for homogeneous catalysts.[28] The reliance on the SED to perform any type of chemistry is problematic for any catalytic system as SED are, as their name suggests, sacrificial and not catalytic. Similar mechanisms have now

been implicated in other MOF platforms.[29] Therefore, care should be taken when relying on such chemical species to demonstrate reactivity and turnover.

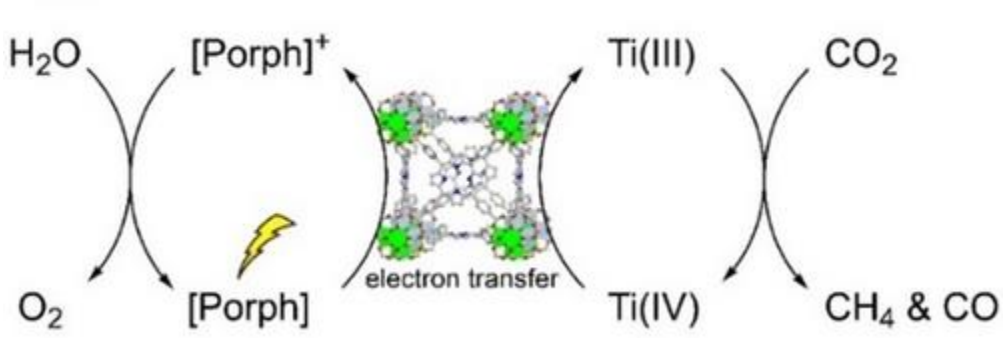

Figure 29: Mechanism for CO_2 reduction and Water Oxidation with Ti/Zr-MOF-525. Reprinted with permission from ChemSusChem 2020, 13 (23), 6273-6277., Copyright 2020, Wiley Materials. [23]

Another porphyrin MOF, MOF-525, which exhibits a ftw structure compared to the csq topology of MOF-545, was shown to reduce CO_2 in the absence of a sacrificial donor. The Zr-MOF was doped with Ti at the node via metal exchange at elevated temperature. The free base porphyrin is photoexcited and the titanium is reduced from Ti^{IV} to Ti^{III} like that observed in MIL-125(Ti). Interestingly, the oxidized porphyrin was proposed to oxidize the solvent, i.e., water producing oxygen and regenerating the initial state of the porphyrin. The Ti^{III} was proposed to reduce CO_2 and form the observed CO/CH_4 mixture of products. Control experiments using labelled $H_2{}^{18}O$ demonstrated that the amount of labelled $^{18}O_2$ formed matched the combined equivalents of CO and CH_4 products. Ti-exchanged 525 warrants further study for one clear reason the production of CH_4, an 8 e^- process, indicates a drastically different operative mechanism than MIL-125(Ti) even though the putative mechanism for charge separation and active site Ti^{III} are the same. Additionally, the ability to carry out complete artificial photosynthetic chemistry (water oxidation and carbon dioxide reduction) within a singular MOF platform is intriguing. For example, does the oxygen produced quench the excited state of the porphyrin by either energy transfer or electron transfer?

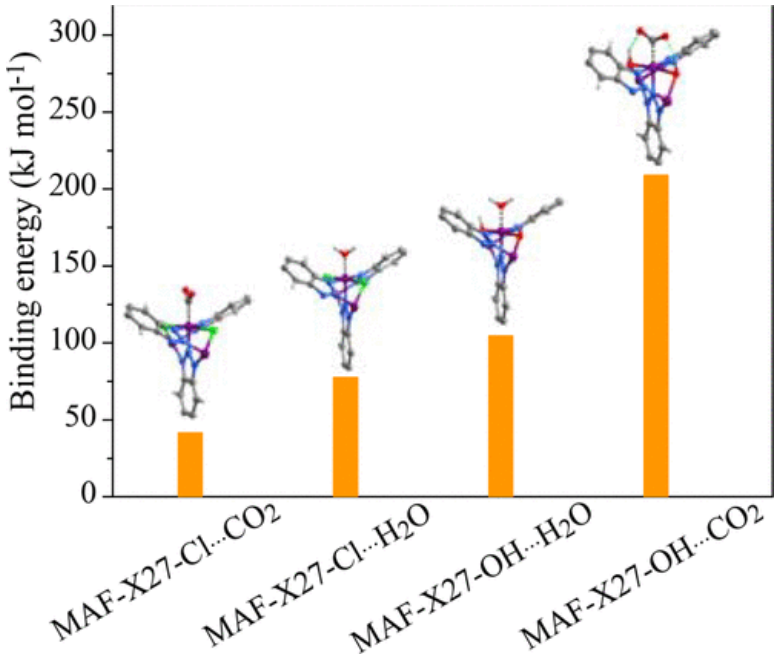

Figure 30: Binding Energy for H_2O and CO_2 in MAF-X27 MOFs. Reprinted with permission from **Journal of the American Chemical Society 2018, 140 (1), 38-41**. Copyright 2018 American Chemical Society. [19]

The stabilization of bound CO_2 intermediates has also been demonstrated to increase reactivity, like approaches exploited in homogeneous molecular catalysis. Two new cobalt MOFs were studied for photocatalytic CO_2 conversion to CO.[19] When combined with $Ru(bpy)_3$ and a SED, the new MOFs: $[Co_2(\mu\text{-}Cl)_2(bbta)]$ (MAF-X27-*l*Cl, H_2bbta =1 H,5H-benzo-(1,2-d:4,5-d′)bistriazole) and $[Co_2(\mu\text{-}OH)_2(bbta)]$ (MAF-X27-*l*OH) outperformed previously reported cobalt MOFs including Co-ZIF-9. The hydroxide ligand increased the turnover significantly and was able to produce CO at lower CO_2 pressures when compared to MAF-X27-Cl. DFT computational studies calculated the binding strength of the various MOFs with CO_2. The analysis showed a much higher binding energy for the hydroxylated MOF as well as formation of hydrogen bonds with the neighboring -OH groups. The increased stabilization of bound CO_2, shown in **Figure 7** can explain the promotion of CO_2 conversion by the –OH MOF compared to the -Cl MOF. The DFT calculations also showed a lower water binding energy, which would limit the competitive hydrogen evolution reaction.

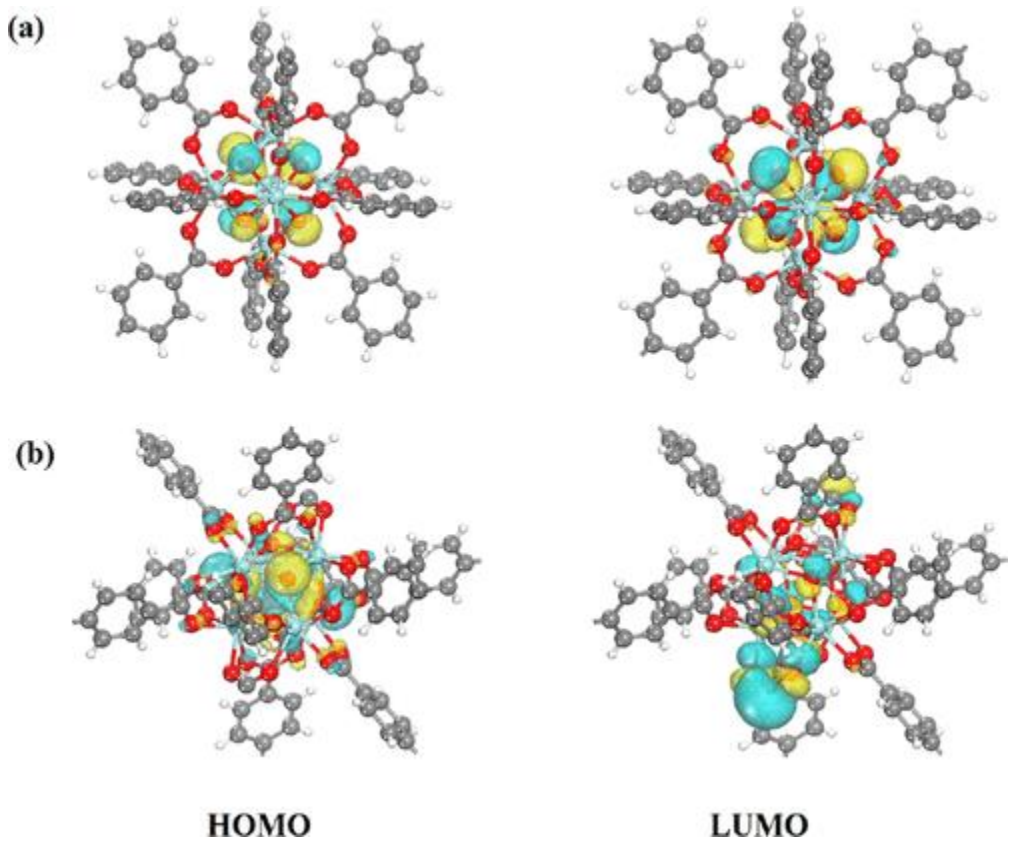

Figure 31: HOMO and LUMO of UiO-67 with (a) and without (b) defects. Reprinted with permission from Inorganic Chemistry 2022, 61 (3), 1765-1777. Copyright 2022 American Chemical Society. [21]

In addition to linker functionalization (*vide supra* on $–NH_2$ substituents) to tune absorption properties, ligand defects have also been used to tune the optical band gap of MOFs leading to enhanced reactivity.[21] It is well known that the use of modulators during Zr-based MOF synthesis can introduce missing linker defects, where the modulator remains bound to the node as opposed to the native linker. Typical modulators are formic acid, acetic acid, difluoroacetic acid, and benzoic acid. While pristine UiO-67 has 6 linkers per zirconium node, the defected samples in the referenced study had a range of 4.54 to 3.19 linkers per node confirmed by TGA analysis. The missing linker defects were introduced through the addition of different concentrations of formic acid in the synthesis. In a pristine UiO-67 structure, the HOMO-LUMO transition is predicted to primarily be Zr to Zr in character. Whereas, in the defected sample the LUMO contains a

significant contribution from the linker itself, indicative of an LMCT transition. The introduction of linker defects resulted in an increase in the average lifetime of the excited state from 5.9 ns to 7.1 ns. The increase in excited state lifetime was accompanied by an increase photocatalytic performance. When exposed to reaction conditions for CO_2 conversion, the defected material improved activity from 2.34 μmol g^{-1} h^{-1} to 12.29 μmol g^{-1} $h^{-1}$of CO. We do note that in addition to an increased lifetime of the excited state, more active sites are also available. Thus, it is likely that both components play a role in the observed increase in reactivity.

5.3 Linker-based Catalysts

Table 2: Summary of Earth-Abundant MOF-based Approaches for CO_2 Reduction with Linker based active sites

MOF	Light Absorber	Active Site	e^- donor	Light Source (nm)	Product	μmol/g	Time	Ref.
mPT-Cu/Re	Cu complex	Re complex	BIH[b]	350-700	$HCOO^-$	140	24 h	[30]
Zr-DMBD-Co[a]	$Ru(phen)_3$	Co^{II}	TEOA	450	CO	33300	10 h	[31]
Mn-UiO-67	$Ru(dmb)_3$	Mn-UiO-67	BNAH[c]	470	$HCOO^-$	1123	18 h	[32]

Cu@UiO-66-NH_2	UiO-66-NH_2	Cu single atom	TEOA	>400	CH_3OH CH_3CH_2OH	53.3 42.2	10 h	[33]
LTG-FeZr	Eosin Y	LTG-FeZr	TEOA	AM 1.5 sun	$HCOO^-$	265	6 h	[34]

[a] DMBD-2,5-dimercapto-1,4-benzenedicarboxyilic acid
[b] BIH-1,3-dimethyl-2-phenyl-2,3-dihydro-1*H*-benzo[*d*]imidazole
[c] BNAH-1-benzyl-1,4-dihydronicotinamide

The organic linkers in MOFs are generally aromatic molecules with multiple carboxylic acid groups that bind to the metal nodes to create the porous framework. The wide variety of linkers that have been incorporated into MOFs give the ability for these linkers to be functionalized for a many applications. Incorporating organometallic/inorganic catalysts in the backbone of the MOF allows for site isolation, which in many cases can attenuate or prevent known molecular degradation pathways (i.e., dimerization). While more amenable to modification than node functionalization, the limitations of requiring coordination to a multidentate linker does limit the complete versatility of catalyst design.

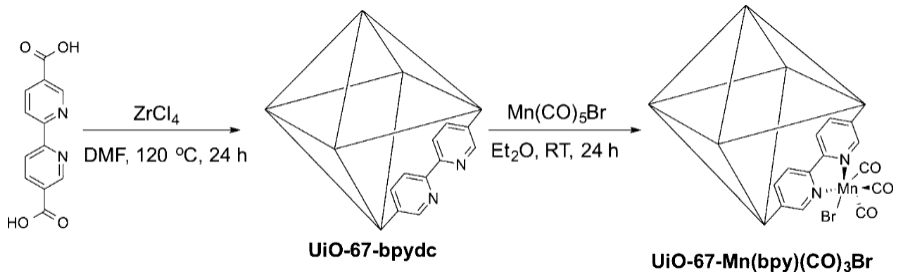

Figure 32: Post synthetic Incorporation of Mn catalyst into UiO-67. **Reprinted with permission from Inorganic Chemistry 2015 54 (14), 6821-6828. Copyright 2015 American Chemical Society** [32]

UiO-67 has been widely explored to support transition metal complexes due to the ease of incorporation of a bipyridine ligand into the framework through replacement of the native biphenyl linkers. Re(bpydc)$(CO)_3Cl$, (bpydc=bipyridine dicarboxylic acid) was one of the first complexes incorporated into UiO-67 for photocatalytic CO_2 conversion to CO.[35] While the MOF could be

recycled, the Re catalyst ultimately degraded through a photodissociation pathway and free Re was detected in the solution. The degradation led to a significant loss in reactivity after three catalytic cycles. In a similar fashion $Mn(CO)_3Br$ was post synthetically incorporated into the framework that had been doped with bpydc linkers, Figure 9.[32] The MOF produced $HCOO^-$ selectively with a turnover of 110 after 18 h. Importantly, the Mn-UiO-67 outperformed a homogeneous solution of the molecular analog, $Mn(bpydc)(CO)_3Br$, and was able to be recovered and recycled. That said, similar leaching of Mn was observed upon prolonged photolysis.

Incorporation of sensitizers into the backbone of the framework can inherently increase reactivity because of the structured distances between chromophores and actives species. While ruthenium and iridium polypyridyl complexes are generally used in current studies due to their long-lived charge separated states, the low abundance and overall toxicity of Ru and Ir means other photosensitizers need to be explored as alternatives. Copper complexes have recently emerged as viable replacements. That said, additional research is needed to extend the lifetimes of their excited states.[30, 36, 37] Immobilization of copper complexes in MOFs is one method to extend their lifetime, as rigidification of chromophores is known to attenuate non-radiative relaxation processes.

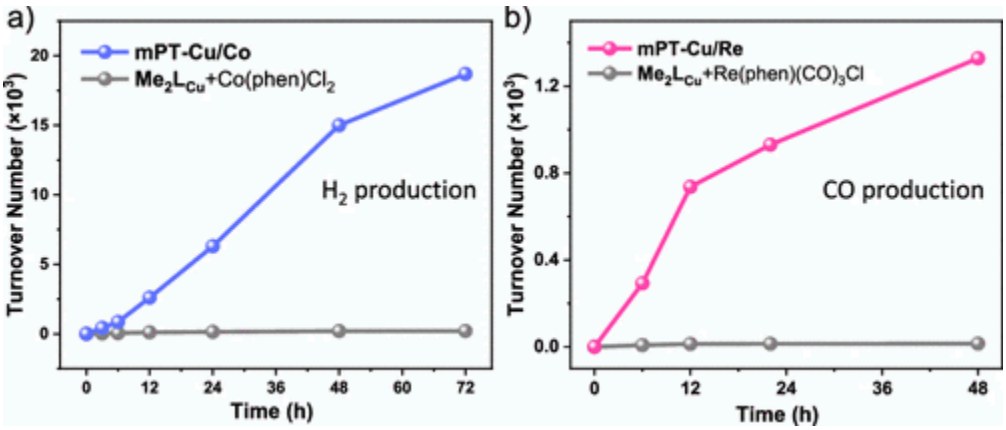

Figure 33: Reduction reaction products from copper photosensitized reactions. Reprinted with permission from **Journal of the American Chemical Society 2020, 142 (2), 690-695**. Copyright 2020 American Chemical Society [30]

A phenanthroline based MOF was co-loaded with a copper-based photosensitizer and rhenium catalyst. The post-synthetic metalation of phenanthroline-based linkers was completed in a stepwise fashion by first by reacting the MOF with $Re(CO)_5Cl$, second metalation with $Cu(CH_3CN)_4(PF_6)_2$, and coordination of of 1,2-bis(diphenylphosphino)ethane to the Cu. ICP analysis revealed a loading of 85% Cu and 14% Re. The dual functionalized MOF outperformed the homogeneous control by a factor of 95, resulting in a TON of 150 (6 h) and selectivity of 96% for CO. Photoluminescence measurements confirmed that the sensitizer was first quenched via the SED followed by electron transfer to the catalyst. Bulk photolysis experiments confirmed that the incorporation of the sensitizer stabilized the complex to degradation, an explanation for the superior performance.

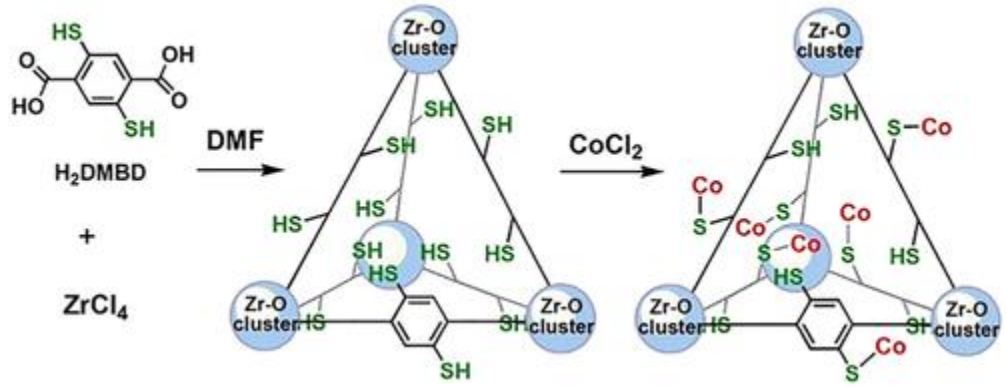

Figure 34:Immobilization of Co single atoms onto thiol decorated MOF. Reprinted from ChemSusChem 2019, 12 (10), 2166-2170., Copyright 2019, with permission from Wiley Materials [31]

In a similar fashion to bipyridine, thiol- and amine- decorated linkers have been employed as a ligation site for transition metals. Relevant to CO_2 reduction, cobalt ions were installed on a thiolate BDC linker, generating a competent photocatalyst with a turnover frequency for CO of 2.72 s^{-1}.[31] The overall activity was dependent on the degree of Co incorporation. While increased Co amounts generated more actives sites, too much caused the formation of nanoclusters, which lowered turnover rates due to the blockage of active sites in the middle of these clusters. [38-40] The post synthetic incorporation of copper onto UiO-66-NH_2 resulted in single Cu atoms attached to

the amine groups.[33] The work on the Cu@UiO-66-NH_2 platform highlights the need for detailed investigation of the nature of the active site and potential photodegradation. Initially, the MOF was not active for CO_2 reduction. However, with prolonged irradiation an active species was produced capable of the production of methanol and ethanol at rates of 5.33 and 4.22 μmol h^{-1} g^{-1} respectively.

An iron based terpyridine linker, $[Fe(HL_{)2}]\cdot(BF4_{)2}$(HL= 4-([2,2′:6′,2″-terpyridin]-4′-yl)benzoic acid), was incorporated into a zirconium MOF for CO_2 activation.[41] The MOF was highly active for CO_2 conversion producing HCOOH at 265 μmol h^{-1} g^{-1}. Uniquely, in the dark, this MOF, LTG-FeZr, is active for cycloadditions of CO_2 to epoxide rings with conversion rates of up to 99% depending on the functionalization of the epoxide ring. Materials with dual functionality are important for the use of all available CO_2.

5.4 Pore Guest Catalysts

Table 3: Summary of Earth-Abundant MOF-based Approaches for CO_2 Reduction with Guest based active sites

MOF	Light Absorber	Active Site	e^- donor	Light source (nm)	Product	μmol/ g	Time	Ref.
$MAPbI_3$@ PCN-221	$MAPbI_3$@ PCN-221	$MAPbI_3$@ PCN-221	H_2O	>400	CH_4 CO	1700 1200	80 h	[26]
Ni@Ru-UiO-67	$Ru(bpy)_2(bpydc)$	Ni(bpet)	BIH/ TEOA	450	CO	4260	10 h	[38]

CoO/MIL -101	$Ru(bpy)_3$	CoO/MIL-101	TEOA	>420	CO	28700	4 h	[40]

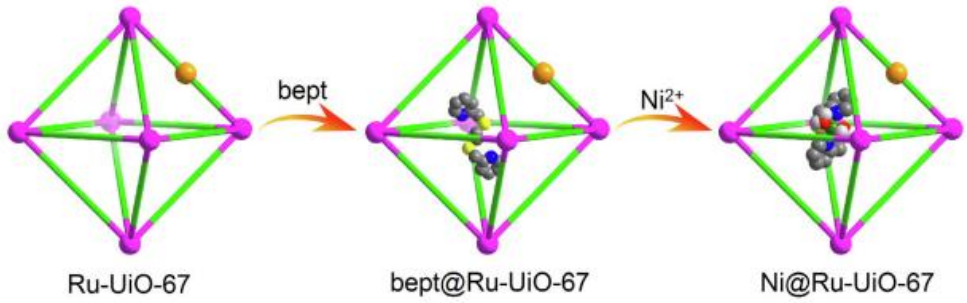

Figure 35: Guest Encapsulation of Ni complex into Ru-UiO-67. Reprinted from Science Bulletin 2019, 64 (14), 976-985., Copyright 2019, with permission from Elsevier[38]

Because of their porous nature, MOFs can be loaded with guest species that are not covalently bonded to the framework itself but confined to the pores.[42] While utilizing the inherent nodes or linkers of a MOF is limited to specific MOFs with active coordination sites, guests can be introduced in almost every MOF platform. Encapsulation provides many benefits including (1) controlled environment created due to the confined space of the pores, (2) site isolation, and (3) potential for multi-component guest encapsulation for cascade chemistry.

Like incorporation methods, encapsulation also provides site isolation and, therefore, can stabilize catalysts. For example, the encapsulation of a $Ni^{II}(bpet)(H_2O)_2$, ((bpet = 1,2-bis((pyridin-2-ylmethyl)thio)ethane) into UiO-67 loaded with $Ru(bpy)_2(bpydc)$ demonstrated a TON for CO production more than double the homogeneous complex in solution (581 and 280, respectively).[38] Both materials exhibited the same initial rates, indicating that the mechanism of reactivity was likely unchanged due to encapsulation. However, the homogeneous catalyst deactivated after about 5 h, while the MOF composite exhibited CO production well over 10 h. The MOF was also able to be collected, exposed to fresh catalysis solution, and another catalysis batch run with no loss in catalytic rate.

Encapsulated materials also serve as a pathway to cooperative reactivity. For example, a MOF known to be competent in CO_2 adsorption can serve and the host for a known CO_2 reduction catalyst. MIL-101(Cr) has been shown to have high CO_2 uptake due to the Lewis acidity of the Cr^{III} nodes. When combined with an active reduction catalyst like CoO_x, the CO production increased in comparison to CoO_x alone. CoO_x nanoparticles were encapsulated into MIL-101(Cr) by introduction of Co^{2+} ions and subsequent combustion to produce the oxide. Incorporation at 2.6 wt% showed the highest CO production at 28.7 μmol h^{-1}. In another example of cooperative chemistry, ZIF-8, another framework with high CO_2 sorption capacity, was used to encapsulate a perovskite known to reduce CO_2 to CO. Under ambient conditions, perovskites are known to be unstable. Therefore, encapsulation provided a route to enhanced stability, proximal CO_2 placement (due to MOF adsorption), and recyclability. Specifically, a $CsPbBr_3$ perovskite was immobilized in both a zinc- and cobalt-based ZIFs, ZIF-8 and ZIF-67, **Figure 13**.[43] The $CsPbBr_3$@ZIF composite was then subject to light irradiation under a CO_2 atmosphere where methane was detected as the major product with over 90% selectivity. The catalyst was stable over multiple cycles and had higher efficiency compared to a physical mixture of the two solids indicating a cooperative effect.

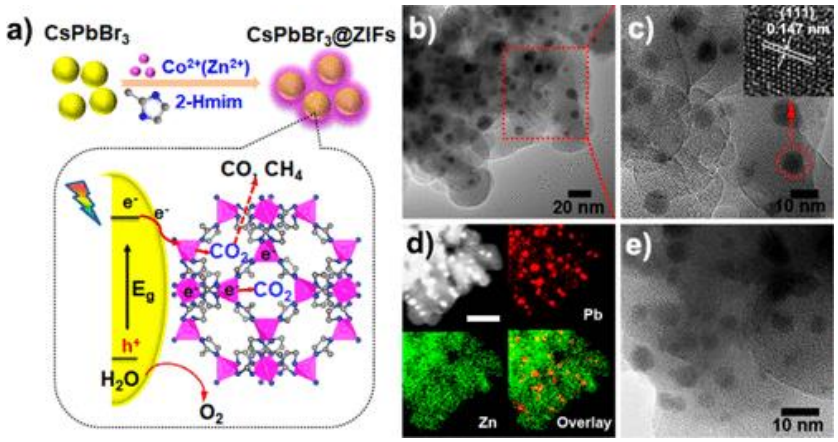

Figure 13: Perovskites grown within ZIF-8; a) synthetic scheme and proposed mechanism of CO_2 reduction b-e) TEM imaging of composite $CsPbBr_3$@ZIF and atom mapping. Reprinted with permission from ACS Energy Letters 2018, 3 (11), 2656-2662. Copyright 2018 American Chemical Society.[43]

5.5 MOF COMPOSITES

Table 4: Summary of Earth-Abundant MOF-based Approaches for CO_2 Reduction for Composite Materials

MOF	Light Absorber	Active Site	e^- donor	Light Source (nm)	Product	µmol/g	Time	Ref
g-C_3N_4/CuO@ MIL-125	g-C_3N_4	Ti cluster	H_2O	420	CO CH_3OH CH_3CHO CH_3CH_2OH	180.1 997.2 531.5 1505.7	3 h	[39]
NH_2-rGO/Al-PMOF	NH_2-rGO	Al-PMOF	TEOA	White light (Hg Lamp)	HCOOH	685.6	1 h	[27]
Co-ZIF-9/TiO_2	TiO_2	Co-ZIF-9	H_2O	White Light (Xe Lamp)	CO CH_4	175.8 19.8	10 h	[44]

MOFs can be grown from the surface of many known light absorbers to form composites. One important aspect of composites is the need for a controlled ratio between the MOF and composite material.[27, 43, 44] In typical approaches, where the added material absorbs light and the MOF acts

as the catalyst, too little light absorber can result in reduced activity simply because the generation of excited states is insufficient. On the other hand, too much of the light absorber can block active sites and/or promote non-productive excited state relaxation, which would also decrease reactivity.

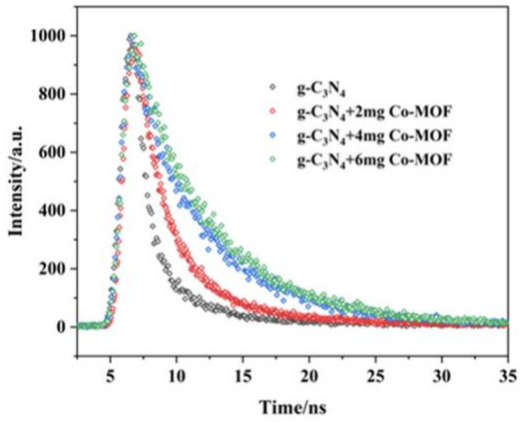

*Figure 14: Lifetime of graphitic carbon nitride increasing with the addition of Co-MOF. Reprinted with permission from Inorganic Chemistry **2023**, 62 (3), 1240-1249. Copyright 2023 American Chemical Society.*[45]

A key component of composites is the generation of charge separated states with extended distances between the charges. Graphitic carbon nitride (g-C_3N_4) is an analog of graphene with nitrogen groups doped into the crystal structure.[45] A cobalt MOF was grown on g-C_3N_4 for photocatalytic conversion of CO_2. The excited state of g-C_3N_4 reduced the MOF incorporated cobalt to form a charge separated state across the g-C_3N_4/MOF interface, as observed through transient absorption studies. The lifetime of the charge separated state was greater than that of g-C_3N_4 alone, increasing from 4.15 ns to 19.57 ns at the highest loading of MOF, Figure 14. The increase in lifetime promoted and increase in CO generation to 1824 µmol h^{-1} g^{-1}, which was a seven-fold increase compared to the native MOF without the g-C_3N_4.

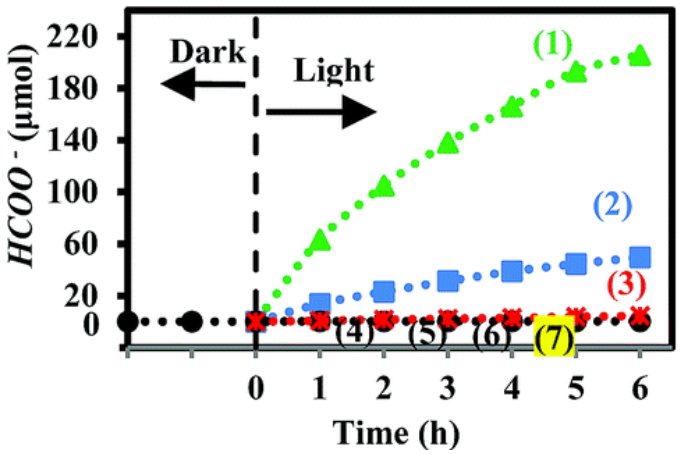

Figure 15: Production of $HCOO^-$ for NH_2-rGO/Al-PMOF (green triangle), Al-PMOF (blue square),TCPP (red x), and other controls (black) Reproduced from Journal of Materials Chemistry A 2018, 6 (37), 18031-18035 with permission from the Royal Society of Chemistry.[27]

Composites also provide a route for cooperative chemistry through environmental effects. An aluminum-based porphyrin MOF was grown on amine-functionalized reduced graphene oxide, NH_2-rGO and used in photocatalysis.[27] The $HCOO^-$ production increased from 165.3 μmol h^{-1} g^{-1} to 685.6 μmol h^{-1} g^{-1} when the NH_2-rGO was combined with the MOF with almost 100% selectivity shown in Figure 15. The authors hypothesized that the pendant amine groups of the NH_2-rGO provide hydrogens proximal to the active sites of the MOF, an approach previously exploited in molecular catalysis (*vide supra*).

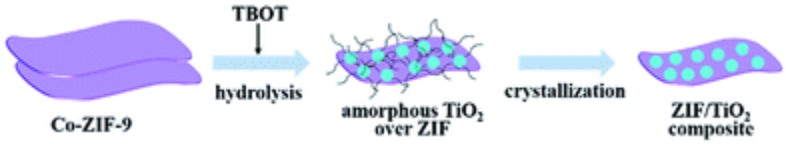

Figure 16: TiO_2/ZIF composite synthesis. Reproduced from Journal of Materials Chemistry A 2016, 4 (39) with permission from the Royal Society of Chemistry.[44]

Similar approaches have been carried out with TiO_2 as the light absorbing material. Yan et al. grew Co-ZIF-9 on TiO_2 to achieve higher efficiency of photochemical CO_2 reduction.[44] Co-ZIF-9 was previously used as a cocatalyst with $Ru(bpy)_3$ to reduce CO_2.[20] Co-ZIF-9 is a cobalt ZIF with benzimidazolate linkers. Using a wavelength dependence study, the reaction was shown to be dependent on excitation of the $Ru(bpy)_3$ sensitizer, however when loaded with higher

concentrations of the dye, the reaction favored hydrogen evolution most likely due to the formation of a catalytic ruthenium species for proton reduction. The use of the molecular photosensitizer limits the commercial application of the material due to instability and deactivation. Yan et. Al. grew Co-ZIF-9 onto TiO_2 to use as a light absorber for CO_2 conversion. The composite showed successful photochemical production of CO and CH_4 at rates of 175.8 and 19.8 μmol h^{-1} g^{-1}, respectively.[44] The composite material showed higher turnover numbers for CO and CH_4 products than a physical mixture of the materials showing a productive interaction between the materials upon growth.

5.6 CONCLUSION

Overall, MOFs show great promise as CO_2 conversion photocatalysts when utilizing earth abundant complexes. Because photoreductive processes have multiple steps; light adsorption, charge transfer, and substrate reduction, MOFs provide an ideal backbone for one material to complete all steps of the catalysis. While much progress has been made, MOFs are complex materials, and their translation to commercial application is limited by our lack of understanding in design principles required to create active scaffolds. Future research should also explore synthetic methods to combine the photosensitizer and catalyst in an efficient manner, as well as study impacts of particle size, catalyst doping levels, and solvent conditions. Mechanistic studies to understand the fundamental limitations in efficiency and to uncover clear methods next generation design are needed. The examples herein highlight the need for detailed investigations of photoinduced processes via advances spectroscopic techniques, optimization of the parameters that dominate charge transfer processes throughout the framework, and discovery of new platforms for highly active photoreduction catalysts.

ACKNOWLEDGEMENTS

This work was supported by the Department of Energy under Grant DE-SC0012445.

5.7 REFERENCES

(1) Administration, U. S. E. I. *Electricity Explained*. 2023. https://www.eia.gov/energyexplained/electricity/electricity-in-the-us.php (accessed 2023 07/03).

(2) USGS. *What is carbon sequestration?* 2023. https://www.usgs.gov/faqs/what-carbon-sequestration (accessed 2023 July 6).

(3) *Renewables 2022*; Paris, 2022. https://www.iea.org/reports/renewables-2022.

(4) Energy, D. o. *Sunshot 2030*. https://www.energy.gov/eere/solar/sunshot-2030 (accessed.

(5) Kuhl, K. P.; Cave, E. R.; Abram, D. N.; Jaramillo, T. F. New insights into the electrochemical reduction of carbon dioxide on metallic copper surfaces. *Energy & Environmental Science* **2012**, *5* (5), 7050-7059, 10.1039/C2EE21234J. DOI: 10.1039/C2EE21234J.

(6) Huang, Z.; Grim, R. G.; Schaidle, J. A.; Tao, L. The economic outlook for converting CO2 and electrons to molecules. *Energy & Environmental Science* **2021**, *14* (7), 3664-3678, 10.1039/D0EE03525D. DOI: 10.1039/D0EE03525D.

(7) Laumb, J. D.; Kay, J. P.; Holmes, M. J.; Cowan, R. M.; Azenkeng, A.; Heebink, L. V.; Hanson, S. K.; Jensen, M. D.; Letvin, P. A.; Raymond, L. J. Economic and Market Analysis of CO2 Utilization Technologies – Focus on CO2 derived from North Dakota lignite. *Energy Procedia* **2013**, *37*, 6987-6998. DOI: https://doi.org/10.1016/j.egypro.2013.06.632.

(8) Hong-Cai Zhou, J. R. L., and Omar M. Yaghi. Introduction to Metal–Organic Frameworks. *Chemical Reviews* **2012**, *112* (2), 673-674. DOI: 10.1021/cr300014x.

(9) Maza, W. A.; Morris, A. J. Photophysical Characterization of a Ruthenium(II) Tris(2,2′-bipyridine)-Doped Zirconium UiO-67 Metal–Organic Framework. *The Journal of Physical Chemistry C* **2014**, *118* (17), 8803-8817. DOI: 10.1021/jp501140r.

(10) Gibbons, B.; Cairnie, D. R.; Thomas, B.; Yang, X.; Ilic, S.; Morris, A. J. Photoelectrochemical water oxidation by a MOF/semiconductor composite. *Chemical Science* **2023**, *14* (18), 4672-4680, 10.1039/D2SC06361A. DOI: 10.1039/D2SC06361A.

(11) Cai, M.; Loague, Q.; Morris, A. J. Design Rules for Efficient Charge Transfer in Metal–Organic Framework Films: The Pore Size Effect. *The Journal of Physical Chemistry Letters* **2020**, *11* (3), 702-709. DOI: 10.1021/acs.jpclett.9b03285.

(12) Getting Down to Earth: The Renaissance of Catalysis with Abundant Metals. *Accounts of Chemical Research* **2015**, *48* (9), 2495-2495. DOI: 10.1021/acs.accounts.5b00385.

(13) Benseghir, Y.; Solé-Daura, A.; Cairnie, D. R.; Robinson, A. L.; Duguet, M.; Mialane, P.; Gairola, P.; Gomez-Mingot, M.; Fontecave, M.; Iovan, D.; et al. Unveiling the mechanism of the photocatalytic reduction of CO2 to formate promoted by porphyrinic Zr-based metal–organic frameworks. *Journal of Materials Chemistry A* **2022**, *10* (35), 18103-18115, 10.1039/D2TA04164B. DOI: 10.1039/D2TA04164B.

(14) Usov, P. M.; Huffman, B.; Epley, C. C.; Kessinger, M. C.; Zhu, J.; Maza, W. A.; Morris, A. J. Study of Electrocatalytic Properties of Metal–Organic Framework PCN-223 for the Oxygen Reduction Reaction. *ACS Applied Materials & Interfaces* **2017**, *9* (39), 33539-33543. DOI: 10.1021/acsami.7b01547.

(15) Lin, S.; Pineda-Galvan, Y.; Maza, W. A.; Epley, C. C.; Zhu, J.; Kessinger, M. C.; Pushkar, Y.; Morris, A. J. Electrochemical Water Oxidation by a Catalyst-Modified Metal–Organic Framework Thin Film. *ChemSusChem* **2017**, *10* (3), 514-522. DOI: https://doi.org/10.1002/cssc.201601181.

(16) Zhu, J.; Usov, P. M.; Xu, W.; Celis-Salazar, P. J.; Lin, S.; Kessinger, M. C.; Landaverde-Alvarado, C.; Cai, M.; May, A. M.; Slebodnick, C.; et al. A New Class of Metal-Cyclam-Based

Zirconium Metal–Organic Frameworks for CO2 Adsorption and Chemical Fixation. *Journal of the American Chemical Society* **2018**, *140* (3), 993-1003. DOI: 10.1021/jacs.7b10643.

(17) Fu, Y.; Sun, D.; Chen, Y.; Huang, R.; Ding, Z.; Fu, X.; Li, Z. An Amine-Functionalized Titanium Metal–Organic Framework Photocatalyst with Visible-Light-Induced Activity for CO2 Reduction. *Angewandte Chemie International Edition* **2012**, *51* (14), 3364-3367. DOI: https://doi.org/10.1002/anie.201108357.

(18) Wang, D.; Huang, R.; Liu, W.; Sun, D.; Li, Z. Fe-Based MOFs for Photocatalytic CO2 Reduction: Role of Coordination Unsaturated Sites and Dual Excitation Pathways. *ACS Catalysis* **2014**, *4* (12), 4254-4260. DOI: 10.1021/cs501169t.

(19) Wang, Y.; Huang, N.-Y.; Shen, J.-Q.; Liao, P.-Q.; Chen, X.-M.; Zhang, J.-P. Hydroxide Ligands Cooperate with Catalytic Centers in Metal–Organic Frameworks for Efficient Photocatalytic CO2 Reduction. *Journal of the American Chemical Society* **2018**, *140* (1), 38-41. DOI: 10.1021/jacs.7b10107.

(20) Wang, S.; Yao, W.; Lin, J.; Ding, Z.; Wang, X. Cobalt Imidazolate Metal–Organic Frameworks Photosplit CO2 under Mild Reaction Conditions. *Angewandte Chemie International Edition* **2014**, *53* (4), 1034-1038. DOI: https://doi.org/10.1002/anie.201309426.

(21) Zhao, X.; Xu, M.; Song, X.; Liu, X.; Zhou, W.; Wang, H.; Huo, P. Tailored Linker Defects in UiO-67 with High Ligand-to-Metal Charge Transfer toward Efficient Photoreduction of CO2. *Inorganic Chemistry* **2022**, *61* (3), 1765-1777. DOI: 10.1021/acs.inorgchem.1c03690.

(22) Wang, S.-S.; Huang, H.-H.; Liu, M.; Yao, S.; Guo, S.; Wang, J.-W.; Zhang, Z.-M.; Lu, T.-B. Encapsulation of Single Iron Sites in a Metal–Porphyrin Framework for High-Performance Photocatalytic CO2 Reduction. *Inorganic Chemistry* **2020**, *59* (9), 6301-6307. DOI: 10.1021/acs.inorgchem.0c00407.

(23) Gao, W.-Y.; Ngo, H. T.; Niu, Z.; Zhang, W.; Pan, Y.; Yang, Z.; Bhethanabotla, V. R.; Joseph, B.; Aguila, B.; Ma, S. A Mixed-Metal Porphyrinic Framework Promoting Gas-Phase CO2 Photoreduction without Organic Sacrificial Agents. *ChemSusChem* **2020**, *13* (23), 6273-6277. DOI: https://doi.org/10.1002/cssc.202001610.

(24) Cheng, X.-M.; Dao, X.-Y.; Wang, S.-Q.; Zhao, J.; Sun, W.-Y. Enhanced Photocatalytic CO2 Reduction Activity over NH2-MIL-125(Ti) by Facet Regulation. *ACS Catalysis* **2021**, *11* (2), 650-658. DOI: 10.1021/acscatal.0c04426.

(25) Ma, M.; Bétard, A.; Weber, I.; Al-Hokbany, N. S.; Fischer, R. A.; Metzler-Nolte, N. Iron-Based Metal–Organic Frameworks MIL-88B and NH2-MIL-88B: High Quality Microwave Synthesis and Solvent-Induced Lattice "Breathing". *Crystal Growth & Design* **2013**, *13* (6), 2286-2291. DOI: 10.1021/cg301738p.

(26) Wu, L.-Y.; Mu, Y.-F.; Guo, X.-X.; Zhang, W.; Zhang, Z.-M.; Zhang, M.; Lu, T.-B. Encapsulating Perovskite Quantum Dots in Iron-Based Metal–Organic Frameworks (MOFs) for Efficient Photocatalytic CO2 Reduction. *Angewandte Chemie International Edition* **2019**, *58* (28), 9491-9495. DOI: https://doi.org/10.1002/anie.201904537.

(27) Sadeghi, N.; Sharifnia, S.; Do, T.-O. Enhanced CO2 photoreduction by a graphene–porphyrin metal–organic framework under visible light irradiation. *Journal of Materials Chemistry A* **2018**, *6* (37), 18031-18035, 10.1039/C8TA07158F. DOI: 10.1039/C8TA07158F.

(28) Sampaio, R. N.; Grills, D. C.; Polyansky, D. E.; Szalda, D. J.; Fujita, E. Unexpected Roles of Triethanolamine in the Photochemical Reduction of CO2 to Formate by Ruthenium Complexes. *Journal of the American Chemical Society* **2020**, *142* (5), 2413-2428. DOI: 10.1021/jacs.9b11897.

(29) Zheng, X.; Drummer, M. C.; He, H.; Rayder, T. M.; Niklas, J.; Weingartz, N. P.; Bolotin, I. L.; Singh, V.; Kramar, B. V.; Chen, L. X.; et al. Photoreactive Carbon Dioxide Capture by a Zirconium–Nanographene Metal–Organic Framework. *The Journal of Physical Chemistry Letters* **2023**, *14* (18), 4334-4341. DOI: 10.1021/acs.jpclett.3c00049.

(30) Feng, X.; Pi, Y.; Song, Y.; Brzezinski, C.; Xu, Z.; Li, Z.; Lin, W. Metal–Organic Frameworks Significantly Enhance Photocatalytic Hydrogen Evolution and CO2 Reduction with Earth-Abundant Copper Photosensitizers. *Journal of the American Chemical Society* **2020**, *142* (2), 690-695. DOI: 10.1021/jacs.9b12229.

(31) Liu, D.-C.; Ouyang, T.; Xiao, R.; Liu, W.-J.; Zhong, D.-C.; Xu, Z.; Lu, T.-B. Anchoring CoII Ions into a Thiol-Laced Metal–Organic Framework for Efficient Visible-Light-Driven Conversion of CO2 into CO. *ChemSusChem* **2019**, *12* (10), 2166-2170. DOI: https://doi.org/10.1002/cssc.201900338.

(32) Fei, H.; Sampson, M. D.; Lee, Y.; Kubiak, C. P.; Cohen, S. M. Photocatalytic CO2 Reduction to Formate Using a Mn(I) Molecular Catalyst in a Robust Metal–Organic Framework. *Inorganic Chemistry* **2015**, *54* (14), 6821-6828. DOI: 10.1021/acs.inorgchem.5b00752.

(33) Wang, G.; He, C.-T.; Huang, R.; Mao, J.; Wang, D.; Li, Y. Photoinduction of Cu Single Atoms Decorated on UiO-66-NH2 for Enhanced Photocatalytic Reduction of CO2 to Liquid Fuels. *Journal of the American Chemical Society* **2020**, *142* (45), 19339-19345. DOI: 10.1021/jacs.0c09599.

(34) Wang, X.; Li, J.; Kou, M.; Dou, W.; Bai, D.; Tang, X.; Tang, Y.; Liu, W. Dual-Function Precious-Metal-Free Metal–Organic Framework for Photocatalytic Conversion and Chemical Fixation of Carbon Dioxide. *Inorganic Chemistry* **2023**, *62* (46), 19015-19024. DOI: 10.1021/acs.inorgchem.3c02765.

(35) Wang, C.; Xie, Z.; deKrafft, K. E.; Lin, W. Doping Metal–Organic Frameworks for Water Oxidation, Carbon Dioxide Reduction, and Organic Photocatalysis. *Journal of the American Chemical Society* **2011**, *133* (34), 13445-13454. DOI: 10.1021/ja203564w.

(36) Guo, G.-C.; Ma, L.; Li, X.-D.; Guo, S.; Lu, T.-B.; Zhang, Z.-M. Engineering earth-abundant copper(i) sensitizing centers in metal–organic frameworks for efficient photosynthesis. *Journal of Materials Chemistry A* **2023**, *11* (26), 14052-14057, 10.1039/D3TA02142D. DOI: 10.1039/D3TA02142D.

(37) Feng, X.; Pi, Y.; Song, Y.; Xu, Z.; Li, Z.; Lin, W. Integration of Earth-Abundant Photosensitizers and Catalysts in Metal–Organic Frameworks Enhances Photocatalytic Aerobic Oxidation. *ACS Catalysis* **2021**, *11* (3), 1024-1032. DOI: 10.1021/acscatal.0c05053.

(38) Yan, Z.-H.; Ma, B.; Li, S.-R.; Liu, J.; Chen, R.; Du, M.-H.; Jin, S.; Zhuang, G.-L.; Long, L.-S.; Kong, X.-J.; et al. Encapsulating a Ni(II) molecular catalyst in photoactive metal–organic framework for highly efficient photoreduction of CO2. *Science Bulletin* **2019**, *64* (14), 976-985. DOI: https://doi.org/10.1016/j.scib.2019.05.014.

(39) Li, N.; Liu, X.; Zhou, J.; Chen, W.; Liu, M. Encapsulating CuO quantum dots in MIL-125(Ti) coupled with g-C3N4 for efficient photocatalytic CO2 reduction. *Chemical Engineering Journal* **2020**, *399*, 125782. DOI: https://doi.org/10.1016/j.cej.2020.125782.

(40) Ma, Y.; Du, J.; Fang, Y.; Wang, X. Encapsulation of Cobalt Oxide into Metal-Organic Frameworks for an Improved Photocatalytic CO2 Reduction. *ChemSusChem* **2021**, *14* (3), 946-951. DOI: https://doi.org/10.1002/cssc.202002656.

(41) Wang, X.; Li, J.; Kou, M.; Dou, W.; Bai, D.; Tang, X.; Tang, Y.; Liu, W. Dual-Function Precious-Metal-Free Metal–Organic Framework for Photocatalytic Conversion and Chemical Fixation of Carbon Dioxide. *Inorganic Chemistry* **2023**. DOI: 10.1021/acs.inorgchem.3c02765.

(42) Li, Z.; Rayder, T. M.; Luo, L.; Byers, J. A.; Tsung, C.-K. Aperture-Opening Encapsulation of a Transition Metal Catalyst in a Metal–Organic Framework for CO2 Hydrogenation. *Journal of the American Chemical Society* **2018**, *140* (26), 8082-8085. DOI: 10.1021/jacs.8b04047.

(43) Kong, Z.-C.; Liao, J.-F.; Dong, Y.-J.; Xu, Y.-F.; Chen, H.-Y.; Kuang, D.-B.; Su, C.-Y. Core@Shell CsPbBr3@Zeolitic Imidazolate Framework Nanocomposite for Efficient Photocatalytic CO2 Reduction. *ACS Energy Letters* **2018**, *3* (11), 2656-2662. DOI: 10.1021/acsenergylett.8b01658.

(44) Yan, S.; Ouyang, S.; Xu, H.; Zhao, M.; Zhang, X.; Ye, J. Co-ZIF-9/TiO2 nanostructure for superior CO2 photoreduction activity. *Journal of Materials Chemistry A* **2016**, *4* (39), 15126-15133, 10.1039/C6TA04620G. DOI: 10.1039/C6TA04620G.

(45) Zhao, Y.; Cui, Y.; Xie, L.; Geng, K.; Wu, J.; Meng, X.; Hou, H. Rational Construction of Metal Organic Framework Hybrid Assemblies for Visible Light-Driven CO2 Conversion. *Inorganic Chemistry* **2023**, *62* (3), 1240-1249. DOI: 10.1021/acs.inorgchem.2c03970.